

---

## **Search for Heavy Stable Charged Particles with the CMS detector at the LHC**

From Detector Commissioning to Data Analysis

---

Doctoral dissertation presented by  
**Loïc Quertenmont**  
in fulfilment of the requirements for the degree of Doctor in Sciences

---

Prof. G. Bruno (Advisor)	UCL, Belgium
Prof. J-M. Gérard (Chairman)	UCL, Belgium
Prof. V. Lemaître	UCL, Belgium
Prof. N. van Remortel	UA, Belgium
Prof. D. Contardo	IPNL, France
Prof. D. Stuart	UCSB, USA

---

October 2010



# Remerciements

*Avant de remercier toutes les personnes qui ont contribuées au bon déroulement de ce travail, je souhaiterais mettre en évidence la bonne étoile qui m'a accompagné ces derniers temps. Je pense que le bon déroulement d'un travail aussi conséquent n'a été possible que grâce à la rencontre de plusieurs éléments indispensables. Tout d'abord, j'ai eu la chance de travailler dans le cadre de recherche idéal qu'est le "center for Cosmology, Particle Physics and Phenomenology (CP3)". Ensuite j'ai eu la chance de côtoyer les personnes qui, au cours de mes études, mémoire et maintenant thèse, ont par leur expérience et leur passion pu me donner goût à la recherche scientifique. Finalement, le moment auquel j'ai eu la chance de commencer cette recherche m'aura permis de travailler avec des données simulées comme beaucoup l'ont fait avant moi, mais également avec des données provenant de particules cosmiques comme beaucoup d'autres ont pu le faire en même temps que moi, et finalement avec des données provenant de collisions de protons au LHC comme sans doute beaucoup d'autres le feront encore après moi. Je me rends compte de la grande chance que j'ai eu d'avoir pu participer à l'analyse de ces trois différents types de données. Ceci n'aurait évidemment pas été possible sans la liste, non exhaustive, des personnes citées ci-dessous.*

*Je tiens tout d'abord à remercier le professeur Giacomo Bruno de m'avoir offert la possibilité d'effectuer ce travail. Ses idées pertinentes, son souci du détail et sa persévérance sont à la base de ce travail. Merci pour la grande liberté qu'il m'a accordée et les responsabilités qu'il m'a laissé prendre en toute confiance. Grâce à lui, cette thèse a été une expérience intense et passionnante durant laquelle j'ai énormément appris.*

*Cette thèse n'a été possible que grâce au support du Fonds de la Recherche Scientifique, qui a financé cette recherche via sa bourse F.R.I.A. Je tiens donc à remercier les responsables de cet organisme pour la confiance qu'ils m'ont accordée.*

*Je souhaiterais également remercier les membres de mon Jury de soutenance, les professeurs Jean-Marc Gérard, Vincent Lemaître, Nick van Remortel, Didier Contardo et David Stuart, qui ont sacrifié une partie de leur temps pour évaluer ce travail et contribuer à améliorer ce manuscrit grâce à la pertinence de leurs nombreux commentaires. J'ai eu énormément de plaisir à discuter avec vous... merci.*

*Evidemment, je n'oublie pas les autres membres du CP3, qui ont contribué à rendre ces années extrêmement enrichissantes. Je pense entre autres à nos professeurs souvent trop occupés, mais qui, lors de rencontres infortuites dans les couloirs, ont toujours eu quelques mots d'encouragement. Je pense en particulier aux professeurs Eduardo Cortina, Vincent Lemaître et Jean-Marc Gérard.*

*Je pense également aux post-doctorants, doctorants, mémorants et aux autres membres du CP3 qui sont toujours là pour mettre de l'ambiance ou tout simplement de la vie dans notre institut. Je tiens à remercier mes collègues et amis, Nicolas Schul, Julien Caudron, Andrea Giannanco, Suzan Basegmez, Philippe Merten, Céline Degrande, Arnaud Pin et d'autres, qui, au cours de simples mais fréquentes discussions, m'ont souvent permis de résoudre les nombreux problèmes que j'ai rencontrés tout au long de ma recherche. Je n'oublie évidemment pas nos anciens : Séverine Ovyn, Xavier Rouby, Simon de Visscher, etc. Ils ont sans aucun doute tous contribué à rendre nos locaux plus attachants.*

*Je souhaiterais également profiter de cette occasion pour remercier le staff administratif et informatique de CP3, ils sont souvent en première ligne lorsque quelque chose ne va pas, mais ne sont que trop rarement remercié lorsque tout fonctionne correctement. De plus, ils doivent souvent composer avec la mauvaise humeur des utilisateurs et en particulier avec la mienne. Je tiens donc particulièrement à les remercier de m'avoir (presque toujours) permis de garder mon travail en mouvement.*

*J'ai également une pensée pour toutes les personnes, du CERN et d'ailleurs, avec qui j'ai eu l'occasion de collaborer tout au long de cette recherche. Je pense également aux collaborateurs du groupe HSCP de CMS qui ont été d'une précieuse aide dans mon travail: Andrea Rizzi, Jie Chen, Camilo Carrillo. Leur soutien et expérience ont été d'une grande aide pour ce travail.*

*Un travail qui me tient tout particulièrement à cœur est évidemment la création de FROG. Ce projet à souvent, à tort, été perçu comme allant à contre-courant. Je souhaiterais donc remercier tout ceux qui ont participé à ce projet, ou tout simplement ceux qui ont eu le courage de le soutenir. Je remercie chaleureusement Vincent Roberfroid sans qui cette aventure n'aurait jamais commencé. FROG est le fruit de notre collaboration fructueuse. Je tiens également à saluer Christophe Delaere, qui en plus de son aide précieuse sur d'autres sujets, a été le premier à réellement utiliser FROG pour le commissioning de CMS. C'est entre autres grâce à lui que ce logiciel*

*est connu par la collaboration CMS tout entière. D'autres personnes ont évidemment contribué à ce succès, je pense entre autres à Nicolas Schul, Julien Caudron, Dorian Kcira et Muriel Vander Donckt.*

*Sans le soutien de ma famille, il m'aurait été impossible d'achever ce travail. Ils le savent déjà, mais je leur suis extrêmement reconnaissant pour toute l'aide morale qu'ils m'ont donnée. Ce sont eux qui ont depuis toujours observé une démarche scientifique en moi et m'ont poussé dans cette direction. Ma soeur doit également être particulièrement remerciée pour la patience qu'elle a eu lors des nombreuses lectures et relectures de ce manuscrit. Elle a également participé à en améliorer le contenu.*

*Merci à toi, Emilie, qui es là depuis le premier jour de cette thèse. Au cours de ces trois dernières années, tu n'as jamais cessé de m'écouter, de me soutenir et de m'encourager. Tu m'as laissé prendre du temps, des journées, des week-ends, des vacances... afin de me permettre avancer dans cette recherche. De nombreuses heures sur notre temps, ton temps.*

*Merci à vous tous, qui avez, par vos conseils, votre soutien, votre connaissance ou simplement par votre présence, permis la réalisation de cette thèse.*



This page is dedicated to the one I love,  
Emilie, this is for you...

### **The Square Root of Three**

*I'm sure that I will always be  
A lonely number like root three*

*The three is all that's good and right,  
Why must my three keep out of sight  
Beneath the vicious square root sign,  
I wish instead I were a nine*

*For nine could thwart this evil trick,  
with just some quick arithmetic*

*I know I'll never see the sun, as 1.7321  
Such is my reality, a sad irrationality*

*When hark! What is this I see,  
Another square root of a three*

*As quietly co-waltzing by,  
Together now we multiply  
To form a number we prefer,  
Rejoicing as an integer*

*We break free from our mortal bonds  
With the wave of magic wands*

*Our square root signs become unglued  
Your love for me has been renewed*

by David Feinberg



# Contents

<b>Introduction</b>	<b>13</b>
<b>1 Models and Phenomenology</b>	<b>17</b>
1.1 Standard Model . . . . .	17
1.2 HSCP Phenomenology and Models . . . . .	19
1.3 Previous Experimental Searches . . . . .	26
1.4 Conclusion . . . . .	28
<b>2 Collider and Detector</b>	<b>29</b>
2.1 The Large Hadron Collider . . . . .	30
2.1.1 Accelerator Complex . . . . .	31
2.1.2 Luminosity and Event Rate . . . . .	33
2.1.3 LHC Commissioning . . . . .	33
2.2 The Compact Muon Solenoid . . . . .	37
2.2.1 The overall detector . . . . .	39
2.2.2 CMS Coordinate conventions . . . . .	39
2.2.3 Superconducting Magnet . . . . .	40
2.2.4 Tracking System . . . . .	40

2.2.5	Electromagnetic Calorimeter . . . . .	43
2.2.6	Hadronic Calorimeter . . . . .	44
2.2.7	Muon System . . . . .	45
2.2.8	Trigger and data acquisition . . . . .	47
2.2.9	CMS Software . . . . .	49
2.2.10	Visualization Software . . . . .	50
2.3	Conclusion . . . . .	54
<b>3</b>	<b>Silicon Strip Gain Calibration</b>	<b>55</b>
3.1	Strip tracker sensor and readout chain . . . . .	55
3.2	Inter-calibration of gain . . . . .	61
3.2.1	Inter-calibration of gain with tick-marks . . . . .	62
3.2.2	Inter-calibration of gain with particles . . . . .	63
3.3	Absolute calibration of gain . . . . .	71
3.3.1	Using APV charge injection . . . . .	71
3.3.2	Using the tick-mark height . . . . .	72
3.3.3	Using energy deposit . . . . .	72
3.4	Conclusion . . . . .	75
<b>4</b>	<b>Particle identification and mass reconstruction with dE/dx</b>	<b>77</b>
4.1	Introduction . . . . .	77
4.2	dE/dx estimators . . . . .	80
4.3	Mass Reconstruction . . . . .	85
4.4	dE/dx discriminators . . . . .	88
4.5	Validation of the particle identification tools . . . . .	92
4.6	Cluster Cleaning Algorithm . . . . .	95
4.7	Conclusion . . . . .	99

<b>5 Search for Heavy Stable Charged Particles</b>	<b>101</b>
5.1 HSCP Signature . . . . .	101
5.2 Signal and Standard Model Background . . . . .	103
5.3 Online Selection . . . . .	104
5.4 Offline Selection . . . . .	108
5.5 Mass Reconstruction . . . . .	120
5.6 Data-Driven Background Determination . . . . .	121
5.7 Results . . . . .	127
5.8 Systematic Uncertainties . . . . .	140
5.9 Perspectives . . . . .	141
5.10 Conclusion . . . . .	142
<b>Conclusion</b>	<b>143</b>
<b>Appendices</b>	<b>145</b>
<b>A FROG Visualization Software</b>	<b>147</b>
A.1 FROG File Format . . . . .	150
A.2 FROG Producer . . . . .	151
A.3 FROG Displayer . . . . .	152
A.4 FROG Features . . . . .	153
A.5 FROG Applications . . . . .	161
A.5.1 GASSTOF: The Ultra-Fast Gas Time-of-Flight Detector . . . . .	162
A.5.2 DELPHES: a Framework for the Fast Simulation . . . . .	164
A.5.3 ILD: The ILC Detector Design . . . . .	166
A.5.4 TOTEM: The TOTEM Experiment . . . . .	167
A.5.5 CMS: The Compact Muon Solenoid . . . . .	168
A.6 Conclusion . . . . .	170

<b>B Bethe-Bloch Approximation</b>	<b>171</b>
<b>Bibliography</b>	<b>172</b>
<b>List of Tables</b>	<b>181</b>
<b>List of Figures</b>	<b>183</b>

# Introduction

In this thesis, a model-independent search for Heavy Stable (or long-lived) Charged Particles (HSCPs) produced in  $pp$  collisions at  $\sqrt{s} = 7$  TeV by the Large Hadron Collider (LHC) and recorded by the Compact Muon Solenoid (CMS) experiment is presented.

The HSCPs particles are predicted by various extension of the Standard Model (SM) of the fundamental interactions among elementary particles. Despite the overall excellent agreement between the predictions of the SM and the observations from previous experiments, there are several issues that indicate the necessity for physics Beyond the Standard Model (BSM). Many models solving some of the SM issues predict the existence of new exotic particles that may be created at the Large Hadron Collider (LHC), and in particular, some of them predict the existence of HSCPs.

Given their high mass, when produced at the LHC, the HSCPs are generally non-relativistic particles with high momentum. Therefore, their ionization energy loss is expected to be large compared to the SM stable particles of similar momentum. The high ionization is the main HSCP signature exploited by the search presented in this document.

The LHC entered successfully in operation just a few months ago. The first  $pp$  collisions it produced were recorded by the CMS detector and then used for the calibration, alignment, and more generally, understanding of the detector. The collision data taken at  $\sqrt{s} = 7$  TeV, that were first produced at the beginning of April 2010, are exploited in this search for HSCP.

A short introduction to the Standard Model and few motivations for physics Beyond the Standard Model are given in the first chapter of the thesis. Then, despite the completely model independence of the techniques used in this search, a couple of theoretical models predicting HSCPs are also listed; these models are useful to produce

benchmark of simulated HSCP events. The phenomenology and the current upper limits on the production cross-section of the HSCP can also be found in this chapter.

The second chapter is focused on the experimental frame of this research. First, the main features of LHC will be detailed. In the second part, a global description of the CMS detector is given.

In this analysis, the particle ionization energy loss is measured using the silicon strip tracker (SST) detector. The SST is the largest silicon detector ever built, it is made of 200 m<sup>2</sup> of pure silicon, and one of the most complex subdetector of CMS. The HSCP identification based on the energy loss is possible only if all the SST sensors give a same signal to a same amount of energy released by the particle crossing the sensor. Therefore, a precise inter-calibration of the SST is needed as well as an absolute-calibration of the SST. The later is needed to convert the energy loss from an electronic unit into a physical unit: the number of MeV released by the passage of the particle by units of the particle path-length in the silicon. All these calibration procedures as well as the SST read-out chain are detailed in the chapter 3.

The chapter 4 details the tools that have been developed in order to estimate the ionization energy loss of a charged non-relativistic particle and to discriminate highly ionizing particles from minimum ionizing particles using the SST. The use the measured ionization energy loss and particle momentum for particle identification and mass reconstruction is also presented. The performance of the developed techniques are shown for the identification of low momentum hadrons produced in *pp* collisions.

The last chapter is dedicated to the main analysis: an early signature-based search for HSCP in *pp* collisions. The analysis exploits the very first data from the initial LHC run from April-July 2010, at  $\sqrt{s} = 7$  TeV, corresponding to an integrated luminosity of about 3.06 pb<sup>-1</sup>. The analysis isolates HSCP candidates by selecting tracks reconstructed in the inner tracker detector with high ionization energy loss and high transverse momentum. A second selection additionally requires that the tracks are loosely identified as muons. For both selections, the mass of the HSCP candidates are reconstructed from the measured track momentum and ionization energy loss. A counting experiment is finally performed to search for excess in data compatible with an HSCP signal.

The Appendix A is dedicated to an event data visualization tool, FROG, developed in the context of this Ph.D. but not directly related to the search for HSCPs. Event data visualization is frequently the best approach for the understanding of subtle effects affecting the detectors, event reconstruction algorithms or even unlikely physical processes. The development of FROG started because the visualization software of the CMS framework was not efficient enough to be really usable by standard physicists. The source of the official program inefficiencies were quickly identified as the result

of the full integration of the visualization software in the CMS framework. The philosophy of FROG was therefore to completely decouple the visualization software from the experiment framework. Some of the many side advantages that naturally come out from the chosen strategy are described in this appendix. The tool was intensively used for the detector commissioning and understanding. And also revealed to be of precious help for the search for HSCP where it was used to cross-check results.

The work presented in this thesis is essentially based on the following publications:

- "Search for Heavy Stable Charged Particles in pp collision at  $\sqrt{s} = 7$  TeV"  
*G. Bruno, L. Quertenmont, A. Rizzi et al*  
CMS-AN-2010/194 (associated to CMS-PAS-EXO-10-004)
- "Search for Heavy Stable Charged Particles with the CMS inner tracker"  
*G. Bruno, A. Giannanco, L. Quertenmont*  
CMS-AN-2010/053 (associated to CMS-PAS-EXO-10-004)
- "Ionization energy loss and particle-id performance of the Silicon Strip Tracker with 900 GeV data"  
*G. Bruno, A. Giannanco, L. Quertenmont*  
CMS-AN-2010/20 (associated to CMS-PAS-TRK-10-001)
- "Commissioning and Performance of the CMS Silicon Strip Tracker with Cosmic ray muons"  
*The CMS Collaboration*  
2010 JINST 5 T03008, arXiv:0911.4996v2
- "FROG: The Fast and Realistic OpenGL Event Displayer"  
*L. Quertenmont, V. Roberfroid*  
CMS-NOTE-2009/007, arXiv:0901.2718v1
- "Search for Heavy Stable Charged Particles with  $100 \text{ pb}^{-1}$  and  $1 \text{ fb}^{-1}$  at CMS experiment"  
*G. Bruno, L. Quertenmont, A. Rizzi et al*  
CMS-AN-2007/049 (associated to CMS-PAS-EXO-08-003)



# Chapter 1

## Models and Phenomenology

In this chapter, the Standard Model of particle physics is described, followed by a brief introduction to the model extensions that predict the existence of Heavy Stable (or quasi-stable) Charged Particles (HSCP). These models of physics Beyond the SM are frequently used as benchmarks for the HSCP analysis. Finally, the current limits from previous experimental searches for HSCP will also be given.

### 1.1 Standard Model

The Standard Model (SM) of particle physics [1] is a relativistic quantum field theoretic model that describes the constituents of matter - point-like particles and forces that govern their interactions. It is based on a Lagrangian symmetric under  $SU(3) \times SU(2) \times U(1)$  gauge transformations with a vacuum that spontaneously breaks these symmetries.

The model describes three fundamental interactions (electromagnetic, strong, and weak) between the elementary particles that make up all known matter. Matter particles, fermions (spin 1/2), interact by the exchange of force carrier particles, the bosons (spin 1). A schematic representation of the SM particle content is illustrated on Figure 1.1.

The fermionic sector of the Standard Model consists of three generations of four particles: 2 leptons and 2 quarks. Different generations only differ by the particle masses that are higher at each generation. Ordinary matter is only composed by particles of the first generation. Particles of the second and the third generation are unstable and

decay relatively quickly in particles of the first generation. In addition to the mass, the particles are characterized by a set of quantum numbers including the electric charge, the weak charge (Isospin) and the strong charge (color).

All bosons, except the Higgs, are carriers of one of the three fundamental interactions: massless photons mediate the electromagnetic interaction, and the massive  $W^+$ ,  $W^-$  and  $Z$  particles the weak interaction. Additionally, there exist eight massless gluons as carriers of the strong force. The Higgs boson arises as a consequence of spontaneous symmetry breaking in the process of giving masses to other particles. Finally, all the leptons in the Standard Model are accompanied by anti-particles of opposite quantum numbers.

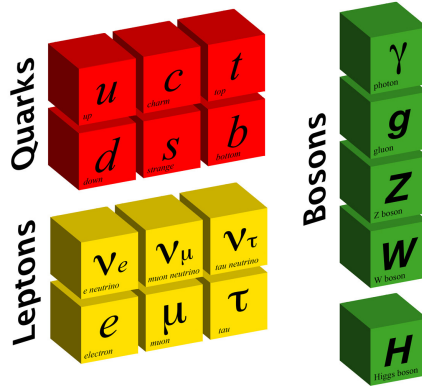


Figure 1.1: Schematic representation of the particle content of the Standard Model

Despite the overall excellent agreement between the Standard Model and experiment, there are several issues that indicate the necessity for physics Beyond the Standard Model (BSM). The SM would remain an effective field theory below the current energy scales ( $\sim 1$  TeV).

The main motivations for BSM models are the various issues affecting the SM like the fact that the SM can not describe the gravitational interaction [1] or that the existence of dark matter and dark energy, that make up 96% of the energy density of the universe, can not be explained [2] or also the SM neutrinos are mass-less particle while the experimental observation indicates that neutrinos are massive particles [3] or even that the unification of the three gauge couplings at the Planck scale does not occur in the SM [4, 5].

## 1.2 HSCP Phenomenology and Models

Heavy Stable Charged Particles (HSCP) arise in models in which one or more new states exist and carry a new conserved, or almost conserved, global quantum number. Supersymmetry with R-parity and extra dimensions with KK-parity provide examples of such models [6].

The lightest of the new states will be stable, due to the conservation of this new parity and depending on quantum numbers, mass spectra, and interaction strengths, one or more higher-lying states may also be stable or metastable. In general, electrically-charged stable states are incompatible with the dark matter problem [6], and colored particles are strongly constrained. For this reason, models that address the dark-matter problem generally have their Lightest Stable Particle (LSP) neutral. Cosmological observations also favor the LSP to be weakly interacting. But in addition to this neutral massive ( $M > 100 \text{ GeV}/c^2$ ) LSP, some extensions to the SM predict one or more higher-lying metastable charged states.

Despite the fact that the search described in this dissertation is completely model independent, benchmark models are useful in order to set experimental exclusion lower limit on the HSCP mass. Four benchmark models are used to study the HSCP discovery potential and set exclusion limits:

- The Split SUper Symmetric model (split SUSY) [7] predicts, in some regions of the parameter space, pair produced stable gluinos ( $\tilde{g}$ )
- The Minimal Super Symmetric Model (MSSM) [8] predicts, in some regions of the parameter space, pair produced stable stops ( $\tilde{t}_1$ )
- The minimal Gauge Mediated Supersymmetry Breaking model (mGMSB) [9] predicts stable staus ( $\tilde{\tau}_1$ )
- The Minimal Universal Extra Dimension model (MUED) [10] predicts pair produced Kaluza-Klein (KK) taus ( $\tau_{kk}$ )

The possibility of an absolutely heavy stable charged particle is constrained by cosmological considerations. But long-lived particles on an experimental scale are only constrained by direct searches. Stable refers, here, to particle that have a lifetimes long enough to escape the detector before decaying.

HSCPs could be produced by the Large Hadron Collider as a result of direct pair-production processes or as final products of the decay chain of heavier exotic particles.

There are mainly two categories of HSCPs: lepton-like HSCP (e.g.  $\tilde{\tau}_1$  and  $\tau_{kk}$ ) and hadron-like (e.g. hadronized  $\tilde{g}$  and  $\tilde{t}_1$ ). Indeed, because they are colored, the HSCP

of the second kind will hadronize and form mesons, baryons or glue-balls. These hadronized states are generically called R-hadrons and are composed of SM partons but one heavy exotic parton ( $\tilde{g}$  or  $\tilde{t}_1$ ). Like standard hadrons, R-hadrons may undergo inelastic scattering from the nuclei of the material in the detector. Different models attempt to describe the nuclear interactions experienced in matter by R-hadrons. Figure 1.2 (left) shows, for four different models, the mean energy per nuclear interaction lost by an R-hadron. The different models predict energy losses around few GeV per hadronic interaction. In every model, the heavy parton ( $\tilde{g}$  or  $\tilde{t}_1$ ) acts only as a spectator, behaving as a reservoir of kinetic energy. The kinetic energy available to each hadronic interaction is typically only a small fraction of the total energy and is proportional to the ratio between light and heavy parton masses. Therefore, the passage of an R-hadron in the calorimeters is not expected to produce large energy deposits. Thanks to this, the lepton-like or hadron-like HSCP is highly penetrating, exactly like the muon. A frequent experimental strategy is therefore to require the HSCP candidates to have a muon-like experimental signature.

The nuclear interactions experienced by R-hadrons may cause the conversion of one species of R-hadron to another in two ways: baryon exchange or charge exchange, as shown in Figure 1.2 (right). This effect is generally referred to as "charge flipping". As a consequence of this phenomenon, the particle can have its electric charge changed and therefore become neutral or oppositely charged, see Figure 1.3 for an illustration of that effect. This charge flipping may therefore lead to a lower muon identification efficiency of the hadron-like HSCP.

Moreover, a recent study [11], on the modeling of the nuclear interactions suffered by HSCPs traveling in matter, shows that the probability for gluino or sbottom-based R-hadrons to emerge as neutral particles after traversing an amount of material typical of the calorimeters or iron yokes of the LEP, Tevatron [12] or LHC experiments is close to unity. If this prediction turns out to be correct, HSCPs of the kind mentioned above would not be observable at all in the muon systems of the experiments. Experimental strategies where the requirement of muon-like behavior for HSCPs is relaxed are therefore mandatory. The search described in chapter 6 is indeed designed to be sensitive both to muon-like HSCP and to HSCP undetected by the CMS muon system.

If the lifetime of new exotic particles is long (1 ns or more) compared to the transit time through the detector, then the particles may escape the detector, thereby evading the limits imposed by direct searches for decay products. However, a HSCP will be directly observable, if it does not become neutral due to charge-flipping, in the detector through the distinctive signature of a non relativistic, high momentum ( $p$ ) charged particle. The low velocity results in an anomalously long time-of-flight and large ionization-energy loss rate ( $dE/dx$ ). As anticipated earlier, since the particle

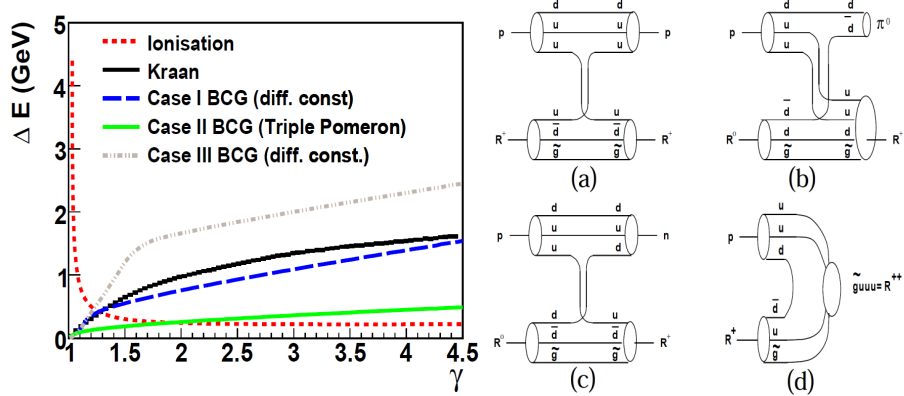


Figure 1.2: Left: Predictions from four phenomenological models of expected energy loss per nuclear interaction as a function of the Lorenz factor ( $\gamma$ ). The ionization energy loss corresponding to the passage of a R-hadron with charge  $\pm e$  through 18 cm of iron, which is equivalent to  $\sim 1$  interaction length, is also shown. Right: R-hadron-proton scattering processes. (a) Elastic scattering, (b) Inelastic scattering leading to baryon and charge exchange, (c) Inelastic scattering leading to charge exchange, (d) Resonance formation [6].

loses energy primarily through low momentum-transfer interactions, even if strongly interacting (R-hadron), it will be highly penetrating and will, experimentally, likely be identified as a muon. The long time-of-flight signature will not be used in the analysis presented in this thesis because the time-of-flight measurement, normally performed with the muon detectors, had not been commissioned at the time of writing.

The expected cross-section computed with PYTHIA [13] for the different benchmarks considered for pp collisions with a center of mass energy of 7, 10 and 14 TeV are listed on Table 1.1.

The distribution of transverse momentum ( $p_T$ ), pseudo-rapidity ( $\eta$ ) and velocity ( $\beta$ ) for different HSCP models and mass values are shown on Figure 1.4. All the details on signal simulation are given in section 5.2. Except light  $\tilde{\tau}_1$ , the HSCPs are mostly produced in the central region ( $\eta \sim 0$ ) with a  $\beta < \sim 0.85$ . HSCPs with a beta close to one are generally not produced in the central region. This feature is clear in Figure 1.5 where the distribution of  $\eta$  versus  $\beta$  is shown for some simulated HSCP samples.

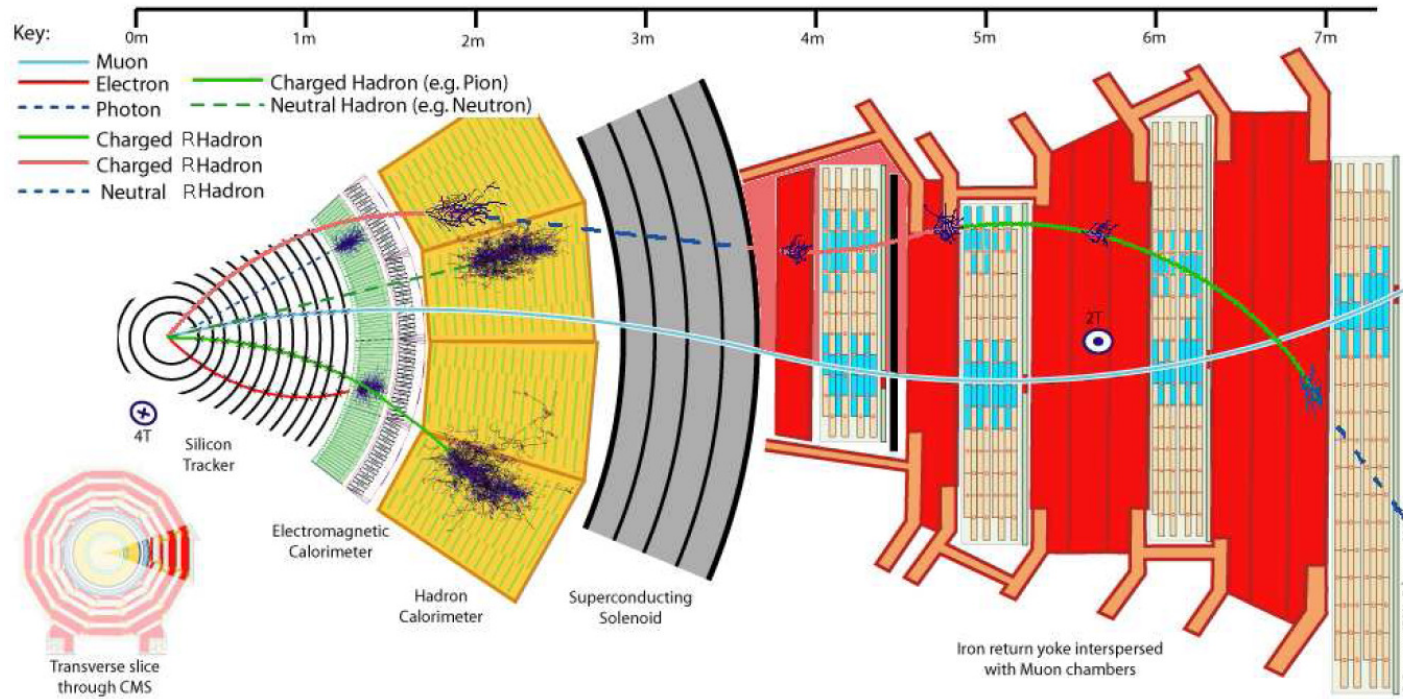


Figure 1.3: Illustration of a transverse slice of the CMS detector, see chapter 2. Expected signals from various (quasi-)stable particles are shown on this illustration, and in particular the signal created by a charged R-hadron that undergoes nuclear interaction and charge flipping in the hadronic calorimeter and in the iron yoke of the muon chambers. The curvature of the trajectory have been exaggerated to highlight the charge flipping effects.

Theoretical Model	HSCP	Mass (GeV/c <sup>2</sup> )	Expected Cross Section (pb)		
			$\sqrt{s} = 14 \text{ TeV}$	$\sqrt{s} = 10 \text{ TeV}$	$\sqrt{s} = 7 \text{ TeV}$
mGMSB	$\tilde{\tau}_1$	100	$1.23 \times 10^{+1}$	$4.27 \times 10^{+0}$	$1.34 \times 10^{+0}$
mGMSB	$\tilde{\tau}_1$	126	$3.50 \times 10^{+0}$	$1.12 \times 10^{+0}$	$3.35 \times 10^{-1}$
mGMSB	$\tilde{\tau}_1$	156	$1.13 \times 10^{+0}$	$3.46 \times 10^{-1}$	$9.85 \times 10^{-2}$
mGMSB	$\tilde{\tau}_1$	200	$2.81 \times 10^{-1}$	$8.25 \times 10^{-2}$	$2.26 \times 10^{-2}$
mGMSB	$\tilde{\tau}_1$	247	$9.27 \times 10^{-2}$	$2.75 \times 10^{-2}$	$7.75 \times 10^{-3}$
mGMSB	$\tilde{\tau}_1$	308	$2.68 \times 10^{-2}$	$8.21 \times 10^{-3}$	$2.14 \times 10^{-3}$
mUED	$\tau_{kk}$	300	$2.15 \times 10^{-2}$	$1.19 \times 10^{-2}$	$5.70 \times 10^{-3}$
split SUSY	$\tilde{g}$	200	$2.20 \times 10^{+3}$	$9.22 \times 10^{+2}$	$3.27 \times 10^{+2}$
split SUSY	$\tilde{g}$	300	$1.00 \times 10^{+2}$	$9.89 \times 10^{+1}$	$2.77 \times 10^{+1}$
split SUSY	$\tilde{g}$	600	$5.00 \times 10^{+0}$	$1.09 \times 10^{+0}$	$1.71 \times 10^{-1}$
split SUSY	$\tilde{g}$	900	$4.60 \times 10^{-1}$	$4.47 \times 10^{-2}$	$3.94 \times 10^{-3}$
split SUSY	$\tilde{g}$	1200	$6.10 \times 10^{-2}$	$3.26 \times 10^{-3}$	$1.69 \times 10^{-4}$
split SUSY	$\tilde{g}$	1500	$1.00 \times 10^{-2}$	$3.24 \times 10^{-4}$	$1.11 \times 10^{-5}$
MSSM	$\tilde{t}_1$	130	$3.35 \times 10^{+2}$	$1.56 \times 10^{+2}$	$6.55 \times 10^{+1}$
MSSM	$\tilde{t}_1$	200	$4.55 \times 10^{+1}$	$1.84 \times 10^{+1}$	$6.83 \times 10^{+0}$
MSSM	$\tilde{t}_1$	300	$5.88 \times 10^{+0}$	$2.16 \times 10^{+0}$	$6.48 \times 10^{-1}$
MSSM	$\tilde{t}_1$	500	$3.53 \times 10^{-1}$	$1.06 \times 10^{-1}$	$2.29 \times 10^{-2}$
MSSM	$\tilde{t}_1$	800	$2.04 \times 10^{-2}$	$4.11 \times 10^{-3}$	$5.42 \times 10^{-4}$

Table 1.1: Production cross-section computed with PYTHIA for the considered benchmarks.

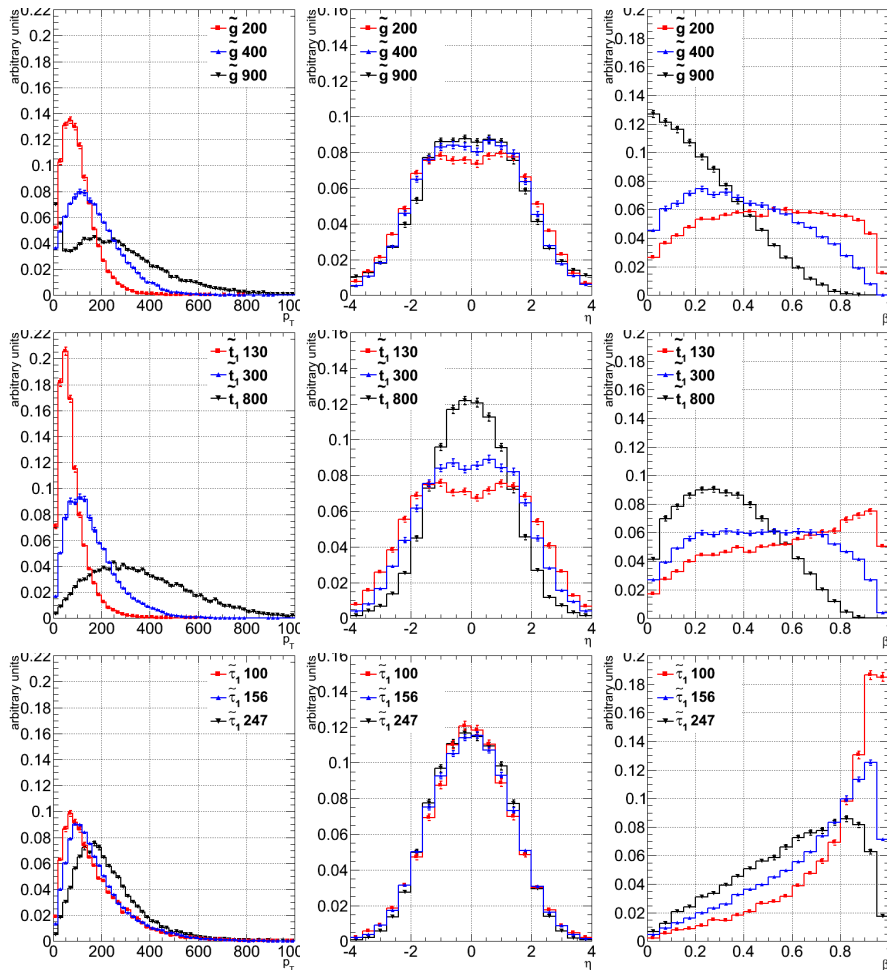


Figure 1.4: Distributions of, from left to right,  $p_T$ ,  $\eta$  and  $\beta$  for different models:  $\tilde{g}$  in split SUSY (top),  $\tilde{t}_1$  in MSSM (center) and  $\tilde{\tau}_1$  in mGMSB (bottom). For each model, three mass points are considered. Signal simulation is fully detailed in section 5.2.

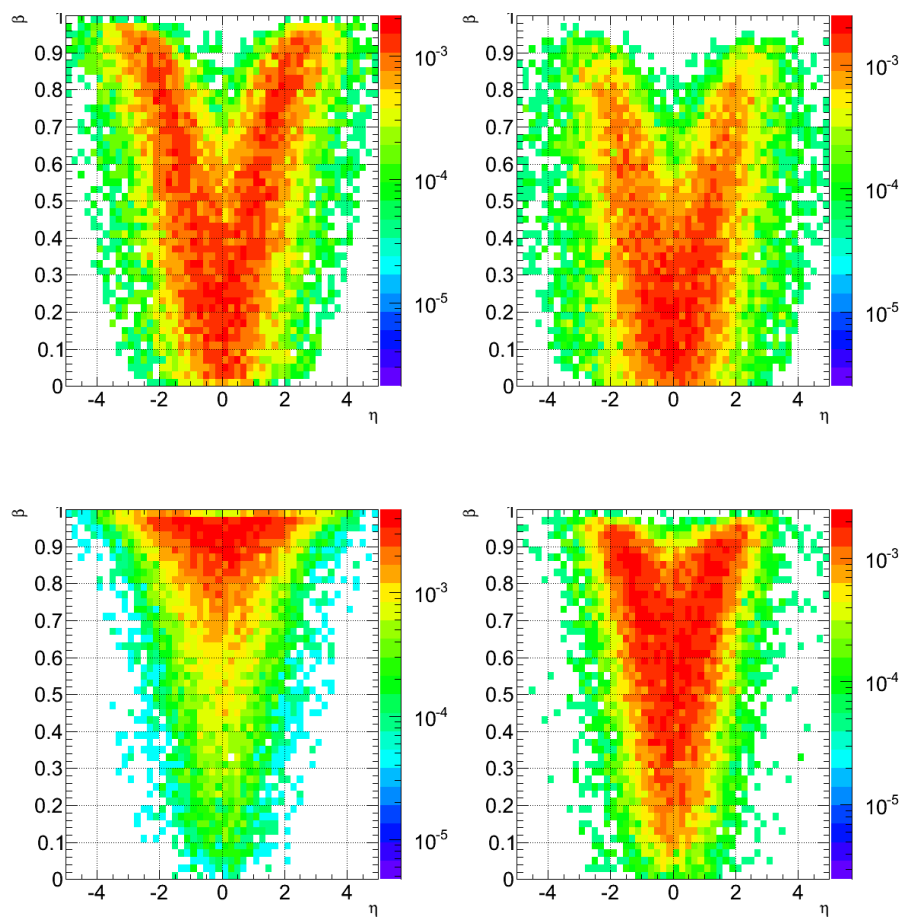


Figure 1.5: Distributions of  $\eta$  versus  $\beta$  for  $200 \text{ GeV}/c^2 \tilde{g}$  (top left),  $400 \text{ GeV}/c^2 \tilde{g}$  (top right),  $100 \text{ GeV}/c^2 \tilde{\tau}_1$  (bottom left) and for  $247 \text{ GeV}/c^2 \tilde{\tau}_1$  (bottom right).

### 1.3 Previous Experimental Searches

The most stringent mass limit on lepton-like HSCP came from the L3 detector at LEP2. It has fixed the lepton-like HSCP lower mass limit to  $90 \text{ GeV}/c^2$  at 95% C.L. [14], by mainly using ionization energy loss signature and assuming pair produced HSCPs in the L3 detector. Various theoretical hypotheses were tested [14], among which the presence of a fourth generation of leptons, these models will not be reviewed here.

A combined result from the LEP2 experiments has excluded a stable super-symmetric partner for SM leptons with a mass below  $99.5 \text{ GeV}/c^2$  at 95% CL [15]. These results have been extracted from  $e^+e^-$  annihilation with a center-of-mass energy of  $\sqrt{s} = 192 - 202 \text{ GeV}$  (in 1999) and  $\sqrt{s} = 202 - 208 \text{ GeV}$  (in 2000) corresponding to a total integrated luminosity of  $450 \text{ pb}^{-1}$ . Three candidate events have been observed while the number of background events was expected to be  $4.1 \pm 1.8$  events.

CDF and D0 collaborations have also performed searches for both strongly and weakly produced HSCPs in  $p\bar{p}$  collisions at  $1.8 \text{ TeV}$  using  $90 \text{ pb}^{-1}$  of data collected during Run I and set cross-section upper limits of about  $1 \text{ pb}$  at 95% C.L. for hadron-like HSCPs with masses up to  $250 \text{ GeV}/c^2$  [16, 17, 18, 19, 20]. CDF have also used  $dE/dx$  information for the HSCP identification.

CDF and D0 have not improved the limit on lepton-like HSCP due to a ten times lower production cross-section ( $\sim 0.1 \text{ pb}$ ) than at LEP ( $\sim 1 \text{ pb}$ ). The Figure 1.6 shows the L3 and CDF results. For hadronic HSCP, CDF has considered three different models to predict the lower cross-section limits. The  $q = 1/3$  and  $q = 2/3$  lines in the figure are cross-section limits for a fourth generation quark with an electric charge of  $1/3e$  or  $2/3e$ . The line labeled "w/o hadronization effects" is a fourth generation quark that does not undergo the hadronic interaction after it is produced, i.e. charge flipping is not allowed. The squarks used are from a generic fourth generation fermions model in PYTHIA.

Finally, the most recent CDF search [21] for super-symmetric top partner (stop), with  $1 \text{ fb}^{-1}$  of  $p\bar{p}$  Run II data at  $\sqrt{s} = 1.96 \text{ TeV}$ , has set a lower limit on the particle mass of  $249 \text{ GeV}/c^2$  at 95% C.L. using a time-of-flight measurement, see Figure 1.7. In addition, CDF has also set an upper limit on the production cross-section of single weakly (stop strongly) interacting HSCP to be less than  $10(48) \text{ fb}$  at 95% C.L. No exclusion limit on the gluino production cross-section has ever been published, however, Tevatron experiments could probably have been able to reject gluino with a mass below  $\sim 350 \text{ GeV}/c^2$ . This number is estimated by rescaling the CDF results on stop on the basis of the gluino production cross section.

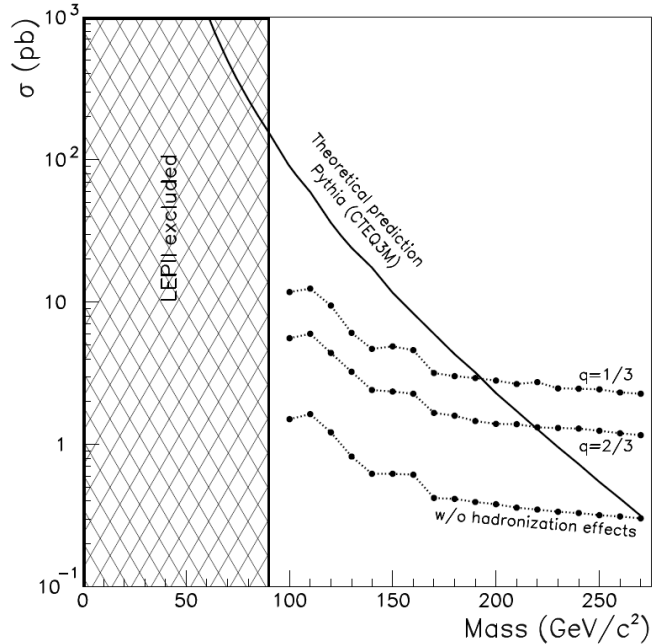


Figure 1.6: Limits set by the CDF collaboration at 95% confidence level on the production cross-section of long-lived fourth generation quarks are compared to the theoretical prediction [16].

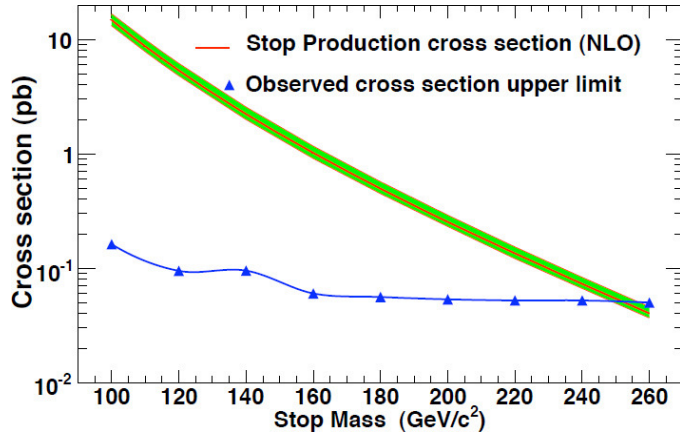


Figure 1.7: The observed 95% C.L. limits on the cross-section for production of a stable top-squark pair (points), compared to the theoretical NLO cross-section (curve). The band represents theoretical and parton distribution function uncertainties. The intersection of the band with the limit curve yields a lower mass limit for a stable top squark of 249  $\text{GeV}/c^2$  [21].

## 1.4 Conclusion

Heavy Stable (or long-lived) Charged Particles are predicted with high cross-section, up to  $\sim 100\text{pb}$ , in  $pp$  collisions at  $\sqrt{s} = 7 \text{ TeV}$ . Moreover, the HSCP phenomenology offers a unique signature which can be used with the early experiment data. It exploits the high transverse momentum of the HSCPs coupled to an anomalously high ionization energy loss and to a long time-of-flight. Both of them are consequences of the slowness of these heavy particles at the LHC. The time-of-flight measurement is not yet fully commissioned and is therefore not used in this thesis. Other experiments have succeed to set limits on HSCP production cross section by using these signatures (or only one of them). Current lower limits, from previous experimental searches, on the HSCP mass are 249 ( $\sim 350$ )  $\text{GeV}/c^2$  for stop (gluino) HSCPs and 90  $\text{GeV}/c^2$  for lepton-like HSCPs.

# Chapter 2

## Collider and Detector

The primary goal of the Compact Muon Solenoid (CMS) experiment [22] is to explore particle physics at the TeV energy scale, exploiting the proton-proton collisions delivered by the Large Hadron Collider (LHC) [23]. The complexity of CMS, like the other LHC experiments, is unprecedented.

The main motivation for the Large Hadron Collider (LHC) is to elucidate the nature of electroweak symmetry breaking for which the Higgs mechanism is presumed to be responsible. The exploration of the physics at the TeV scale is also the purpose of this accelerator. Presence of Heavy Stable Charged Particle (HSCP) is part of the new physics that may be discovered with the LHC.

The Compact Muon Solenoid is a multipurpose detector that aims at studying the new physic process and particles that may appear in the energetic LHC  $pp$  collisions. It is an outstanding detector for the search for HSCP because it can measure the track momentum with a relatively good resolution, in particular for muon-like particles, thanks to its precise muon tracking detector and the long lever-arm it offers. The same muon detectors also provide precise information on the particle time of arrival at the muon station; for particle produced at the  $pp$  collisions vertex, it is a measure of the particle time-of-flight. Finally, the high granularity of the CMS silicon tracker is also ideal to measure the particle specific ionization energy loss and therefore to identify HSCP.

## 2.1 The Large Hadron Collider

The Large Hadron Collider (LHC) [23], situated at the CERN research facility near Geneva, is a superconducting hadron collider that entered in operation in fall 2009.

Two counter-rotating beams of protons or heavy ions can be brought into collision at 4 interaction points. The accelerator is installed in the 26.7 km long circular tunnel that was built for the Large Electron Positron Collider (LEP) and is located between 45 m and 170 m underground near the French-Swiss border. The LHC consists of 8 arcs and 8 straight sections. The length of the straight sections is roughly 528 m and they can be used for either accommodate experiments or for other services. Figure 2.1 shows the geometry.

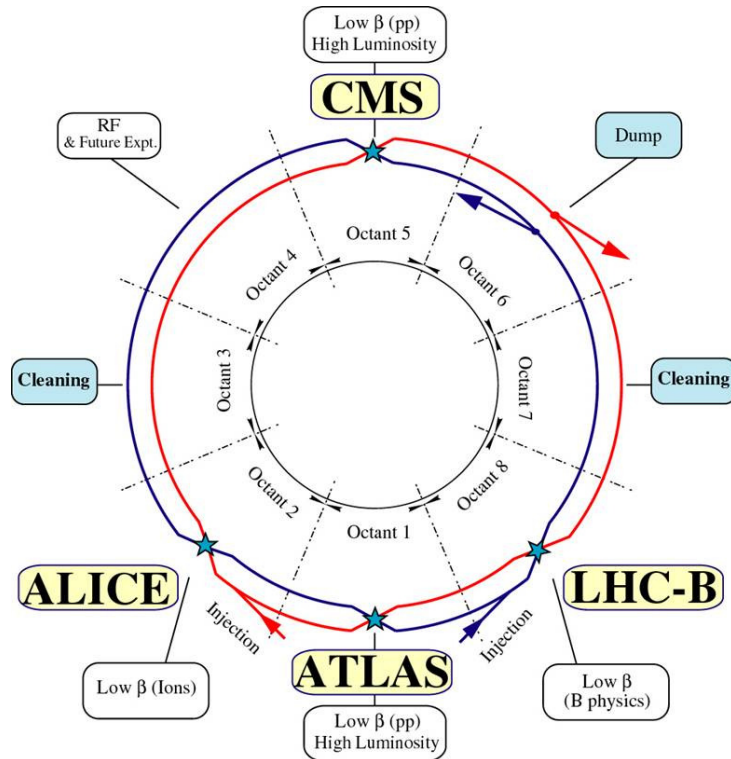


Figure 2.1: Illustration of the LHC geometry.

The particle beams can be crossed on 4 points along the ring, each equipped with one of the major particle detectors:

- ALICE (A Large Ion Collider Experiment)  
Studies Quark-Gluon-Plasma in heavy ion collisions.
- ATLAS (A Toroidal LHC Apparatus)  
One of the two general purpose experiments, looking for the Higgs boson, new physics and conducting precision measurements of the Standard Model.
- CMS (Compact Muon Solenoid)  
The second general purpose experiment, searching for the Higgs boson, supersymmetry or extra dimensions. Also performing detailed measurements of Standard Model processes.
- LHCb (LHC-beauty)  
Looking for CP-violation in the interactions of b quarks.

### 2.1.1 Accelerator Complex

The nominal energy of each proton beam is 7 TeV. To achieve this unprecedented energy, the protons need to be pre-accelerated before being injected into the LHC. The accelerator chain for protons consists of:

Accelerator	Acronym	Output Energy
Linear Accelerator 2	LINAC2	50 MeV
Proton Synchrotron Booster	PSB	1.4 GeV
Proton Synchrotron	PS	25 GeV
Super Proton Synchrotron	SPS	450 GeV
Large Hadron Collider	LHC	7 TeV

As shown in Figure 2.2, protons are obtained by removing electrons from hydrogen atoms and injecting them from the linear accelerator (LINAC2) into the Proton Synchrotron (PS) Booster. The protons accelerated at an energy of 26 GeV by the PS enter in the Super Proton Synchrotron (SPS), which brings protons to an energy of 450 GeV before injecting them into the LHC ring for the final acceleration step. Protons must circulate in the LHC for 20 minutes to reach the designed 7 TeV energy.

The radio-frequency (RF) [24] system is responsible for accelerating the proton beams from the SPS injection energy of 450 GeV to 7 TeV, as well as for maintaining this energy and keeping the bunch structure intact. The RF system consists of 8 separate superconducting cavities for each beam - centered at point 4 - delivering an electric accelerating field of 5 MV/m at approximately 400 MHz. The energy gain per turn and beam is 485 KeV.

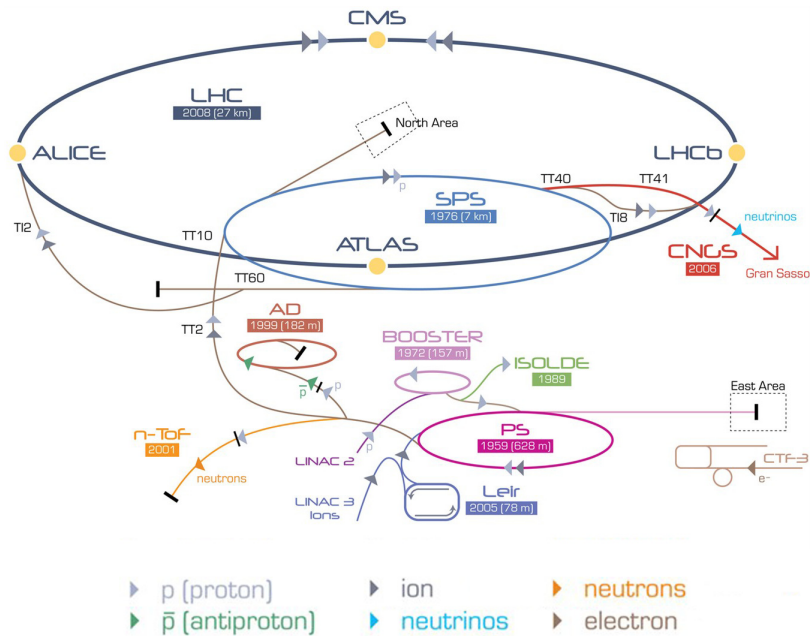


Figure 2.2: Drawing of the CERN accelerator complex. The LHC proton-injection-chain consisting of LINAC 2, Booster, PS and SPS can be seen.

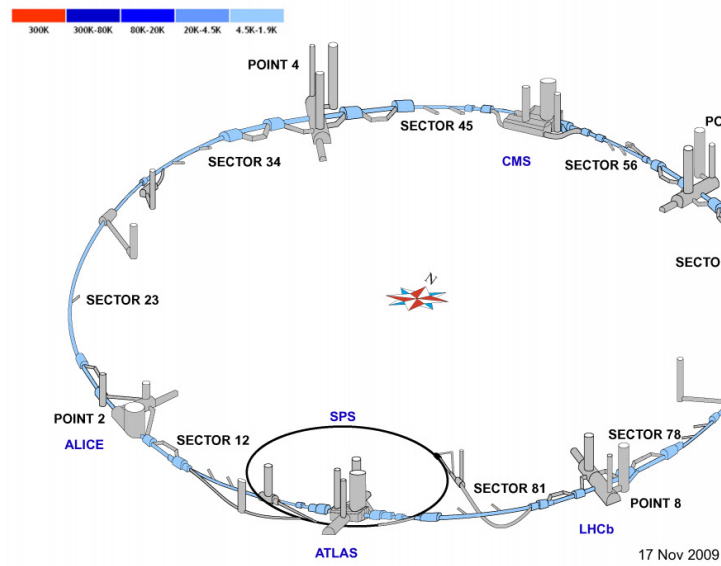


Figure 2.3: LHC Cooldown status on November 2009, just before the 2009 LHC run.

In order to keep the particle beams on track in the LHC ring, 1 232 superconducting dipole magnets are used. The nominal magnetic field during operation is 8.33 Tesla which is achieved by the use of NbTi cables, cooled down to 1.9 Kelvin by liquid Helium. Figure 2.3 shows the temperature map of the LHC just before the 2009 run. For optimal use of space and budget, the LHC has adopted a twin-bore approach for the superconducting magnets - the windings for both beam channels are contained in a single cold mass and cryostat. Additionally 392 quadrupole magnets will be used to focus the beam.

### 2.1.2 Luminosity and Event Rate

Given the proton bunch structure of LHC beams, the luminosity is given by:

$$\mathcal{L} = \frac{\gamma f N_B N_p^2}{4 \pi \epsilon_n \beta^*} F$$

where  $\gamma$  is the Lorentz factor,  $f$  is the revolution frequency,  $N_B$  is the number of bunches,  $N_p$  is the number of protons per bunches,  $\epsilon_n$  is the normalized transverse emittance,  $\beta^*$  is the betatron function at the IP and  $F$  is a reduction factor due to the non-null crossing angle of the beam and due to the complex bunch structures of the beams.

Some other parameters of interest are also listed, for the nominal LHC luminosity of  $10^{34} \text{ cm}^{-2} \text{s}^{-1}$ , in the Table 2.1.

The number of events per second is obtained using the luminosity and the specific cross-section of the process via:  $N_{\text{event}} = \mathcal{L} \times \sigma_{\text{event}}$ . Given the total proton-proton cross-section of 100 mb, the nominal luminosity leads to around  $10^9$  events per second.

### 2.1.3 LHC Commissioning

Currently, during the LHC commissioning phase, the number of bunches and the number of protons in each of them as well as the beam intensity are less than what is shown in Table 2.1.

As a consequence of the incident that occurred during the start-up in fall 2008, the decision was made to operate the LHC at 3.5 TeV per beam in 2010. But the accelerator commissioning started by collisions with a center-of-mass energy of 900 GeV and 2.36 TeV in December 2009. These successful runs were quickly followed by runs

**LHC Parameters**

Design Luminosity	$\mathcal{L}$	$10^{34}$	$cm^{-2}s^{-1}$
Proton Energy	E	7	TeV
Dipole Field	B	8.33	T
Bunch Separation		25	ns
No. of bunches	$k_B$	2808	
No. of protons per bunch	$N_p$	$1.15 \times 10^{11}$	

**CMS Collision Parameters**

$\beta$ -value at IP	$\beta^*$	0.55	m
R.M.S. beam radius at IP	$\sigma^*$	16.7	$\mu m$
Normalized transverse emittance	$\epsilon_n$	3.75	$\mu m$
Luminosity lifetime	$\tau_L$	15	hr
No. of collisions/crossing	$n_c$	$\sim 17.5$	
Reduction factor	$F$	0.88	

Table 2.1: LHC parameters relevant for the CMS detector

at the desired energy: The first collision at  $\sqrt{s} = 7$  TeV occurred on 30 March 2010 during the CMS Media event, where FROG (see Appendix A) was used to animate the first  $p\bar{p}$  collision in CMS for the international press. After that, the beam parameters were slowly modified to increase the instantaneous luminosity while keeping the total beam energy under a safety threshold, as described in Table 2.2. The important increase of the integrated luminosity with time is visible on Figure 2.4.

Date		$\beta^*$	$N_b$	$N_c$	$I_b$	$\mathcal{L} (cm^{-2}s^{-1})$
30	March	2010	10	2	1	$1.0 \times 10^{10}$
02	April	2010	10	2	1	$2.0 \times 10^{10}$
10	April	2010	2	2	1	$2.0 \times 10^{10}$
19	April	2010	2	4	2	$2.0 \times 10^{10}$
15	May	2010	2	6	4	$2.0 \times 10^{10}$
22	May	2010	2	13	8	$2.6 \times 10^{10}$
26	June	2010	3.5	3	2	$1.1 \times 10^{11}$
02	July	2010	3.5	6	4	$1.0 \times 10^{11}$
12	July	2010	3.5	8	4	$9.0 \times 10^{10}$
15	July	2010	3.5	13	8	$9.0 \times 10^{10}$
29	July	2010	3.5	25	16	$9.0 \times 10^{10}$
14	August	2010	3.5	25	16	$1.1 \times 10^{11}$
19	August	2010	3.5	48	36	$1.1 \times 10^{11}$
23	September	2010	3.5	56	47	$1.1 \times 10^{11}$
25	September	2010	3.5	104	93	$1.1 \times 10^{11}$
30	September	2010	3.5	152	140	$1.1 \times 10^{11}$
		2011	2	800	800	$1.5 \times 10^{11}$
						$3.7 \times 10^{32}$

Table 2.2: Summary of the modifications on the LHC beam parameters during the 2010 commissioning phase.  $N_b$  represents the number of bunches per beam while  $N_c$  represent the number of bunches colliding at ATLAS/CMS.  $I_b$  is the number of protons per bunch. The last line refers to the values that should be reached in 2011, the uncertainty on this extrapolation is obviously pretty large.

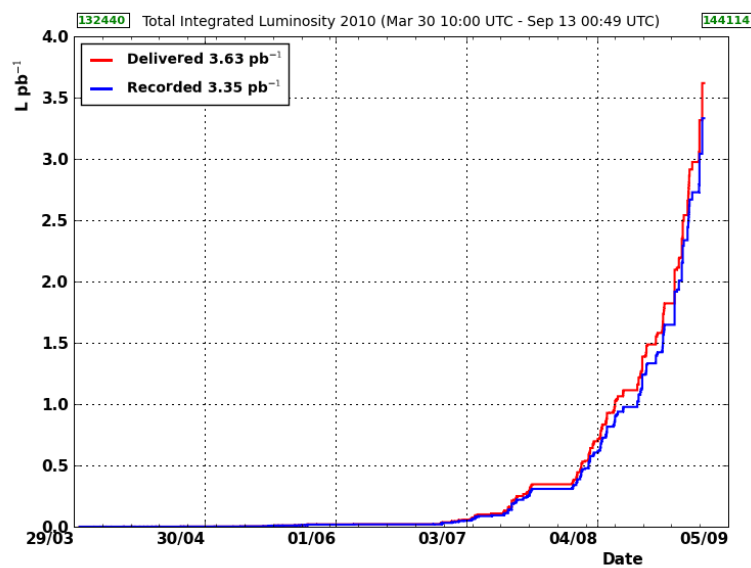


Figure 2.4: Integrated luminosity delivered by the LHC and recorded by CMS with a center-of-mass energy of 7 TeV.

## 2.2 The Compact Muon Solenoid

The Compact Muon Solenoid (CMS) detector [25], one of the two LHC general purpose experiments, is situated at Point 5, close to the French village of Cessy. The CMS collaboration is formed by approximatively 3600 collaborators from 183 institutes over 38 countries. The overall layout of CMS is shown in Figure 2.5 and in Figure 2.6. The Figure 2.7 is zoomed on the inner tracking system. CMS stands for:

- **Compact:** much less voluminous than ATLAS, CMS has a cylindrical shape with a diameter of 15 m and a length of 21.5 m for a total weight of about 12500 tons
- **Muon:** the detector is optimized for the measure of very energetic muons
- **Solenoid:** the detector is built around a big solenoid magnet. It has the particularity to be large enough to contain the tracker and the calorimeters

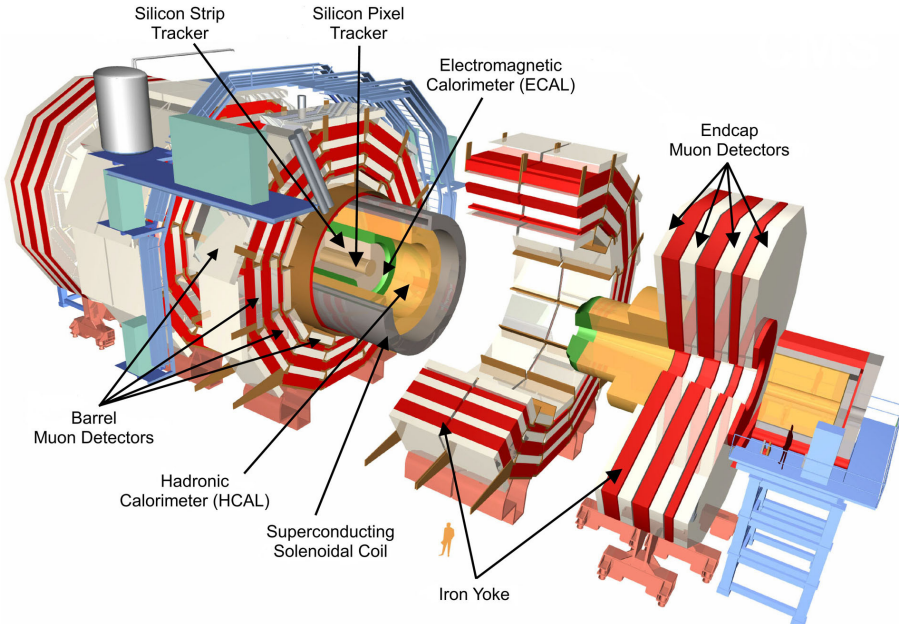


Figure 2.5: Tridimensional view of the CMS detector.

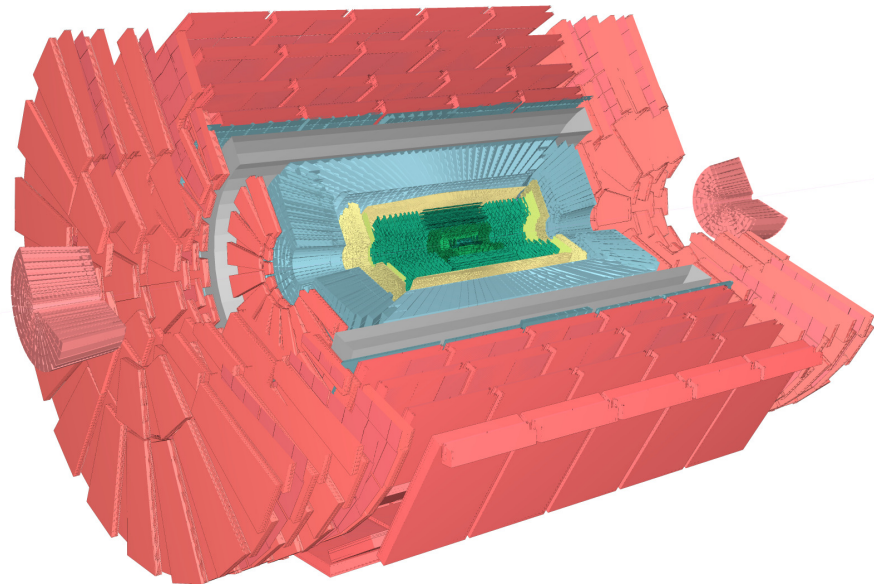


Figure 2.6: Two open views of the CMS Detector: from inside to outside, the pixel and strip silicon tracker (green), the electromagnetic calorimeter and pre-shower (yellow), the hadronic calorimeters (blue), the solenoid magnet (grey), the outer hadronic calorimeter (blue), the three muon systems (light red) and finally the forward calorimeter (light pink). This picture was obtained with FROG, see Appendix A.

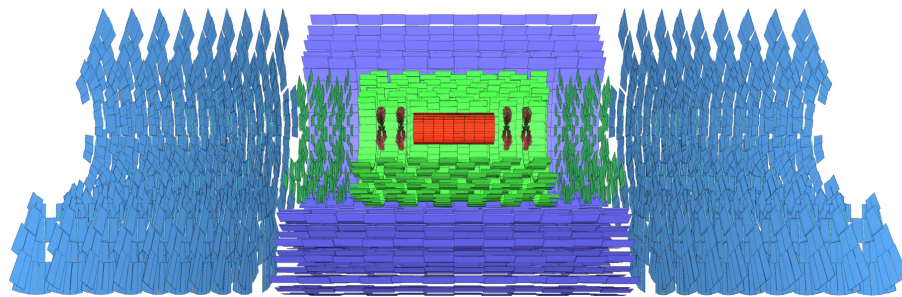


Figure 2.7: A view of the CMS Tracker: the Pixel Inner Barrel (PIB) is in red, and End-caps (PIE) are in light red, the Tracker Inner Barrel (TIB) is displayed in green while the Inner Disks (TID) are in light green. Finally, the Outer Barrel (TOB) and End-caps (TEC) are respectively colored in blue and in light blue. This picture was obtained with FROG, see Appendix A.

### 2.2.1 The overall detector

CMS is designed to identify and measure the energies and momenta of particles such as electrons, photons, muons and other collision products. Its main features are imposed by the physics analyses to be conducted:

- High precision measurement of muon momenta over a wide range as well as fast and reliable muon identification
- An electromagnetic calorimeter that allows a precise measurement of electron and photon energies and position
- A tracking system that provides good momentum resolution and track reconstruction for charged particles and the accurate measurement of primary and secondary interaction vertices
- A hadron calorimeter with almost hermetic coverage to detect the energies of hadronic particles and allow measurement of missing transverse energy

The detector consists of different sub-detectors, arranged in concentric layers around the interaction region, measuring different and complementary aspects of a collision event. The innermost layer is the inner tracking system, which is made of pixel and silicon strip detectors. It is followed by the electromagnetic calorimeter (ECAL) and by the hadronic calorimeter (HCAL). These three subdetectors fill completely the inner volume of the Solenoid Magnet. The outer parts of the detector are mainly composed of three kinds of muon chambers. In the forward region, close to the beam pipe, there is an additional forward part of the hadronic calorimeter, the very forward calorimeter (HF), but also a detector of the independent TOTEM [26] experiment.

The different subsystems will be reviewed in the following sections, but the CMS coordinate system and the CMS solenoid magnet will first be described.

### 2.2.2 CMS Coordinate conventions

The origin of the CMS coordinate system is centered at the nominal collision point. The  $y$ -axis pointing vertically upward and the  $x$ -axis pointing radially inward toward the center of the LHC. Since the frame is right handed, the  $z$ -axis points along the beam direction toward the Jura mountains. The azimuthal angle  $\phi$  is measured from the  $x$ -axis in the  $x$ - $y$  plane. The polar angle  $\theta$  is measured from the  $z$ -axis. Pseudorapidity is defined as  $\eta = -\ln \tan(\theta/2)$ . In the case of a massless particle,  $\eta = y$  where  $y$  is the particle rapidity:  $y = \frac{1}{2} \ln \left( \frac{E+P_z}{E-P_z} \right)$ . The rapidity has the property to

be invariant against Lorentz Transformation (Boost). For this reason, CMS physicists prefer to work in the  $R\text{-}\eta\text{-}\phi$  frame rather than in the  $x\text{-}y\text{-}z$  frame.

Note: The momentum and energy measured transverse to the beam direction, denoted by  $p_T$  and  $E_T$ , respectively, are computed from the  $x$  and  $y$  components.

### 2.2.3 Superconducting Magnet

The resolution on the particle-momentum measurement can be expressed as:

$$\frac{\Delta p_T}{p_T} \sim \frac{1}{BR^2} \text{ where } \begin{cases} B & \text{is the magnetic field in an orthogonal direction to the} \\ & \text{particle trajectory} \\ R & \text{is the tracker radius} \end{cases}$$

Resolution can therefore be improved either by building a larger detector or by opting for a high magnetic field. Tracking performance also relies on precise position measurements. A momentum resolution of  $\frac{\Delta p_T}{p_T} \approx 10\%$  is required for the charge sign determination of muons with a momentum of  $\approx 1$  TeV/c.

Since a part of the particle energy can be absorbed by the important material budget of the magnet, it has been chosen to measure the energy of the (highly interacting) particles in inner detector layers. For that reason, the internal radius of the CMS magnet must be large enough to host the tracking system and the two calorimeters. CMS chose a large superconducting solenoid magnet [27], which has a length of 12.9 m and a diameter of 5.9 m. A current of 19.5 kA is needed to generate the nominal magnetic field of 4 Tesla.

The magnet return yoke directly supports muon chambers and indirectly all subdetectors. This massive steel structure closes the magnetic loop. From the outer radius of the solenoid to the outer radius of CMS, a 2 Tesla magnetic field bends therefore muons trajectories in the reverse direction.

### 2.2.4 Tracking System

The main purpose of the inner tracking system [28, 29] is the accurate measurement of the tracks of charged particles - originating from the LHC collisions - and the identification of primary and secondary interaction vertices. This subsystem is of a capital importance for the identification of electrons, muons and hadrons.

Given that, at each bunch crossing (at high luminosity), the tracker is filled by  $\mathcal{O}(10^3)$  charged primary particles, the tracker granularity and time response are critical to allow the exact measurement of tracks and correct assignment of the bunch crossing. For

these reasons, the CMS Tracker is fully silicon based. Two technologies of detectors are in used in the tracking system because of the fast decrease of the particle density with the increase of the distance to the interaction vertex. Silicon pixel detectors are used in the closest region to the interaction vertex where a very high granularity is needed. The rest of the tracking system is made of silicon microstrip detectors.

In addition of the precise measurement of the particle crossing point position, the two subsystems can also be used to measure the amount of energy released by the particle in the silicon material. The latter feature makes possible the identification of the HSCP using the information of the energy loss in the silicon, see chapter 4.

A schematic view of the CMS Tracker detector is shown on Figure 2.8.

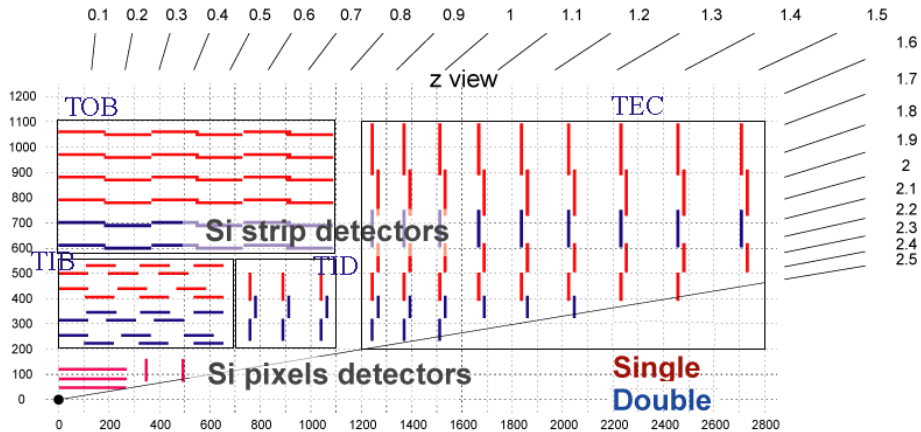


Figure 2.8: The CMS tracker detector layout (1/4 of the  $z$  view).

### Pixel Tracker

The pixel detector consists of the Pixel Inner Barrel (PIB) and of the Pixel Inner End-caps (PIE). The PIB is made of 3 layers located at a radius of 4.4 cm, 7.3 cm and 10.2 cm. The barrel has a length of 53 cm. The PIE is composed of 2 endcap disks on each side, placed at  $|z| = 34.5$  cm and 46.5 cm. This geometry allows for at least 3 tracking points over almost the complete tracker pseudo rapidity:  $|\eta| \leq 2.5$ . PIB (PIE) contains a total of 768 (672) pixel modules and about 48M (18M) single pixels yielding to a covered area of 0.72 (0.27)  $\text{m}^2$ . Thanks to the small size of the "square" pixels ( $100 \times 150 \mu\text{m}^2$ ), the measured spatial resolution is about  $10 \mu\text{m}$  in the barrel and about  $20 \mu\text{m}$  in the endcaps.

## Strip Tracker

Since the particle flux decreases with the radius, silicon micro-strip detectors of different sizes and pitches have been chosen for the outer layers. The tracker includes four subsystems:

- tracker inner barrel (TIB)
- tracker inner disks (TID)
- tracker outer barrel (TOB)
- tracker endcaps (TEC)

The TIB, consisting of 4 layers, occupies the radius up to 55 cm and is accompanied by 3 disks (TID) at each end.

The TIB is made of 4 layers and covers up to  $|z| < 65$  cm and  $20 < r < 55$  cm, the strip pitch varies from 80 to 120  $\mu\text{m}$ . In the TOB, the strips are longer and the pitch is wider, it varies from 180 to 120  $\mu\text{m}$  from inner to outer radius, the silicon module is also thicker. The TOB is made of 6 module layers located in  $|z| < 110$  cm and  $60 < r < 110$  cm.

Each TEC comprises 9 disks that extend into the region  $120 \text{ cm} < |z| < 280 \text{ cm}$ , and each TID comprises 3 small disks that fill the gap between the TIB and the TEC.

The barrel modules have strips parallel to the beam axis, while the endcap modules have strips in the radial direction, therefore TID/TEC modules have a variable pitch.

Unlike the pixel modules, the strip modules are only able to measure 2 coordinates of the particle tracking point. Indeed, the point of passage along the strip can not be measured. So the module in the barrel and endcaps only gives information, respectively, on the  $(r, \phi)$  and  $(z, \phi)$  coordinates. In order to provide a measurement of the third coordinate, additional micro-strip modules are mounted back-to-back to some parts of the strip tracker modules. These second modules are tilted with an angle of 100 mrad with respect to the standard module. The pair of modules is call a "stereo" module. They are placed on layers located at a radius of 20 – 30 cm and 60 – 70 cm, both of the barrel and endcap parts of the tracker, see Figure 2.8 for the exact layers position.

For the TIB (TOB), this montage leads to a single-point resolution of between 23–34  $\mu\text{m}$  (35–52  $\mu\text{m}$ ) in the  $r - \phi$  direction and 230  $\mu\text{m}$  (530  $\mu\text{m}$ ) in  $z$ .

As the radiation levels are smaller in the TOB region and in the 3 external disks of TEC, thicker silicon sensors (500  $\mu\text{m}$  instead of 320  $\mu\text{m}$ ) can be used to maintain a

good S/N ratio for longer strip length. The entire detector consists of almost 15400 modules which are installed in a temperature controlled (-20°C) tube. The Table 2.3 summarizes the main information related to the strip modules.

part	No. modules	$r$ position (cm)	$ z $ position (cm)	thickness ( $\mu\text{m}$ )	mean pitch ( $\mu\text{m}$ )
TIB	2724	$20 < r < 55$	$ z  < 65$	320	81/118
TOB	5208	$60 < r < 110$	$ z  < 110$	500	81/183
TID	816	$20 < r < 55$	$70 <  z  < 110$	320	97/128/143
TEC(1)	2512	$20 < r < 110$	$120 <  z  < 160$	320	97/126/128/143
TEC(2)	3888	$20 < r < 110$	$160 <  z  < 280$	500	143/158/183

Table 2.3: Detector type and position in the silicon strip tracker.

### 2.2.5 Electromagnetic Calorimeter

The electromagnetic calorimeter (ECAL) [30] is a hermetic, homogeneous crystal-based scintillating calorimeter. It is made of a barrel (EB) part and of 2 ECAL endcaps (EE). The goal of this detector is to precisely measure the energy of electrons and photons. In order to optimize the energy resolution of the calorimeter, the crystals must have the highest density and a small Molière radius. The lead tungstate ( $PbWO_4$ ) crystals chosen by the CMS collaboration have a Molière radius of 2.19 cm and a density of 8.28 g/cm<sup>3</sup>. Crystals of only 23 cm (22 cm) in the barrel (endcaps) are long enough to collect almost all the energy of the electrons thanks to the small radiation length ( $X_0 = 0.89$  cm) of the crystals. These radiation lengths are equivalent to  $\sim 25.8 X_0$  and  $\sim 24.7 X_0$ . EB is constituted by 200 crystals with a section of  $22 \times 22$  mm<sup>2</sup>, which is compatible with the Molière radius, covering the central region up to  $|\eta| < 1.479$  with a granularity of  $0.0174 \times 0.0174$  in the  $\Delta\eta \times \Delta\phi$  space. Each endcap, located at  $|z| = 314$  cm is made of 7324 crystals with a  $30 \times 30$  mm<sup>2</sup> extending the hermiticity of the detector to  $1.479 < |\eta| < 3.0$ .

In the region  $1.65 < |\eta| < 2.61$ , a preshower detector, made of silicon strips, is placed in front of EE. This additional detector allows to make the difference between an ECAL shower produced by a single photon and an ECAL shower produced by two close photons likely coming from a  $\pi_0$  decay. This detector is needed in the endcap region, mainly because of cinematic reasons but also due to the larger crystal section in EE.

For energy below 500 GeV, the ECAL energy resolution of the calorimeter can be expressed as:

$$\left(\frac{\sigma}{E}\right)^2 = \left(\frac{S}{\sqrt{E}}\right)^2 + \left(\frac{N}{E}\right)^2 + C^2 \text{ where } \begin{cases} E & \text{denotes the particle energy} \\ S & \text{is the stochastic term} \\ N & \text{is the noise} \\ C & \text{is the constant term} \end{cases}$$

In a test beam measurement, for a  $3 \times 3$  crystals super module, the typical values of  $S = 2.8\%$ ,  $N = 12\%$  and  $C = 0.3\%$  were found for  $E$  expressed in GeV [30]. For high energy ( $\sim 100$  GeV) electron/photon, the constant and stochastic terms are dominant. Those have been evaluated with first LHC data to be  $1.2\% \pm 0.1\%$  and  $7.1\% \pm 0.37\%$  for the barrel region [31].

## 2.2.6 Hadronic Calorimeter

The main function of the hadronic calorimeter (HCAL) [32] is to measure the energy and direction of hadrons. Associated with the ECAL calorimeter, HCAL increases the hermiticity of the CMS detector and thus gives information about the missing transverse energy ( $E_T$ ). This is one of the only variables sensitive to neutrinos and other weakly interacting particles that could be encountered in the search for new physics. Missing transverse energy measurement is the main motivation for the large pseudorapidity coverage ( $|\eta| < 5.3$ ) of HCAL. This sampling calorimeter is an alternance of thin absorber (brass or steel) layers and plastic scintillators layers. Copper brass was chosen for its relatively low Z, which minimizes multiple scattering for muons. It is also a non-magnetic metal, which is important since the calorimeter is placed within the 4 T solenoid. It consists of four subdetectors:

- HCAL Barrel (HB)
- HCAL Endcap (HE)
- HCAL Outer (HO)
- HCAL Forward (HF)

HB and HE completely surround the electromagnetic calorimeter. The barrel is 9 m long and consists of 2304 towers ( $\Delta\eta \times \Delta\phi = 0.087 \times 0.087$ ) covering the region  $|\eta| < 1.4$ . Projections of HB towers on ECAL correspond to a set of  $5 \times 5$  crystals. Copper plate thickness is 50 mm. Due to the limitations in volume, the coverage in radiation lengths of the HB is strictly constrained. The outer part of HCAL, installed just outside the solenoid, allows to increase it to over 10 interactions lengths in the central region ( $|\eta| < 1.26$ ), and thus to reduce the tails in the energy resolution function. Each hadron endcap consists of 2304 towers covering the region ( $1.3 < |\eta| < 3.0$ ). The  $\eta$

and  $\phi$  segmentations depend on the pseudorapidity.  $\phi$  segmentation varies between  $5^\circ$  and  $10^\circ$  while the  $\eta$  segmentation varies between 0.087 and 0.35. The (very) forward calorimeter completes the acceptance of the detector ( $3.0 < |\eta| < 5.0$ ). The HCAL thickness varies from 7.5 to 13 interaction length depending on the  $\eta$  region, which is enough to contain almost entirely the hadronic showers.

The uncorrected calorimeter (ECAL+HCAL) response can be parametrized via [33]:  

$$\frac{\Delta E}{E} = \frac{1.2}{\sqrt{E}} + 0.095$$
 where  $E$  denotes the energy in GeV.

## 2.2.7 Muon System

The muon system [34] is an integral part of the CMS detector - motivated by several appealing physics channels containing one or more final state muons and the possibility of using muons as a clear and fast trigger signal.

The CMS muon system (Figure 2.9) relies on three gaseous detector components:

- Drift tube chambers (DT)
- Cathode strip chambers (CSC)
- Resistive plate chambers (RPC)

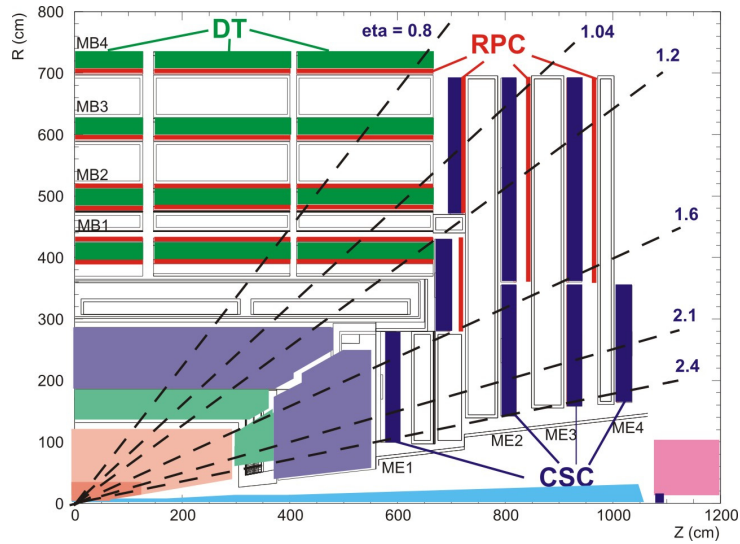


Figure 2.9: The CMS muon system layout (1/4 of the  $z$  view).

The drift tubes are used in the barrel region ( $|\eta| < 1.2$ ), where the muon rate is low and the residual magnetic field in the chambers is low. Drift tubes are suited to the barrel as the magnetic field is mainly contained by the return yoke. Almost all drift chambers are made of 12 planes of aluminum drift tube: 8  $r - \phi$  measuring planes and 4  $z$  measuring planes. Each chamber is designed to give a muon vector in space, with a  $\phi$  precision better than  $100 \mu\text{m}$  in position and approximately 1 mrad in direction. The DT subdetector consists of 5 wheels (slices in  $z$ ), each made of 4 layers of drift chambers. Chambers are staggered so that high- $p_T$  muon crosses at least 3 out of the 4 chambers.

In the endcaps,  $1.04 < |\eta| < 2.4$ , where the muon rate is higher and the magnetic field is larger and less homogeneous, drift tubes are replaced by cathode strip chambers. Cathode strip chambers are multiwire proportional chambers where the cathode is subdivided into strips perpendicular to the anode wires. Chambers are trapezoidal in shape and consist of 6 gas gaps, each gap having a plane of radial cathode strips and a plane of anode wires running almost perpendicularly to the strips. The gas ionization and subsequent electron avalanche caused by a charged particle crossing each plane of a chamber produces a charge on the anode wire and an image charge on a group of cathode strips. Thus, each CSC measures the space coordinates  $(r, \phi, z)$  in each of the 6 layers. The CSC subdetector is made of 4 stations of CSC chambers with an overlap in  $\phi$  to avoid gaps in the muon acceptance. Typical resolution of CSC are  $200 \mu\text{m}$  in position and approximately 10 mrad in  $\phi$  direction.

The good timing resolution of these drift detectors is very useful for the HSCP identification, since it allows to measure the arrival time of the particle at the muon station, and therefore it can be used to identify HSCP based on their anomalously high time-of-flight with respect to muons. Thanks to the detector timing resolution and to the great distance between the CMS interaction point and the muon stations, the particle time-of-flight can be achieved with a precision of the order of  $\sim 1 \text{ ns}$ .

In addition, RPCs are used both in the barrel and in the endcaps. This system is slightly faster and more robust, but has a less good spatial resolution. The RPCs information, redundant to the DT and CSC information, is used as additional sensitive planes. It is essentially used for trigger redundancy.

The best momentum resolution is obtained by combining information from the tracker to information from the various muon detectors, see Figure 2.10.

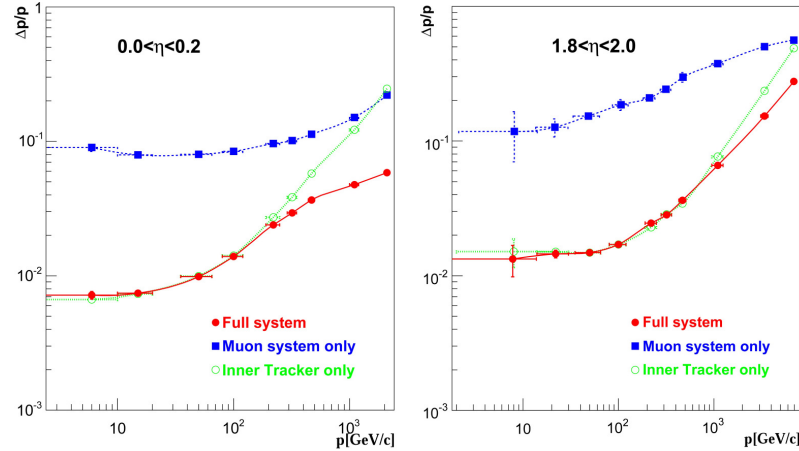


Figure 2.10: The muon momentum resolution versus  $p$  using the muon system only, the inner tracker only, or both for the central region ( $|\eta| < 0.2$ ) and the endcap region ( $1.8 < |\eta| < 2.0$ ).

### 2.2.8 Trigger and data acquisition

The LHC bunch crossing rate of 40 MHz leads to  $\sim 10^9$  interactions/sec (1 GHz) at design luminosity. It is impossible to store and process so many events. Also majority of those events are not interesting for the new physics search, since they are well-known elastic proton collisions,  $b\bar{b}$  or jets events. The primary goal of the CMS Trigger system is to analyze on the fly all the events produced in CMS and decide if they are interesting enough to be stored and post-processed later. CMS has the capacity to store about 100 events/sec (100 Hz). This decision is made in two steps.

#### Level-1 Trigger

The Level-1 (L1) Trigger [35] reduces the event rate by a factor 400. The L1 maximum output rates is fixed at 100 KHz. The events data are stored in a pipeline memory able to store up to 128 events. Given the 40MHz LHC event rate and the size of the buffer, the L1 Trigger has about  $3.2 \mu\text{s}$  to take a decision about one single event. This trigger is completely implemented in a dedicated electronic which allows fast decision taking in order to keep or discard the events in time.

The short decision time does not allow to exploit the CMS Inner Tracker information, while the other subdetectors are used but not with the full granularity. ECAL and HCAL information are organized in so called trigger towers having a size of  $0.087 \times$

0.087 in  $\Delta\eta \times \Delta\phi$  up to  $|\eta| = 1.74$  and being larger for higher pseudo-rapidities. The calorimeter information is used to compute few quantities on which the decision is based. Those quantities are particle candidates ( $e/\gamma, \tau, \text{jets}$ ) or global information such as total transverse energy ( $\sum E_T$ ) or missing transverse energy ( $E_T^{\text{miss}}$ ).

The three muon subsystems are taking part in the triggering but they are used separately. DTs are used to coarsely reconstruct 4 muon candidates. CSCs are similarly used to reconstruct 4 muon candidates in the forward region. RPCs are finally used to reconstruct 4 candidates in the central region and 4 in the forward region. Then the Global L1 muon trigger selects the 4 best candidates out of the 16 reconstructed muons and also makes use of the calorimeter information to check the isolation of the best muons.

The L1 global trigger bases its decision on simple logical operations based on the previously built quantities. The Figure 2.11 summarizes the Level-1 Trigger architecture.

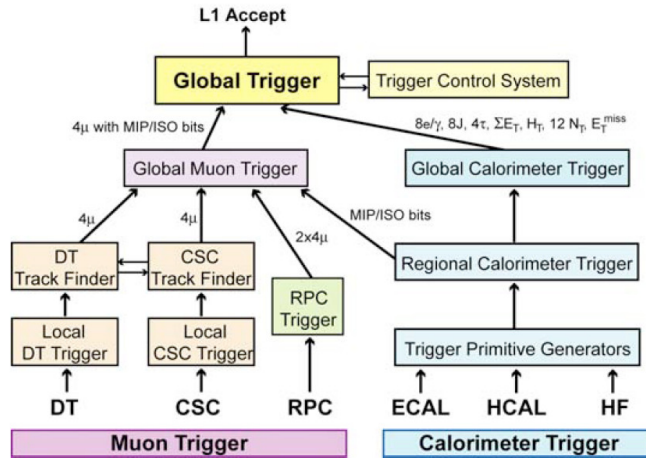


Figure 2.11: Box diagram showing the different components of the Level-1 Trigger.

## High Level Trigger

Unlike the L1 trigger, the High Level Trigger (HLT) [36] is purely implemented on software and runs on a cluster of commercial CPUs. Events selected by the L1 trigger directly enters in the HLT with an input rates of 100 KHz. The HLT is responsible for an event rate reduction of a factor 1000. Thanks to the first reduction, the HLT has

more time to take its decision and can thus use the complete detector information and more sophisticated algorithms.

The main trigger path for muon-like HSCP is obviously the muon trigger. However, the trigger efficiency in the muon detectors is limited by requirements on the arrival time of the tracks to the muon system. This requirement can affect the efficiency for detecting slow HSCPs. The muon trigger efficiency for HSCP is expected to start dropping linearly at  $\beta = 0.7$  and reaches very low values at  $\beta = 0.3$ . For lower  $\beta$  HSCP, the event can still be triggered by looking at the hadronic energy present in the event (Jet triggers) but also at the large expected missing energy ( $E_T$  triggers) since the un-reconstructed muon escape the detector with an important fraction of the energy. These two triggers are also used for strongly interacting HSCP becoming neutral in the muon system. More details on the trigger used for the HSCP search are available in section 5.3.

The available time to take a decision at HLT level is long enough to use a trigger path dedicated to HSCP. The latter can be based on a particle ionization energy loss measurement or even on its time-of-flight. Currently, none of these are currently used or implemented.

Events accepted by the HLT are stored on disks/tapes waiting for a complete processing and sharing all over the world.

### 2.2.9 CMS Software

The CMS Software [37] (CMSSW) is a set of tools and algorithms that are used for the event simulation and reconstruction. Giving a complete description of these tools is almost impossible since the software itself is continuously evolving.

The event simulation chain includes the following steps. First the event is generated, generally using a third party library like PYTHIA [13] and/or madgraph [38]. The generated particles are then propagated in the detector. The interactions of the particles with the CMS magnetic field and material are simulated at this using the Geant4 [39] framework. Then, the response of the sensor electronics is generated taking into account the energy released by the particle interactions simulated at the previous step. Last but not least, the CMS trigger system (L1+HLT) is finally emulated. The very last step is the encoding of the simulated data in "raw" data similar to the one sent by the CMS electronic for real events.

The event reconstruction chain is common to both real and simulated events. It is used to interpret the various electronic signal from the event readout into physical quantities or objects. Typically, at the end of the reconstruction, the particle tracks in

the inner tracking system and muon system have been identified. The energy released by particles in the calorimeter cells is aggregated to form energy clusters. Finally, the reconstructed tracks and energy clusters are used to reconstruct high level physics objects such as electrons, photons, Jets,  $E_T$ , muons, etc.

### 2.2.10 Visualization Software

In high energy physics experiments, and in particular in CMS, the possibility to visualize each event is crucial for several reasons. Understanding the event topologies can for instance help in developing better data analysis algorithms. It can also be used as a powerful debugging tool for the simulation and reconstruction experiment softwares. The ideal visualization tool has to be :

- fluid : draw > 60 frames per second
- fast : scan hundreds of events in few seconds
- light : the entire package should not exceed 10 MB
- easily upgradeable
- an intuitive debugging tool
- able to provide nice illustrations for the media, publications, etc.

Fulfilling simultaneously the above requirements could require heavy usage of all the resources of a computer. In general, these resources are the main limitation of the 3D visualization. In large experiments such as CMS [25], complex algorithms are used to reconstruct and analyze physics data. Since these algorithms are processor and memory consuming, a fast visualization tool should be decoupled from simultaneous physics calculations.

A generic visualization tool has been developed in the context of this thesis: the Fast and Realistic OpenGL event displayer [40] (FROG). It is based on a unique strategy where the visualization software is divided into a Producer and a Displayer, see Figure 2.12. This philosophy allows to easily satisfy the previous requirements, but it has also an impact on several other elements of the software, like the smart input file format, the operating system portability and the internal structure of the software. A dedicated FROG File Format (FFF) is needed in order to make the two parts of the code communicate with each other. It has to be highly compact, but the decoding time of the files has also to remain as limited as possible. Finally, the FFF should also be flexible enough. Its binary encoding ensures its universality with respect to the computer type and to the operating system.

The Producer is the interface between the physics software of the detector/experiment and the FROG Display. This code depends on the respective experiment software but it does not require specific graphical libraries. Its main task is to extract and process once for all the data that will be required by the Display to actually visualize the object data. For instance, it can convert the position of a hit from local coordinates of the detector to global coordinates. Such computations are in general relatively fast but can slow down the 3D visualization when repeated many times. The Producer creates two separates files, one containing the processed geometry data (`.geom`) and one containing the needed events data (`.vis`). This is the part that a user has to adapt in order to make FROG working for his particular experiment.

The Display has the unique function of displaying the content of the `.geom` and `.vis` files. It is completely independent from the experiment software. The Display can be distributed and run on different platforms: Windows, Linux and MacOS are currently supported. The only requirement to execute the Display is to use some graphic libraries such as OPENGL [41] and GLUT [42].

FROG is completely generic in the sense that it has been designed to be usable for any experiment and also to allow anyone to easily create plugins in order to use FROG for his particular case. It can therefore be used for any sort of applications and purposes. For this reason, FROG is used by the CMS collaboration, but also by other large communities like TOTEM [26], ILD [43] and CALICE [44] collaborations. Smaller projects are also exploiting the FROG flexibility, this is for instance the case of the DELPHES framework [45] and of the GASTOF [46, 47] detector.

More details about this visualization software, including a complete description of the FFF, of the Producer and of the Display, can be found in the Appendix A. A description of several of the FROG features as well as few applications of FROG in specific detector setups/environments are given in the same appendix.

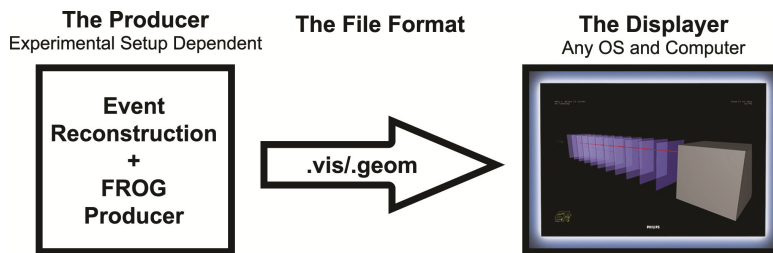


Figure 2.12: Factorization of FROG into the Producer and Display components. The Producer is integrated in the experimental software. It extracts, processes and stores the data required by the Display, using the FROG File Format for data encapsulation. The Display is completely disconnected from the experimental software.

An event display example of a simulated event, where a pair of stable  $200 \text{ GeV}/c^2$  gluinos is produced at CMS, is shown on Figure 2.13. The two produced gluino R-hadrons are charged in the CMS inner tracker, but one of two becomes neutral after the first DT layer due to the charge flipping mechanism. This track is therefore reconstructed as a "tracker muon", which is nothing but an inner track pointing to muon chambers with some activity.

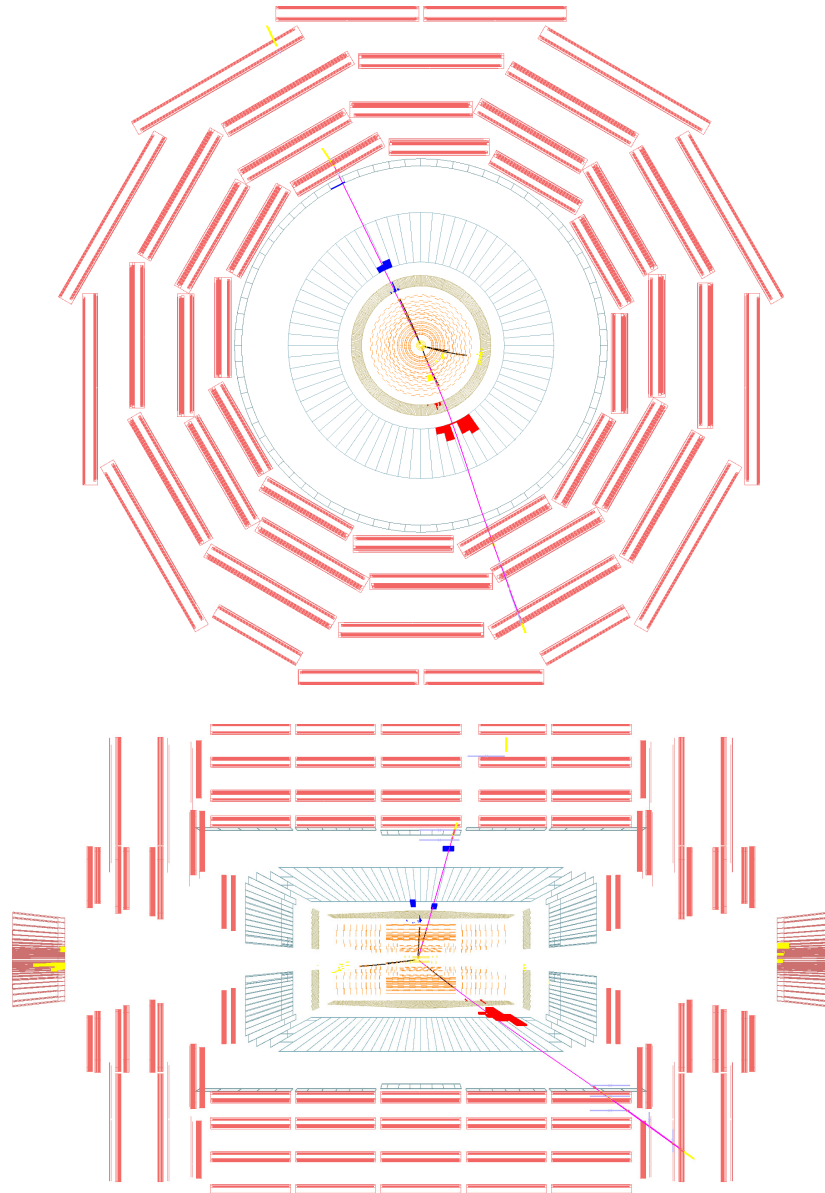


Figure 2.13: Transverse and longitudinal FROG views of simulated HSCP event. In this figure, the tracks associated to HSCP are shown in pink while the other tracks are shown in black. The two hardest jet in  $p_T$  of the event are shown in red (first jet) and blue (second jet), other jets are shown in yellow. The DT/CSC muon segments are displayed as thick yellow lines in the muon system and the RPC hits are displayed as light blue crosses.

## 2.3 Conclusion

The Compact Muon Solenoid is an outstanding detector which have many features ideal for the search for Heavy Stable (or long-lived) Charged Particles. The combining of the large muon system information with the inner tracker information allows to have a resolution on the particle momentum generally better than  $\sim 5\%$  for TeV particles. The precision of the CMS muon system can be used to measure the particle time-of-flight with a resolution of  $\sim 1$  ns. The silicon tracking system is capable to measure the particle energy loss through silicon. Given the large number of layers composing the inner tracking system, the number of energy loss measurement is expected to be large. If the detector is properly inter-calibrated, several measurements can be combined together in order to reduce the large fluctuation affecting individual measurement.

A so complex detector first needs to be understood before it can be used to seek for new physics. This is done by looking at well-known physics: cosmic muon ray and low energetic (900 GeV) proton collisions. Many of the subtle effects, that show up during the commissioning phase of the detector, are difficult to understand because they are the results of the correlation of many variables. The data visualization is an efficient tool to find correlations between various event properties.

The next chapter describes the Silicon Strip Gain Calibration that is required for particle identification based on ionization energy loss that is introduced in the chapter 4.

# Chapter 3

## Silicon Strip Gain Calibration

The charges released in the silicon sensors by the passage of a charged particle is processed by the readout electronics chain. The ratio of ADC counts output after digitization to the originally-released charge corresponds to the gain of the electronics chain. Particle identification using energy loss in the silicon detectors is known to be sensitive both to the absolute calibration scale and to gain non-uniformities. It is therefore important that these non-uniformities are corrected for and that the conversion factor between deposited energy and ADC counts is measured precisely.

The technique deployed for the search for Heavy Stable Charged Particles, see chapter 5, completely relies on the identification of HSCP based on the particle ionization energy loss. This identification method requires the use of the inter-calibration of the silicon (strip) tracker detectors detailed in this chapter.

### 3.1 Strip tracker sensor and readout chain

The Silicon Strip Module of the CMS tracker can be divided in two main components: the sensor and the readout electronics.

The sensor elements in the strip tracker module are single sided p-on-n type silicon micro-strip sensors with a thickness of  $320\ \mu\text{m}$  (TIB,TID,inner TEC) or  $500\ \mu\text{m}$  (TOB, outer TEC) [48]. When a charged particle crosses a sensor, it ionizes the silicon resulting in the creation of electron-hole pairs. The amount of energy needed for the creation of an electron-hole pair is  $3.61\ \text{eV}$  in a silicon at a temperature of  $-10^\circ\text{C}$  (operating temperature in CMS). At room temperature, the energy becomes  $3.62\ \text{eV}$ .

The charge created by this way are then collected on the sensor strips with an electric field generated by a difference of potential of 400 V between the two faces of each module. This induces a signal on the strips that can then be read by the electronics. It has been measured [49] that the effective silicon thickness is  $\sim 30 \mu\text{m}$  thinner than the actual sensor thickness.

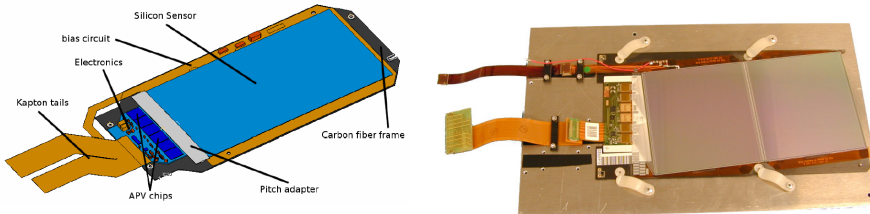


Figure 3.1: Left: Schematic drawing of a TIB silicon module with electronics, sensor and carbon fiber frame. Right: a picture of a TOB stereo module.

The electronics of a SST module is located on one of the two short edges of the sensor. The main components located here are:

- 6 or 4 APV chips
- 3 or 2 APV multiplexer (APVMUX)
- 1 PLL device
- 1 DCU device

The signals from the silicon sensors are amplified, shaped, buffered and processed by a custom readout chip, the APV [50]. This chip is the core of the SST electronic. Each sensor strip is connected to the APV through micro-bonds of the pitch-adapter. SST modules host 4 or 6 APV depending on the module width, each of them is connected to 128 strips. About 76 000 chips are needed to handle signals of strips of the 15 148 strip modules composing the CMS tracker.

The PLL is used to synchronize the electronics with the LHC clock and to set delays with respect to the CMS trigger. The PLL allows to set a fine (1 ns) and coarse (25 ns) latency to time-align all the modules to the same event. In fact, the different cable length and the position in the clock distribution chains introduce delays that must be taken into account and compensated.

The DCU is a chip that contains a unique ID for each module and 8 ADC channels to which different types of sensors can be connected. Those channels are typically used

to monitor electronics, sensor temperatures, leakage current and low voltage levels. A schematic view of the silicon strip tracker readout scheme is given in Figure 3.2.

Upon a positive first level trigger decision, the analogue signals of two APVs ( $2 \times 128$  channels) are multiplexed by an APVMUX and sent to the Linear Laser Driver (LLD) for transmission on the optical fiber. The LLDs convert analogical electrical signal into an analogical optical signal that is transmitted by the optical fiber to the Front End Driver (FED) boards. The 440 FEDs needed to read the  $\sim 10$  million channels of the SST are located, at  $\sim 100$ m from the module, in the service cavern. The FEDs are digitizing the signal using 10-bits Analog-to-Digital Converters (ADC). Clock, trigger, and control signals are sent to the electronics (APVs, FEDs, etc.) via optical links by one of the 46 Front-End Controllers (FEC).

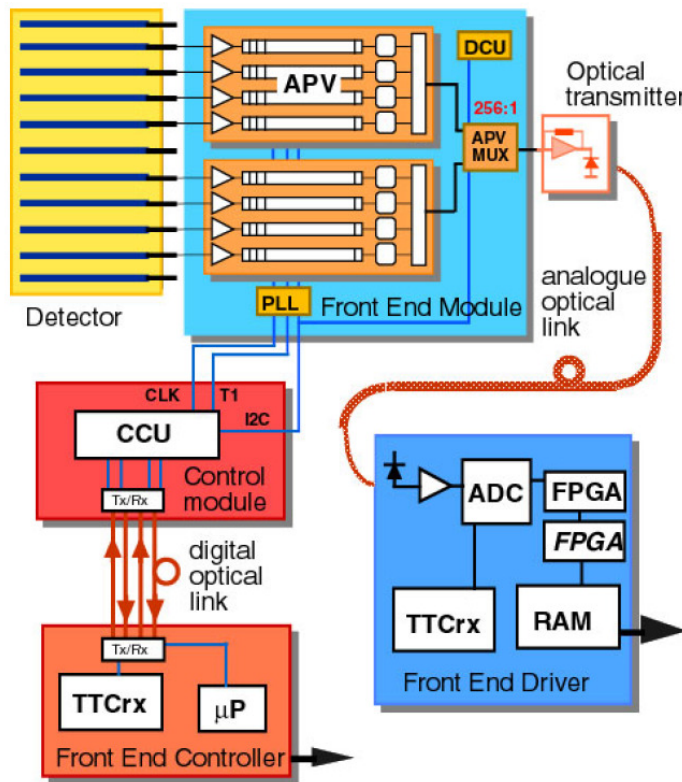


Figure 3.2: Readout scheme of the CMS strip tracker.

The APV readout channels consist of low noise and power charge sensitive pre-amplifier. The APV chip uses pre-amplifier and shaper stages working at the LHC frequency of 40MHz. The shaper stages produce a CR-RC pulse shape with a rela-

tively slow rise-time of 50 ns. The chip may run into two different modes: In peak mode, the signal is sampled at the maximum of the 50 ns pulse. In deconvolution mode, the signal is built out of a weighted sum of three consecutive samples. Despite the fact that it reduces signal-to-noise ratio, deconvolution mode is needed at high luminosity in order to confine the signal to the right bunch crossing. Deconvolution is the standard mode of operation. The two operating modes are characterized by completely different pulse shapes, see Figure 3.3.

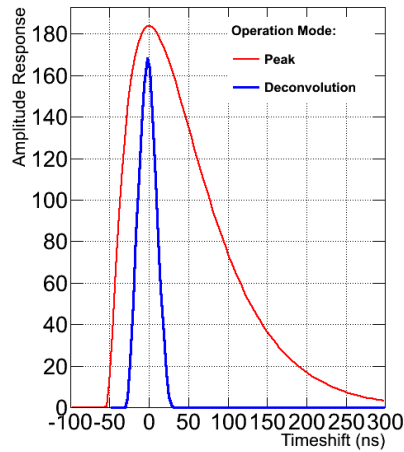


Figure 3.3: Signal amplitude for the two operating modes of the tracker as a function of the delay with respect to the ideal sampling time (at 0 ns).

In peak mode, the pulse have a much wider shape, it is therefore less sensitive to synchronization problem. The lost in the signal amplitude is negligible for a sampling time off by few nano-seconds in peak mode, but can be dramatic in deconvolution mode, because of its sharp shape. This have important consequences for slow particles like HSCPs. The signal amplitude and thus energy loss measurement, see chapter 4, can be significantly lower than the actual energy released by the particle in the silicon. The strength of this effect depends of the particle arrival time and therefore of the particle velocity, the Table 3.1. Therefore an HSCP of  $\beta = 0.6$  ( $\beta = 0.4$ ) in the forward region will reach the last silicon module ( $\sim 3\text{m}$ ) with a delay of 6ns (13.5ns).

Figure 3.4 shows an example of the raw data captured at 40 MHz by a single FED readout channel on receipt of a trigger. The data contain frames from two APV chips that are multiplexed together. A single frame starts by 12 bits of binary information that encodes time and error information, known as the digital header. It is followed by analogue pulse height data from  $2 \times 128$  sensor strips. Finally a trailing tick mark

Time (ns)	Signal Amplitude )	Time (ns)	Signal Amplitude
-2	98%	+2	98%
-4	93%	+4	93%
-6	85%	+6	86%
-8	74%	+8	79%
-10	64%	+10	71%
-12	54%	+12	63%
-14	45%	+14	53%
-16	37%	+16	43%

Table 3.1: Signal response for particle arrival time at the silicon sensor from -16 to +16ns. The amplitude is expressed in percentage the amplitude at optimal arrival time (=0ns).

identifies the end of the frame. The structure observed in the pulse height data across the  $2 \times 128$  channels is due to static offsets, known as pedestals, that are unique to each detector channel. Small, time-varying common mode shifts in the levels of all 128 channels are observed when operating. In the same figure, a signal left by a minimum ionizing particle is also visible. Signals are superimposed on the pedestal and common mode levels, that need to be subtracted before the signal can be identified. In the absence of a trigger, no data frame is sent by the APV chip, but tick marks are produced every 70 clock cycles. This feature is used heavily in the checkout and commissioning procedures. In standard operation mode, called Zero Suppressed mode, the FEDs perform pedestal and common mode subtraction and identify channels potentially containing signals above thresholds. A threshold of five times the detector channel noise is used for single channel, but a threshold of only twice the channel noise is used for signals in contiguous channels. The zero-suppressed data are output with an 8-bit range which therefore limits the maximal strip signal to 255 ADC counts. Actually, the values of 254 and 255 ADC counts are respectively used to encode that the signal measured for this strip is in the range [254,1023] and above 1023 ADC counts. This limitation of the signal amplitude by the FED is frequently referred to as the saturation effect.

Later, during the event reconstruction, the Zero Suppressed data are first calibrated in gain and then used to build strip clusters [25]. Clusters are reconstructed by searching for a seed strip with a signal to noise ratio  $S/N > 3$ . Nearby strips are included in the cluster if they satisfy  $S/N > 2$ . The total signal size of the cluster must exceed 5 times the square-root of the sum of the R.M.S.-noise-squared of the individual strips inside it. The position of the tracking hits, used for track reconstruction, is defined as the

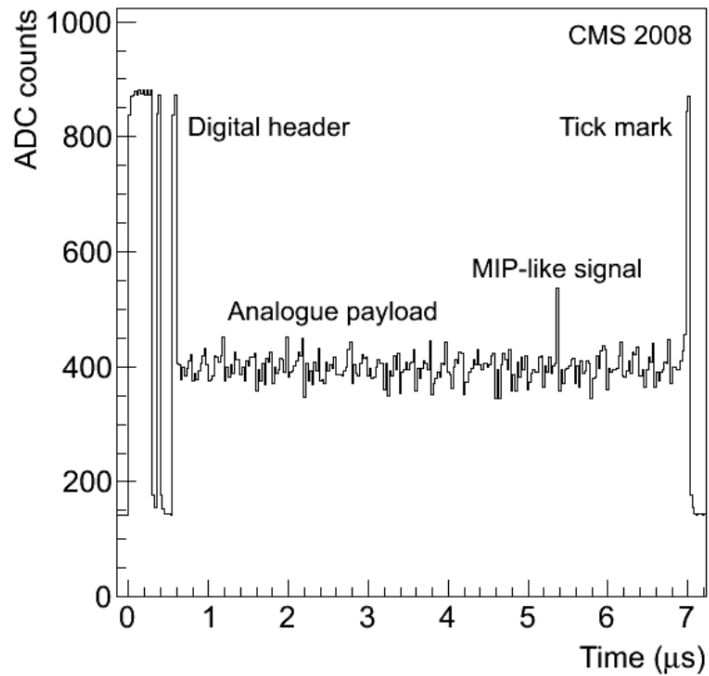


Figure 3.4: Two APV data frames multiplexed, containing a time stamp and the sensor pulse height information. The figure shows a sampling interval of 25 ns [51].

cluster charge barycenter. The cluster charge is defined as the sum of the individual charge of each strip composing the cluster, while the cluster size is just the number of strips composing the cluster. Another useful quantity is the cluster charge normalized for the path-length of the particle in the silicon. It is simply defined as the cluster charge ( $\Delta E$ ) divided by the path-length ( $\Delta x$ ). The path-length is a simple geometrical quantity, defined by  $\Delta x = L / \cos \theta$ , where  $L$  is the thickness of the silicon sensor and  $\theta$  is the angle between the track and the axis normal to the module, see Figure 3.5. The normalized charge,  $\Delta E / \Delta x$ , is frequently referred to as an energy loss measurement.

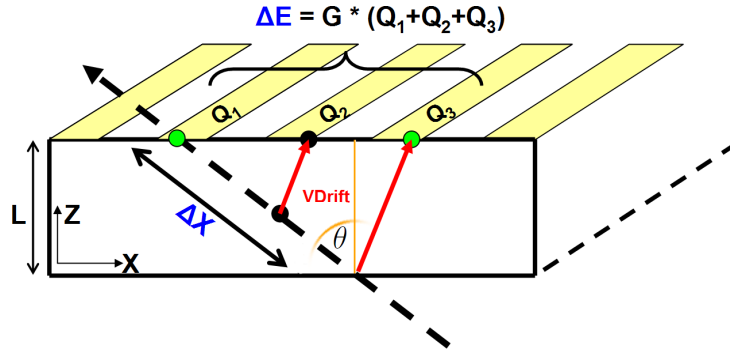


Figure 3.5: Illustration of a particle passing through a silicon sensor. Charged induced by the ionization of the silicon are collected on three strips forming a cluster of charge  $\Delta E = G(Q_1 + Q_2 + Q_3)$ , where  $Q_i$  is the charge induced on the  $i_{th}$  strip and  $G$  is the inter-calibration gain of this APV. The normalized cluster charge is given by  $\Delta E/\Delta X$  where is the path-length of the particle through the silicon.

## 3.2 Inter-calibration of gain

The silicon strip charge collection and signal amplification may be affected by a couple of effects like the temperature of the silicon, variation of the operating voltage of the sensor electronic, variation in the signal charge collection efficiencies due to radiation damages in the silicon wafers, time-drift in the laser output efficiencies, etc. All these effects are relatively stable with time but may differ from one module, laser or chip to another. However, a uniform and well-known response across all silicon detectors is important for a number of purposes:

- monitoring of variations in the detector response
- evaluation in an unbiased way of the position and error on the crossing point of charged particle
- particle identification based on ionization energy loss

The two main inter-calibration methods used by CMS are detailed in this section. The first method uses the tick-mark part of the APV pulse signal to equalize the detector response. The second method is based on the observation of minimum ionizing particles (MIP) for the inter-calibration.

### 3.2.1 Inter-calibration of gain with tick-marks

This method is entirely based on the use of the tick mark signal which is part of the APV data frame. The height of the tick mark signal (800 mV) is supposed to be identical for all the strip tracker chips and constant in time. In practice there is a variation from chip to chip of  $\sim 5\%$ . The FED captures the transmitted APV tick and its height is measured in ADC. In the hypothesis where no effect is affecting the overall readout chain, the 800 mV tick height sent by the APV should be reconstructed by the FED as a 640 ADC counts signal, since each FED corresponds to 1.25 mV. This hypothesis is in general wrong, therefore the overall readout link gain ( $G$ ) is determined by simply dividing the tick height measured by the FED in ADC counts by the expected value of 640 ADC counts. The value of  $G$  is then used as a gain to equalize the response of the system. The choice of 640 ADC counts as reference value is justified since it is the expected tick height produced by an APV, but another value could have been chosen.

The CMS readout system offers the possibility to use an approximate gain directly in the LLD chips, this gain is known as the AOH Gain. But a more precise gain can be used for offline reconstruction.

#### Online Gain

Four gain settings are possible in the LLD chip. The setting that results in a tick-mark amplitude closest to the target value of 640 ADC counts is chosen. Figure 3.6 shows the resulting (simulated) distribution of the tick-mark height. After tuning the system, a spread of 20% is observed [51], which is expected because of the coarse granularity of the LLD gain settings.

#### Offline Gain

An offline calibration of the electronic gain is necessary to improve the precision of the measurement of noise and signal. This is achieved by correcting the signal magnitude by the normalization factor [51]:

$$G = \frac{640 \text{ (ADC counts)}}{\text{TickMarkHeight} \text{ (ADC counts)}}$$

One limitation [49] in the use of this equation is due to the different module operating voltages for different layers. It was known that the tick-mark amplitude is linearly

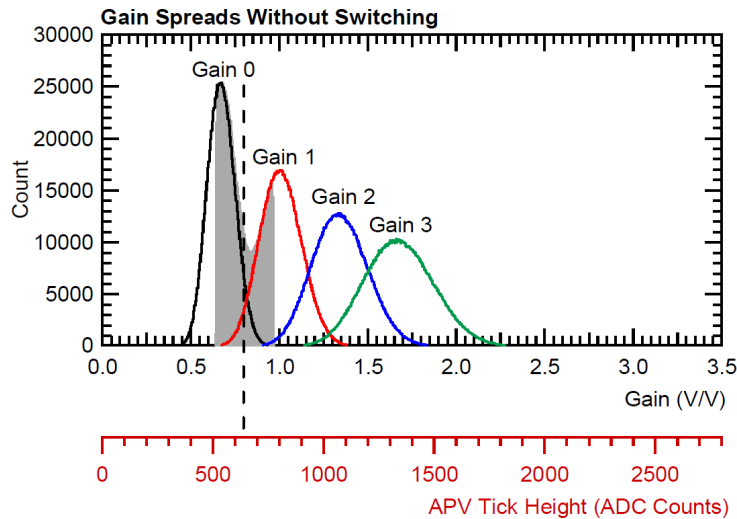


Figure 3.6: Simulation [52] of the tick-mark height distribution using each of the four possible gains (colored lines). The shaded area is obtained by choosing the AOH gain which brings the tick-mark height closest to its nominal value ( $800\text{ mV}=640\text{ ADC}$ ) represented by the dashed line.

proportional to the  $2.5\text{ V}$  operating voltage, therefore tick-marks from different modules can be compared only if they operate at the same voltage. The signal at the APV amplifier output is not much affected by changes in the supply voltage. Therefore to make a more precise estimation of the electronic gain, it is necessary either to equalize all the operating voltages or to correct the tick-mark value for the difference compared to  $2.5\text{ V}$ .

Another intrinsic limitation to this method is that it is only sensitive to effects that affect the signal between the APV and the FED, basically only signal modification induced by the optical connection can thus be probed.

The advantage of the method, both online and offline, is that new constants can be recomputed very quickly and so very frequently. It is therefore easy to monitor modifications of the gain run after run.

### 3.2.2 Inter-calibration of gain with particles

As said in the previous section, the gain inter-calibration method based on tick-marks is completely blind to many effects that are known to modify the signal amplitude: non-uniformities in the sensor response to a particle going through, damages in the

silicon induced by the radiations, non optimal sampling time of the strip signal (due to bad trigger synchronization), wrong depletion of the sensor, etc.

In order to solve all these weaknesses, a more robust method based on the use of the particle signal itself has been developed during the Ph.D. research. The gain extracted by this new method may be used either in replacement to the (offline) tick-mark gain or as an extra gain applied in addition of the tick-mark gain in order to correct the residual mis-calibration of the latter. The second is the current default configuration.

The method consists of building, for each APV (or group of APVs), the distribution of the cluster charge normalized to the path-length of the particle in the silicon of the module. The latter can be fitted by a Landau distribution in order to extract the Most Probable Value (MPV) of the normalized charge distribution. The detector inter-calibration is based on the equalization of the MPV computed to an arbitrary value (300 ADC/mm). The value of 300 ADC/mm was chosen because it is close to the expected cluster charge created by a MIP.

$$G = \frac{300 \text{ (ADC/mm)}}{\text{MPV (ADC/mm)}}$$

Clusters associated to Minimum Ionizing Particles (MIPs) are used in order to build the charge distributions, and only distributions sufficiently populated ( $>50$  Entries) are fitted to extract the MPV. Therefore, inter-calibration constants can be calculated only for APV crossed by at least 50 MIPs. Clusters overlapping on two APVs are ignored as well as cluster close to the sensor edges. A statistic of  $\sim 1M$  minimum bias event is needed to calibrate  $> 99\%$  of the APVs.

This method, since it was completely new in the CMS framework, has been deeply studied on Monte Carlo simulated data. It was then used to calibrate the very first CMS data: cosmic data for two years and more recently collision data at 900 GeV and at 7 TeV. In many of the cases, the study was done with a silicon tracker operating in both deconvolution and peak mode. After a brief discussion of all the instrumental effects that may bias this inter-calibration procedure, the latest results, at 7 TeV with a tracker operating in deconvolution mode, will be detailed in the context of this dissertation. The reader may find results of this calibration procedure for older data taking (including cosmic data) in references [53, 54].

### Bias of the algorithm

The bias induced by subtle instrumental effects on the MPV measurement and therefore on the computed inter-calibration constants have been estimated using simulated data. Only the main conclusion of this study are presented here.

The first effect to consider is the increase of the (minimum bias) particle momentum with  $\eta$ : average momentum is about 2 GeV/c (3 GeV/c) at  $\eta = 0$  ( $\eta = 2$ ), resulting in an up to  $\sim 5\%$  increase in the MPV of the normalized cluster charge.

Another effect that has to be taken into account is the change of shape of the normalized cluster charge distribution with the particle path-length through silicon sensors, see Figure 3.7 (left). The distribution which is close to a Landau distribution tends to be more Gaussian when the path-length become larger, resulting in a shift of the MPV with the path-length. This can be understood by the smaller fluctuation on the number of  $\delta$ -ray escaping the sensor volume. The shift can be described by  $MPV \approx A + B \ln(x)$  [55], where  $x$  is the path-length of the particle in the silicon. The mean of the distribution is given by the Bethe-Bloch formula and does not depend on the path-length.

The strength of the two previous effects is dependent on the  $\eta$  position of the strip module. This dependence is shown on Figure 3.7 for the different strip tracker sub-detectors.

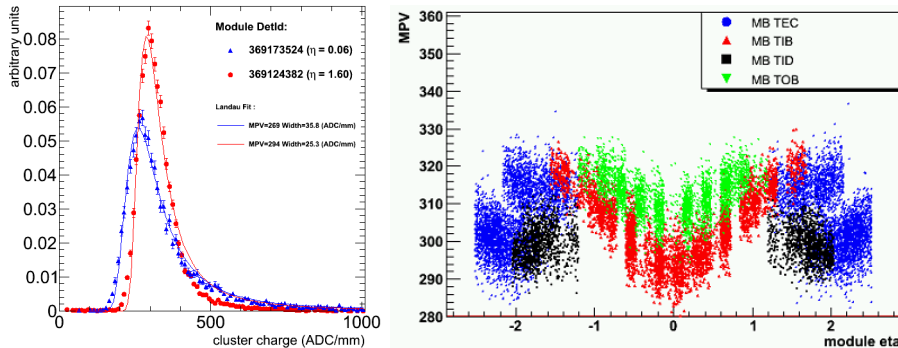


Figure 3.7: Left: Normalized cluster charge distributions and their Landau fits for two (TIB) modules. The red (blue) distribution is produced with mono-energetic muons having a mean path-length of 300 (600) $\mu$ m in the silicon sensor. Right: Distribution of the Most Probable Value (MPV) of the normalized cluster charge distribution of an APV as a function of the strip module  $\eta$  position and of the sub-detector. Using simulated mono-energetic (50 GeV) single muon events.

In the barrel (TIB,TOB), the MPV increases by about 10% between  $\eta = 0$  and  $\eta = 1.5$ , this is because of the increase of the track mean path-length in these modules. In the endcaps (TID, TEC), since the modules are perpendicular to the beam axis, see Figure 2.8, the mean path-length and thus the MPV decreases when eta increases. Two opposite effects are therefore contributing to the displacement of the MPV with

$\eta$ : the increase of the average momentum tends to increase the MPV, but on the other hand, the decrease of the mean path-length with  $\eta$  (for  $|\eta| > \sim 1.1$ ) tends to decrease the value of the MPV. The first effect is dominating. For TEC, two lines are visible because the two different sensor thicknesses of this subdetector are affected differently by the non-linearity of the MPV with the path-length.

The rise of the MPV with the path-length is almost impossible to be corrected due to other effects that modify this logarithmic dependency of the MPV with the path-length. Mainly three instrumental effects are responsible for the deformation of the rise.

The Zero Suppression applied by the FED may slightly affect the cluster shape in removing the first and last strips of the clusters and thus artificially lowering the cluster charge. This effect is rather small but plays a role.

The Capacitive Coupling is the effect that induced charge on the neighbor strips of the strip actually crossed by a particle. Up to 25% of the main strip charge can leak on the closest neighbor strips when the tracker is operating in deconvolution mode. In peak mode only few percents of the charge are spread (5%).

Finally the Saturation effect of the strip charge at 254 ADCs is appearing since the FEDs only keep and transmit (after common mode and pedestal subtraction) the height first Least Significant Bits (LSB) of the strip charge to the Data Acquisition system (DAQ). In order to keep information on the initial strip charge, the strip charge values of 254 and 255 ADC counts are used to code, respectively, that the strip had a charge in the range [254,511] ADCs or in the range [512, 1024] ADCs. This effect is very problematic for what concerns the physics of the heavy stable charged particles, because it biases the cluster charge and therefore complicates the particle identification using ionization energy loss, this will be discussed in detail in chapter 4. It also biases both the inter-calibration with particles algorithm and the study of the MPV-vs-path-length because clusters having a saturating strips can not obviously be used by this analysis.

Taken independently, these different effects are not dramatically biasing the data, but when combined they become much more significant. It is clear that the capacitive coupling can increase the bias induced by the zero suppression since it tends to induce leaks of the first and last cluster strip and thus reduce their absolute charge. On the other hand, the effect of the saturation is decreased by this capacitive coupling effects. For example, for path-length above 0.75mm, it is observed that the MPV is actually decreasing as a consequence of these three effects.

## 7 TeV collision data

At the end of March 2010, the strip tracker response was studied using real 7 TeV LHC collision data for the first time. The results of this study will be shown here. In order to ease the understanding, similar results for Monte-Carlo data with a simulated miscalibration, consisting in a 10% smearing of the APV response, are also given. Tracker was operating in deconvolution mode and inter-calibration algorithm was run at APV-granularity.

Only runs, in the range 132440 to 133325, where both the pixel and strip detectors were running, are used for this analysis. A simple event selection, based on L1 technical trigger bits 0, 36, 37, 38, 39 and 41, was applied in order to remove collision background events, it requires

- crossing bunches, those can be detected via the activation of the Beam Pick-up Timing Experiment (BPTX) detector that flags the presence of a proton bunches passing through CMS.
- the activation of at least two Beam Scintillator Counters (BSC) detector on each side of CMS, with a time correlation compatible with a collision at the middle of CMS.
- a BSC time measurement between the two sides of CMS incompatible with the passage of a particle from forward to backward region, typically a beam background event.

In addition of the run and event selection, a selection of the reconstructed track is also applied in order to use only high quality track of at least 8 hits. The track momentum must be higher than 2 GeV/c in order to fill the cluster charge distribution with only MIPs. Some requirements on the clusters are finally applied: no saturating<sup>1</sup> strip is allowed, cluster size must not be too large to avoid clusters affected by hard  $\delta$ -rays and the cluster can not be spanned on 2 APV chips. Clusters used are already calibrated with the tick-mark method, so the inter-calibration with particles comes as an extra calibration for the residual tracker miscalibration.  $\sim 6.7M$  events are passing the selection for this run range, giving up to  $\sim 187M$  of usable clusters.

The MPV is computed only if the APV normalized cluster charge distribution counts enough entries and the inter-calibration gain is extracted only if the Landau distribution fits properly the data, resulting on a small error on the MPV. Same procedure is used on the equivalent simulated data sample. The distribution of the MPV computed at APV level for the different tracker parts is shown on Figure 3.8.

---

<sup>1</sup>Strip charge must be lower than 254 ADC.

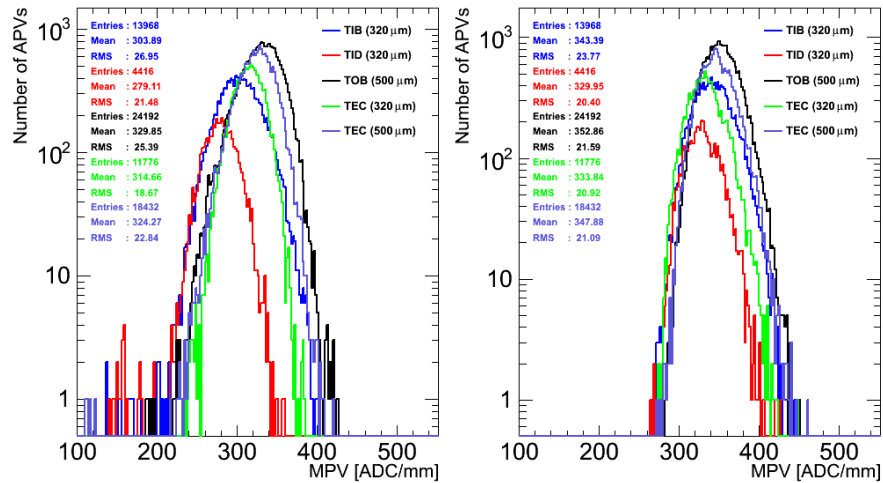


Figure 3.8: Distribution of the Most Probable Value (MPV) of the APV normalized charge distribution for the different tracker parts. Left: Distribution for data extracted from runs between 132440 and 133325. Right: Equivalent Monte-Carlo data with a simulated miscalibration obtained by a 10% smearing of the APV response.

These plots contain many information, first of all, several APVs have a small response (visible on the left of the data distribution), those are mainly TIB, TID and TOB modules that have been identified as modules for which the length of the optical link between the APV and the FED were wrong in the database. Therefore, sampling time adjusted via the PLL is not ideal for those modules: the result of a shift of  $\sim 5(10)$  ns in time with respect to the optimal synchronization implies a drop in the signal response of 19% (45%), see Figure 3.3.

Secondly, the R.M.S. of the distribution is similar for all the tracker parts but also between Monte-Carlo and Data, this indicates that the 10% miscalibration of the APV response was a reasonable assumption. The mean value of the same distributions are clearly changing with the subdetectors. Differences in mean are expected because of a  $\sim 5\%$  increase of the MPV due to a harder particle spectrum illuminating the modules in the forward region (TID and TEC), but also because of another  $\sim 5\%$  increase of the MPV with the path-length. Therefore, an increase of the mean MPV for thick modules (TOB and TEC thick) is expected. Modules having an important angle with the track, like the TOB modules at the end of the barrel (high eta), are also expected to have an higher MPV. The comparison of the mean values of the MPV distributions between Monte Carlo data and collision data allows to conclude that response of TIB/TID modules is too low with respect to the other tracker parts. Investigations to understand where this shift is coming from are ongoing by the CMS

Tracker operation group. The current hypothesis is that for these subdetectors, the reference tick-mark height was changed from 640 ADC counts to 700 ADC counts. A second hypothesis explains this feature by variations to the input voltage (LV) of these modules. Finally, an overall shift of the MPV between data and Monte-Carlo is observed, this indicates that simulation of the absolute particle ionization energy loss was overestimated.

The cluster charge distribution of the data before and after inter-calibration with gain is shown on Figure 3.9. After calibration, a reasonable agreement in the shape of the cluster charge distribution between data and simulation is observed. As expected, the MPV of the distribution is well centered on the value of 300  $ADC/mm$ .

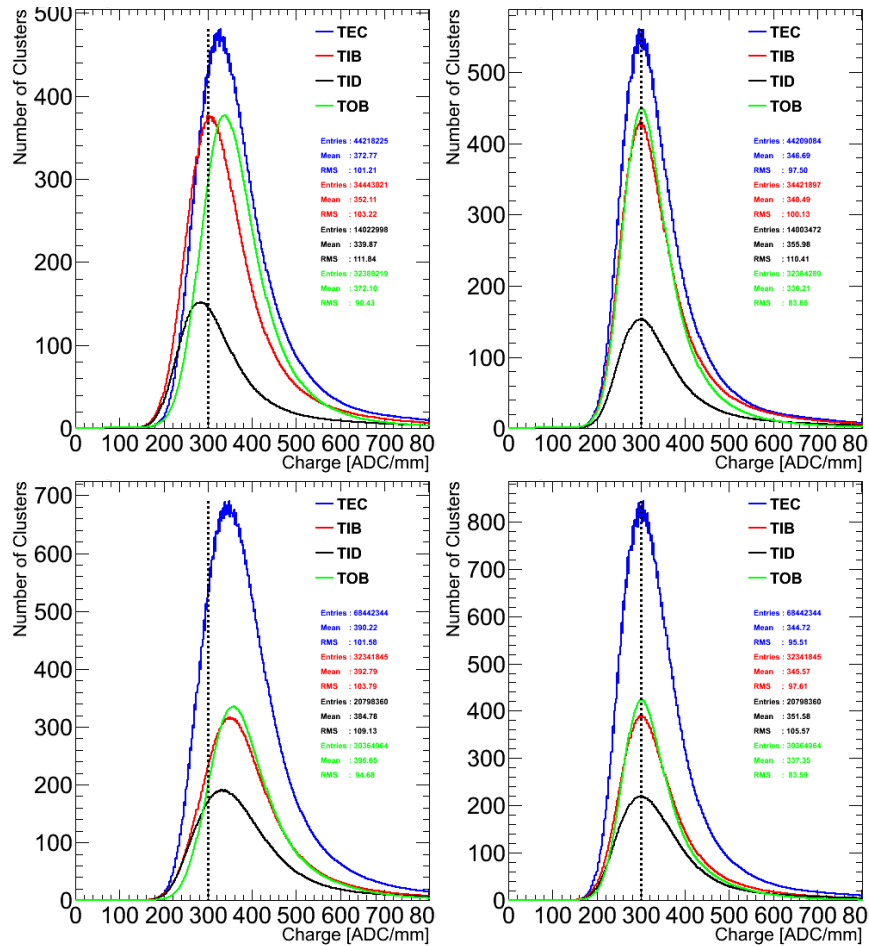


Figure 3.9: Distribution of the path-length normalized cluster charge at subdetector level before (left) and after (right) the inter-calibration of the silicon strip tracker with particle for real collision data (top) and for simulated data (bottom). The dashed line represents the inter-calibration value.

### 3.3 Absolute calibration of gain

In addition to the inter-calibration constants, a last calibration is needed in order to convert the measured particle energy loss in the silicon into a physical unit. Indeed, up to now, the cluster charge was measured in ADC counts. This electronic unit is not really meaningful for physics. What matters for physical purpose, like for particle identification using energy loss, is not the cluster charge in ADC counts, but the amount of energy released by a particle that crossed a given thickness of silicon material. A conversion factor from the ADC counts to a physical unit of energy is therefore needed. The number of ADC counts measured is directly proportional to the height of the electronic signal induced on the sensor strip, which is itself proportional to the number of electrons produced by the passage of an ionizing particle into the silicon sensor. Finally, the number of electrons produced is proportional to the energy lost by the ionizing particle. Since the amount of energy needed to create an electron-hole pair in a silicon at -10°C is known (3.61 eV), the energy loss by a particle in eV can be easily described in terms of ADC counts:

$$\Delta E \text{ (eV)} = \frac{\Delta E \text{ (ADC)}}{G} \times N_e/\text{ADC} \times 3.61 \text{ eV}$$

Where, G is the inter-calibration factor measured earlier and  $N_e/\text{ADC}$  is the number of electron-hole pairs created per ADC count. Therefore, the only unknown parameter that needs to be evaluated is the number of  $e^-$  created per ADC. Three different methods are used in this section to measure this parameter.

#### 3.3.1 Using APV charge injection

The APV chips provide an on-chip calibration circuit that may be used for the absolute calibration of the modules. This feature allows a charge injection of 60 000  $e^-$  with a precision of 5%. During CRAFT08, a calibration run gives a mean signal of 223 ADC counts with a R.M.S. of 29 ADC counts [51], see Figure 3.10. This gave a calibration factor of  $269 \pm 13 \text{ e}^-/\text{ADC}$  counts. The error results from the 5% precision on the charge injection.

The weaknesses of the technique are similar to the tick-mark weaknesses: only effects affecting the signal after the APV chip in the tracker readout chain can be probed, it is not sensitive to sampling time effects and the extracted information can not be combined easily with the inter-calibration constants.

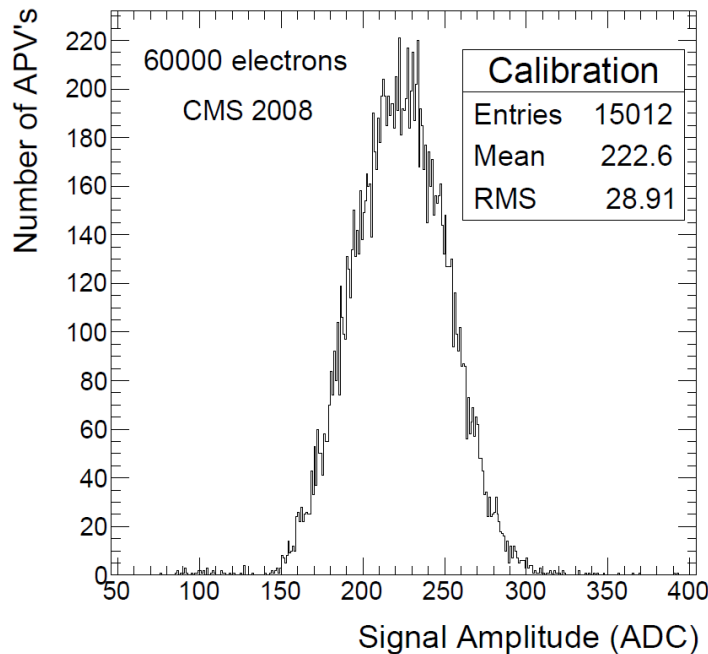


Figure 3.10: Pulse height measurements using the on-chip calibration circuitry of the APV chips in TEC+ [51].

### 3.3.2 Using the tick-mark height

The tick-mark amplitude, supposed to be 640 ADC counts, is a good indicator of the maximum output of the APV chip, which is expected to correspond to a charge deposit of  $175\,000 e^-$ . This method provides a calibration factor of  $274 \pm 14 e^-/\text{ADC counts}$ . The estimated systematic uncertainty is 5%, attributable to the sensitivity of the tick-mark amplitude to variations in the LV power supply and environmental temperature.

This measurement is compatible with the  $269 \pm 13 e^-/\text{ADC counts}$  obtained using the dedicated APV circuitry.

### 3.3.3 Using energy deposit

The energy loss by particles crossing thin layers of silicon is described by the Landau-Vavilov-Bichsel theory [56]. The most probable energy deposition per unit of length, MP  $\Delta E/\Delta x$ , is described by the Bichsel function and depends on the silicon thickness and both the particle momentum and mass.

For muons, the function has a minimum at a momentum of 0.5 GeV/c and then rises to reach a plateau for momenta greater than 10 GeV/c.

The absolute gain calibration can be determined by fitting the Bichsel function predictions to the measured MP  $\Delta E/\Delta x$  values from the CRAFT08 data sample. The quantity MP  $\Delta E/\Delta x$  is measured using the charge of clusters associated to tracks as a function of track momentum. The resulting charge distributions are fitted with a Landau convoluted with a Gaussian. Only tracks of good quality with at least 6 hits are considered. In addition, only clusters with a reasonable cluster size are taken into account to avoid clusters affected by hard  $\delta$ -ray but also to avoid mis-reconstructed clusters.

Before the absolute calibration factor can be extracted from the cluster charge data, two corrections must be applied. First, a correction is needed to take into account any charge loss due to the zero-suppression process or due to the clustering. This is determined using Monte Carlo simulations for each subsystem and for both thin and thick sensors in the end caps. Secondly, a correction is needed to handle the imperfect (PLL) synchronization between the different subsystems [51]. Overall, the uncertainty due to these corrections is estimated to be about 1.5%.

Figure 3.11 shows the most probable value of energy deposition per unit length plotted as a function of the track momentum for both thin and thick sensors. The error bars reflect the uncertainty from the Landau fit, while the bands represent the fully-correlated systematic uncertainties from Monte Carlo corrections. The small dip at 5 GeV/c arises from a temporary problem in the trigger provided by a sector of the muon chambers, because of which this momentum region was contaminated with out-of-time particles. The absolute calibration factor is determined separately for each subsystem and for both thin and thick sensors in TEC+ and TEC-.

The resulting values are given in Table 3.2. If a fit is performed for all SST modules together, the absolute calibration factor is found to be  $262 \pm 3 e^-/\text{ADC counts}$ , which is very similar to the result in the TOB alone since it dominates the data sample. However, thick and thin modules are compatible and overall the result is in agreement with the value of  $269 \pm 13 e^-/\text{ADC counts}$  obtained using the dedicated APV circuitry. The uncertainty of  $3e^-/\text{ADC counts}$  is mostly coming from the uncertainty on the system synchronization.

The rise of the energy deposit becomes almost negligible for (MIPs) particles with a momentum above  $\sim 20$  GeV/c, as also shown by the Figure 3.11. Below this threshold value, the energy loss still depends on the particle momentum. This is an important feature that needs to be correctly taken into account for the MIP backgrounds of the search for HSCP.

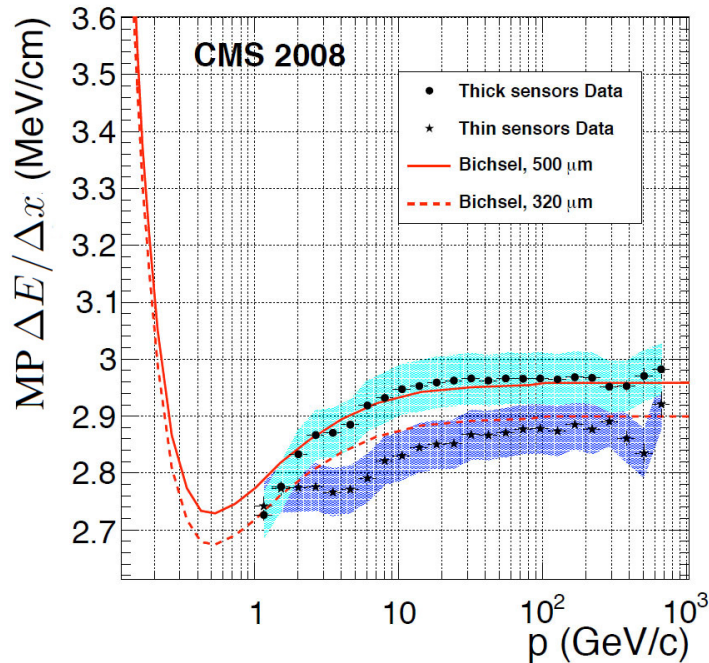


Figure 3.11: Most probable energy deposit per unit of length  $\Delta E/\Delta x$  as a function of track momentum, for thin and thick sensors. The shaded bands show the correlated systematic uncertainties on the measurements, evaluating using both the simulation and the data. The curves are the expectations from the Bichsel function [56, 51].

Subsystem	$e^-/\text{ADC counts}$
TIB/TID	$262.3^{+2.5}_{-3.5}$
TOB	$261.5^{+0.5}_{-1.5}$
TEC+ 320 $\mu\text{m}$	$273^{+7}_{-9}$
TEC+ 500 $\mu\text{m}$	$270^{+7}_{-9}$
TEC- 320 $\mu\text{m}$	$264^{+3}_{-4}$
TEC- 500 $\mu\text{m}$	$261^{+3}_{-4}$

Table 3.2: Measured absolute charge calibration in the different tracker subdetectors using cosmic particles from the CRAFT08 run.

## 3.4 Conclusion

Innovative silicon strip tracker calibration method using particles has been developed and deeply studied. The use of cosmic or collision particles for the calibration allows to correct for many effects affecting the silicon strip read-out chain. Many of these effects, like inefficiency due to voltage bias or simply radiation damages of the silicon, can not be corrected by the standard calibration method based on an electronic signal pulse. The developed method allows to measure the absolute charge calibration with a resolution at the percent level.

The limited ( $\sim 10\%$ ) resolution of the developed inter-calibration method is mainly due to electronic effects affecting the measurement: Zero Suppression, Capacitive Coupling and Strip Saturation at 253 ADC Counts. This resolution is sufficient for particle identification based on ionization energy loss ( $dE/dx$ ) given the intrinsic large fluctuation on individual  $dE/dx$  measurements, see chapter 4.

By construction of the inter-calibration, the most probable energy loss released by a minimum ionizing particle (MIP) is 300 ADC/mm. Since the conversion factor between the ADC and the eV is also known, some useful cross-checks can be done. With these calibrations, the energy released by a MIP is :

$$300 \text{ (ADC/mm)} \times 262 \text{ (e}^-/\text{ADC)} \times 3.61 \text{ (eV/e}^-) = 2.8 \text{ (MeV/cm)}$$

This measurement is compatible with the expected value found in the literature [55] and justifies the inter-calibration reference value. The same relation can be used to determine where the saturation effect appears in terms of energy loss:

$$254 \text{ (ADC)} \times 262 \text{ (e}^-/\text{ADC)} \times 3.61 \text{ (eV/e}^-) = 0.24 \text{ (MeV)}$$

Silicon sensors of 500 (320)  $\mu\text{m}$  have an effective silicon thickness of 470 (290)  $\mu\text{m}$ , this imply that an energy loss of 4.9 (7.6) MeV/cm, equivalent to 1.8 (2.9) the energy of a MIP, is already saturating. The previous computations assumed that the cluster charge is concentrated on a single strip, this is in general not true. In average, the clusters are made of  $\sim 4$  strips, but it can be even more when the particle trajectory is significantly bended by the magnetic field. In the next chapter, chapter 4, many  $\Delta E/\Delta x$  measurements are combined to allow particle identification.



# Chapter 4

## Particle identification and mass reconstruction with $dE/dx$

This chapter will focus on particle identification techniques based on the particle ionization energy loss measured by the CMS Silicon Strip Tracker. Main algorithms and techniques will be detailed, and their performances for particle identification are reported using data collected with the CMS detector during LHC commissioning in April 2010 at a center-of-mass energy of 7 TeV.

Techniques developed and validated with low momenta hadrons in this chapter can be easily transposed to the search for Heavy Stable Charged Particles, since these two types of particles behave similarly for what concern the ionization energy loss.

### 4.1 Introduction

The mean ionization energy loss of a particle crossing a layer of material is given by the Bethe-Bloch formula [55]:

$$\left\langle \frac{dE}{dx} \right\rangle = kz^2 \frac{Z}{A} \frac{1}{\beta^2} \left[ \frac{1}{2} \ln \frac{2m_e c^2 \beta^2 \gamma^2 T_{\max}}{I^2} - \beta^2 - \frac{\delta(\beta\gamma)}{2} \right] \quad (4.1)$$

where  $Z$  and  $A$  are the atomic number and mass number of the absorber respectively,  $I$  is the average excitation potential of the absorber atoms, its value is  $173 \pm 3$  eV for silicon.  $\beta$ ,  $\gamma$  and  $z$  are respectively the velocity, the Lorentz factor and the electric charge of the incoming particle.  $\delta(\beta\gamma)$  is a density correction to the ionization energy

loss that is small under normal conditions.  $k$  is a constant of value  $0.31 \text{ A}$  in unit of  $\text{MeV g}^{-1} \text{ cm}^2$ . Finally,  $T_{max}$  is the maximum kinetic energy which can be imparted to a free electron in a single collision.

The Bethe-Bloch formula describes the mean rate of energy loss in the region  $0.1 \leq \beta\gamma \leq 1000$  for intermediate-Z materials with an accuracy of a few percents. The mean ionization energy loss is shown on Figure 4.1 for different materials and incident particles. For particles with high momentum crossing a thin ( $\lesssim 500 \mu\text{m}$ ) layer of material, the Landau-Vavilov-Bichsel function [56] is a better parameterization of the ionization energy loss than the Bethe-Bloch formula, see section 3.3.3. For un-relativistic particles, the two parameterizations are almost identical.

The mean energy loss is a quantity that can be used for particle identification since, for a given absorber and momentum, it is completely determined by the velocity of the incoming particle and therefore by its mass. The particle identification is possible in the region where large differences in the mean energy loss are observed for small variations in the momentum of the incident particle:  $0.2 \leq \beta\gamma \leq 0.9$ . For higher values of  $\beta\gamma$ , the Bethe-Bloch function reaches a plateau where discrimination between particles is almost impossible. At CMS, these constraints allow identification of low momenta hadrons (pions, kaons and protons), but also of Heavy Stable Charged Particles (HSCPs) that are generally also un-relativistic particles given their high mass.

In this restricted region, the formula 4.1 can be linearized in  $m^2/p^2$  with a few percents agreement with respect to the complete parameterization [57], see Appendix B:

$$\left\langle \frac{dE}{dx} \right\rangle = K \frac{m^2}{p^2} + C \quad (4.2)$$

The main difficulty of the particle identification comes from the few measurements available to estimate the mean particle energy loss. A particle produced by a  $pp$  collision in CMS crosses in average 20 silicon modules before reaching the calorimeters. Each crossing point is a measurement of the particle specific ionization energy loss per unit of path-length ( $\Delta E/\Delta x$ ). The mean ionization energy loss must be estimated out of the few measurements associated to the track. By nature of the particle energy loss fluctuation in thin layer of material, ruled by the Landau distribution, each  $\Delta E/\Delta x$  is strongly fluctuating and therefore the mean energy loss is generally not reliable enough to be used for particle identification. The most probable energy loss ( $dE/dx$ ) is used instead of the mean because it is more stable than the mean.

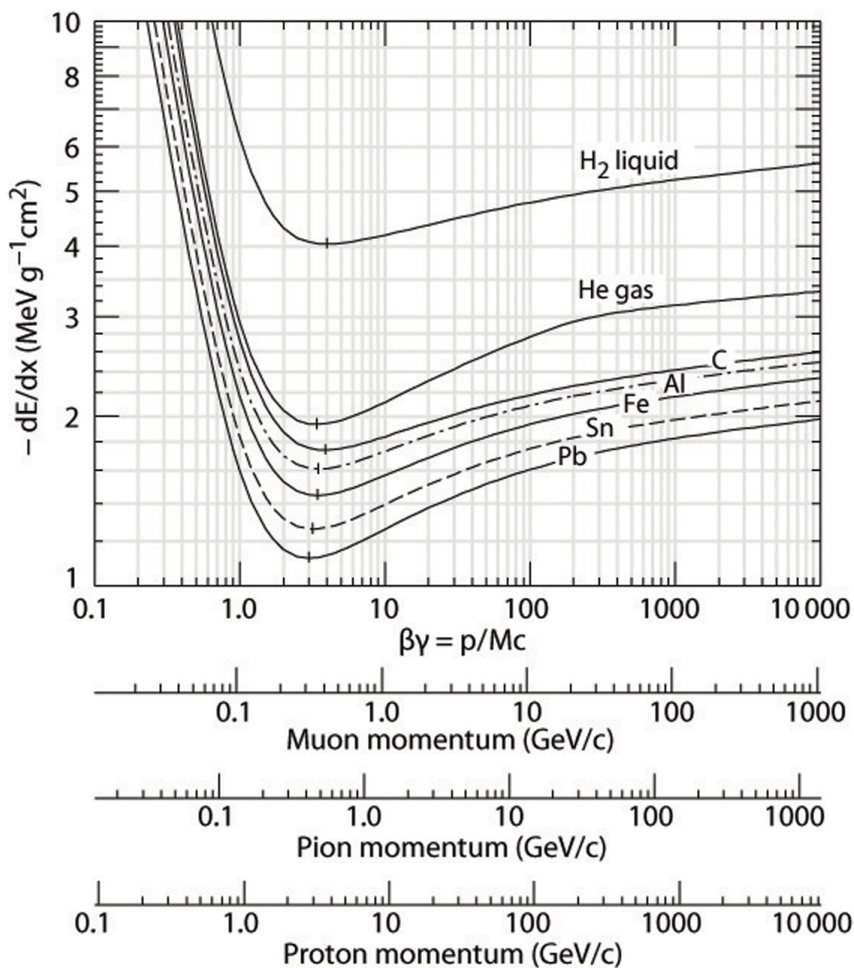


Figure 4.1: Mean energy loss rate in liquid (bubble chamber) hydrogen, gaseous helium, carbon, aluminum, iron, tin and lead. Radiative effects, relevant for muons and pions with  $\beta\gamma \geq 1000$ , are not included [55].

## 4.2 $dE/dx$ estimators

The main purpose of the MP  $dE/dx$  estimators is to combine the few  $\Delta E/\Delta x$  measurements distributed along the particle trajectory into one unique value of the estimated most probable energy loss associated to the track. The short-hand notation MP  $dE/dx$  is used for the estimation of the most probable energy loss, it is also frequently just noted as  $dE/dx$  by abuse of terminology. The combination of the measurements is used to get rid of the large fluctuation of the individual  $\Delta E/\Delta x$  measurements. A couple of estimators have been implemented in the context of this work, their definition is given below for a track leading to  $N$   $\Delta E/\Delta x$  measurements. The measurements are ordered by increasing value:  $(\Delta E/\Delta x)_i$  is the  $i$ -th measurement.

- The *Median estimator* is the median of the measurements set:

$$I_m^h = (\Delta E/\Delta x)_m \quad \text{where } m = N/2 \quad (4.3)$$

- The *Truncated-40 estimator* is the mean excluding the 40% higher values:

$$I_t^h = \frac{1}{T} \sum_{i=1}^T (\Delta E/\Delta x)_i \quad \text{where } T = 0.6 N \quad (4.4)$$

- The *Harmonic-2 estimator* is the harmonic mean of power  $-2$ :

$$I_h^h = \left( \frac{1}{N} \sum_{i=1}^N (\Delta E/\Delta x)_i^k \right)^{1/k} \quad \text{where } k = -2 \quad (4.5)$$

The median estimator is frequently used in other experiments, it is analytically simple but, unfortunately, it is very easily biased, in particular when the number of measurements is low. For this reason, it will not be used in the rest of this document. The truncated-40 estimator is more robust. By construction, it is hardly biased toward higher charge when a reasonable ( $\sim 10$ ) number of measurements is available, the disadvantage of the truncated-40 is obviously that 40% of the measurements are simply ignored. Finally, the harmonic-2 has the advantage of considering all the measurements without being easily biased toward higher charge. With this estimator, measurements are weighted by a negative power ( $-2$ ), therefore, measurements with an anomalously high charge are suppressed by their small weights in comparison to measurements with a smaller charge and thus a larger weight. The side effect of this weighting is that this estimator is very easily biased toward lower charge. In conclusion, there are no perfect estimators working for all use cases. When the number of measurements is reasonable and a small bias toward higher charge is acceptable, which is generally the case for the identification of low momenta hadrons, the

truncated-40 estimator is a good compromise. For the search for HSCP, the preferred estimator is the harmonic-2 because it has a stronger discrimination power since it is less biased toward higher charge.

Both the Silicon Strip sensors and the Silicon Pixel sensors can be used to get  $(\Delta E/\Delta x)$  measurements. However, combining Strip and Pixel measurements requires the good knowledge of the absolute charge calibration for both the pixel and strip detectors. Some techniques to extract this absolute charge calibration have been detailed in the previous chapter for the strip sensors, similar techniques must be developed for the pixel sensors in order to combine measurements from the two subdetectors.

This exercise has not been done in the context of the doctoral work for two reasons: First, the electronic cut-off of the pixel sensors (similar to the saturation effect described for the strips) is already happening for particles releasing 1.5 times more energy than a MIP, while this saturation effect appears only at 2.9 (1.8) times the energy of a MIP for strip sensors of  $320$  ( $500$ )  $\mu m$ . Therefore, it is not guaranteed that the pixel layers will significantly improve the estimation of the MP  $dE/dx$  for HSCPs where important energy loss is expected. Secondly, the pixel detector is composed by only 3 layers thus the pixel can only add for  $\sim 3$   $(\Delta E/\Delta x)$  extra measurements, which is likely negligible to the  $\sim 20$  measurements extracted from the strip sensor. So, in this document, the  $dE/dx$  estimators are assumed to be estimation of the MP  $dE/dx$  of a track computed with the silicon strip sensors only.

The Figure 4.2 shows the one dimensional distributions of the MP  $dE/dx$  estimators for minimum ionizing particles ( $p>5$  GeV/c) from real pp collision event, the distributions are shown for a tick-mark calibrated and a particle calibrated detector. This second calibration clearly improves the shape of the distribution. The large tail at lower charge for the harmonic-2 estimator appears because of the bias toward lower charge discuss before.

The Figure 4.3 shows a comparison of the MP  $dE/dx$  estimators distribution between the data and the simulation for a detector calibrated with particles (bottom) or not (top). In the two cases, the data are already calibrated by tick-marks, so the gain with particles only corrects for residual (still important) miscalibration. Simulated data are one time uncalibrated and a second time calibrated with particles. A clear overall shift between data and simulation is observed, it comes from a not perfectly well simulated response of the SST detector. This shift is also corrected by the gain with particle, since the response of the detector, both in the data and in the simulation, is aligned to the value of  $300$  ADC/mm. Thanks to this, a good agreement between data and simulation is found once detectors are particle-calibrated. Despite this overall shift, it is also visible that the distribution of the MP  $dE/dx$  estimators is higher and therefore thinner after the particle calibration. In the following, all the distributions are extracted from a detector calibrated with particles on both data and simulation.

The correlation of  $dE/dx$  of a track with its momentum is shown on Figure 4.4 for the different estimators for simulated events (top) and for data events (bottom). As expected, the Bethe-Bloch rise for particle with  $\beta\gamma = \sim 0.5$  is well visible and allows to distinguish between, from lower to higher momentum, kaons, protons and deuterons ( $p+n$  nuclei). The pion rise is suppressed by the track quality requirements: "high purity" track with at least 12 SST hits and compatible with the vertex ( $|dZ| < 0.1\text{cm}$  and  $|dxy| < 0.025\text{cm}$ ). Low-momentum kaons and protons are neatly separated from pions with reconstructed masses in agreement with the known values. The absence of deuterons is observed in the simulation since this particle is not simulated by the PYTHIA generator [58]. When vertex compatibility requirement is relaxed, deuterons produced by the interaction of primary particle with the material of the detector are observed. But a lower number of secondary deuteron observed in the simulation may indicate that GEANT4 is also underestimating the production of these particles.

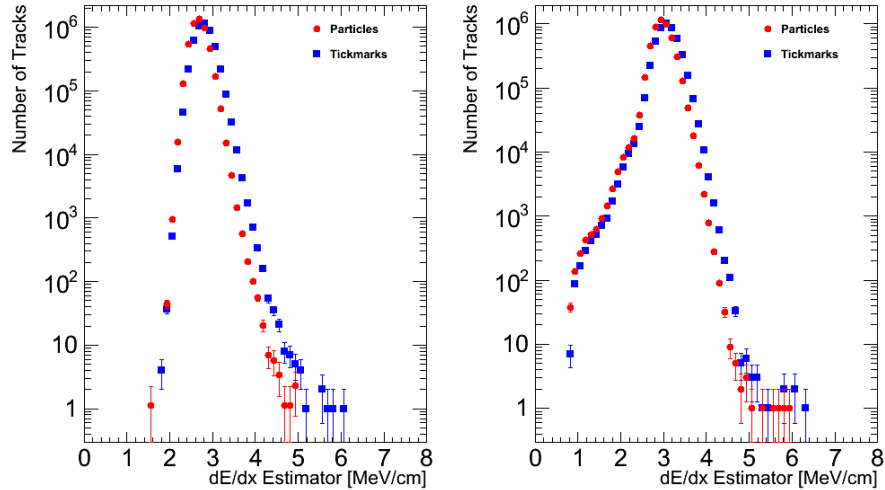


Figure 4.2: Distribution of the MP  $dE/dx$  estimators for tick-mark calibrated data and for particle calibrated data. In both cases, the same tracks have been used: good quality tracks of high momentum ( $p > 5\text{ GeV}/c$ ) coming from 7 TeV collision events. The truncated-40 (harmonic-2 estimator was used on the left (right).

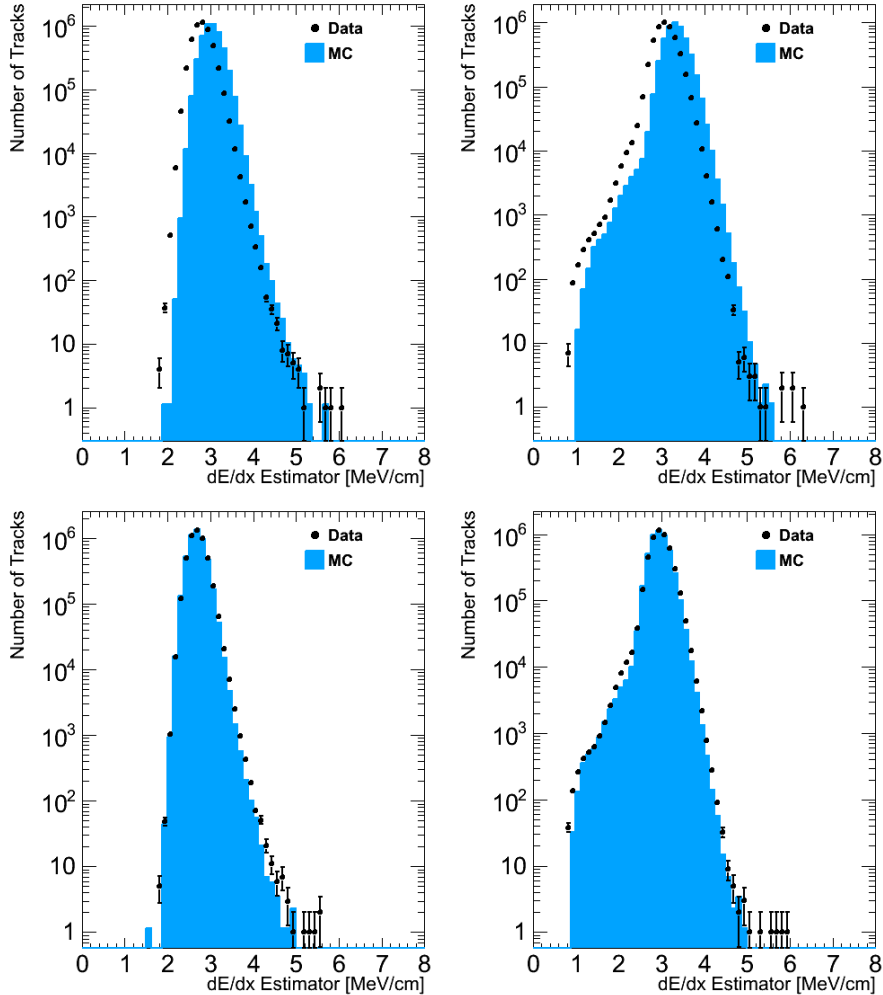


Figure 4.3: Distribution of the MP  $dE/dx$  estimators for good quality tracks of high momentum ( $p > 5$  GeV/c) coming from 7 TeV collision events. The first raw shows a tick-mark calibrated data against uncalibrated simulated data, while in the bottom row, the calibration with particle is used for both data and Monte-Carlo. Left (Right) distributions are built with the truncated-40 (harmonic-2) estimator.

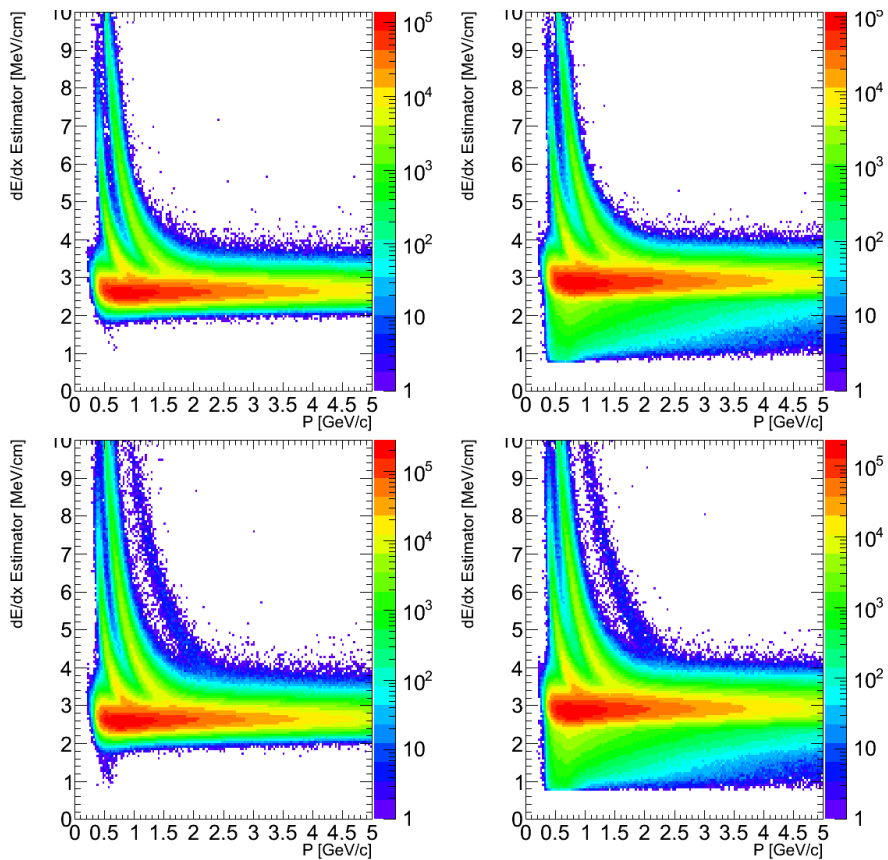


Figure 4.4: Distribution of the MP  $dE/dx$  estimators versus the track momentum for good quality tracks coming from simulated (top) and real (bottom) 7 TeV collision events. Truncated-40 (Harmonic-2) estimator is used on the left (right).

## 4.3 Mass Reconstruction

The simple parameterization of the Bethe-Bloch formula in  $0.2 \leq \beta \leq 0.9$ , see equation (4.2), can be used in order to reconstruct the particle mass from its momentum and MP  $dE/dx$ . The constants  $K$  and  $C$  of this parameterization are extracted from the data using protons.

In a first step, the proton MP  $dE/dx$  for different regions of momentum is estimated from a triple Gaussian fit on the  $dE/dx$  distribution for all particles in a thin window of momentum, see left of Figure 4.5 for the slice  $0.96 \text{ GeV}/c < p < 1.00 \text{ GeV}/c$ . The main reason why protons are used for this exercise is that proton peak is easily identifiable while the kaon peak is closer to the MIPs peak and therefore much harder to identify.

Then the constants are evaluated from a fit of the proton MP  $dE/dx$ , extracted at the previous step, as a function of the track momentum using the Bethe-Bloch parameterization assuming the mass of the proton, see right of Figure 4.5. This fit is done in a restricted range of particle momentum:  $[0.6, 1.0] \text{ GeV}/c$ . For softer tracks, the ionization may start to be too strongly affected by the saturation effects and therefore may bias the fit. For harder tracks, the identification of the proton mean MP  $dE/dx$  is difficult because of frequent failure of the triple Gaussian fit. These failures are visible on Figure 4.5 (right) in the region  $p \sim 1.5 \text{ GeV}/c$ , they come from the small separation between MP  $dE/dx$  of protons and kaons or MIPs at higher energies.

Once the constants have been extracted, the mass of any slow particle can be computed: Figure 4.6 shows the mass distribution for tracks with  $p < 2 \text{ GeV}/c$  and  $dE/dx > 5.0 \text{ MeV}/\text{cm}$  satisfying the quality criteria described earlier. By construction, the proton peak is reconstructed at its nominal value because constants evaluation is done using protons. The small observable bias between the reconstructed kaon/deuteron mass peak and the real mass value of these particles is mostly due to the effect of the electronic cut-off at 253 ADC. The bias is expected to be more important for heavier particles like HSCPs, because contrary to the low momenta hadrons, HSCPs are straight tracks that therefore rely all their energy loss on 1-2 strips at maximum. The threshold of 253 ADC is thus reached more frequently and the bias of the measured energy loss is larger.

The extracted constants can be validated as well as the simplified parameterization of the Bethe-Bloch by superimposing the expected mass lines for kaon, proton and deuteron particles on the MP  $dE/dx$  vs  $p$  distribution. The result of this exercise is shown on the Figure 4.7. Overall agreement is reasonable.

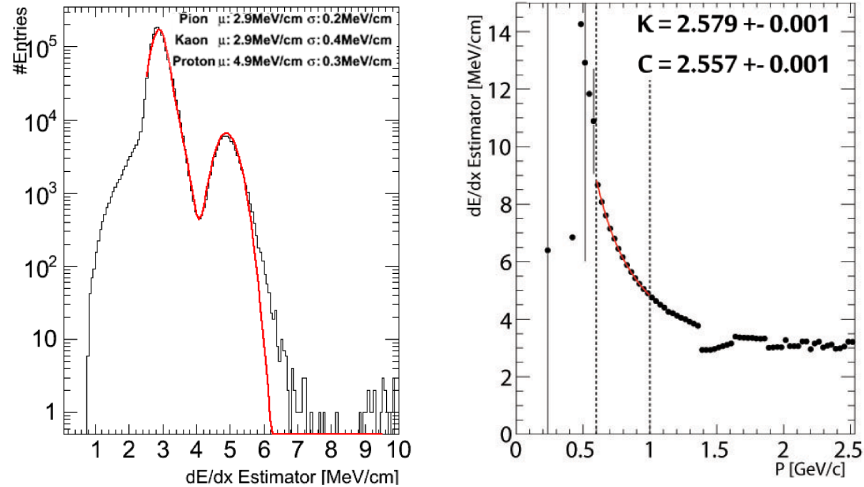


Figure 4.5: Left: Distribution of the  $dE/dx$  harmonic-2 estimator for good tracks with  $0.96 \text{ GeV}/c < p < 1.00 \text{ GeV}/c$ . A triple Gaussian fit is superimposed on the figure as well as the mean and the sigma of the three Gaussian. Right:  $dE/dx$  as a function of proton momentum

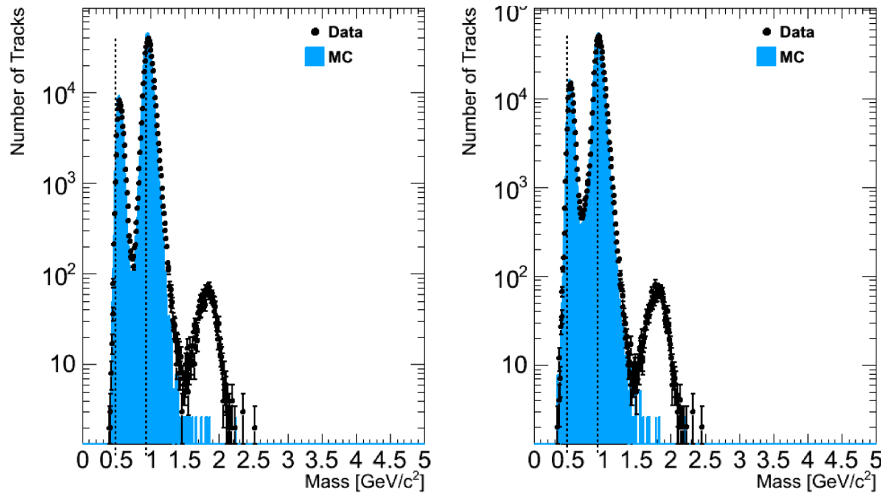


Figure 4.6: Reconstructed mass of low momenta hadrons with  $p < 2 \text{ GeV}/c$  and  $dE/dx > 5.0 \text{ MeV}/\text{cm}$  for the truncated-40 (left) and harmonic-2 (right) estimator. The three peaks corresponding, from lower to higher masses, to the kaon, proton and deuteron mass peaks. The absence of deuteron in the simulation is clearly highlighted here.

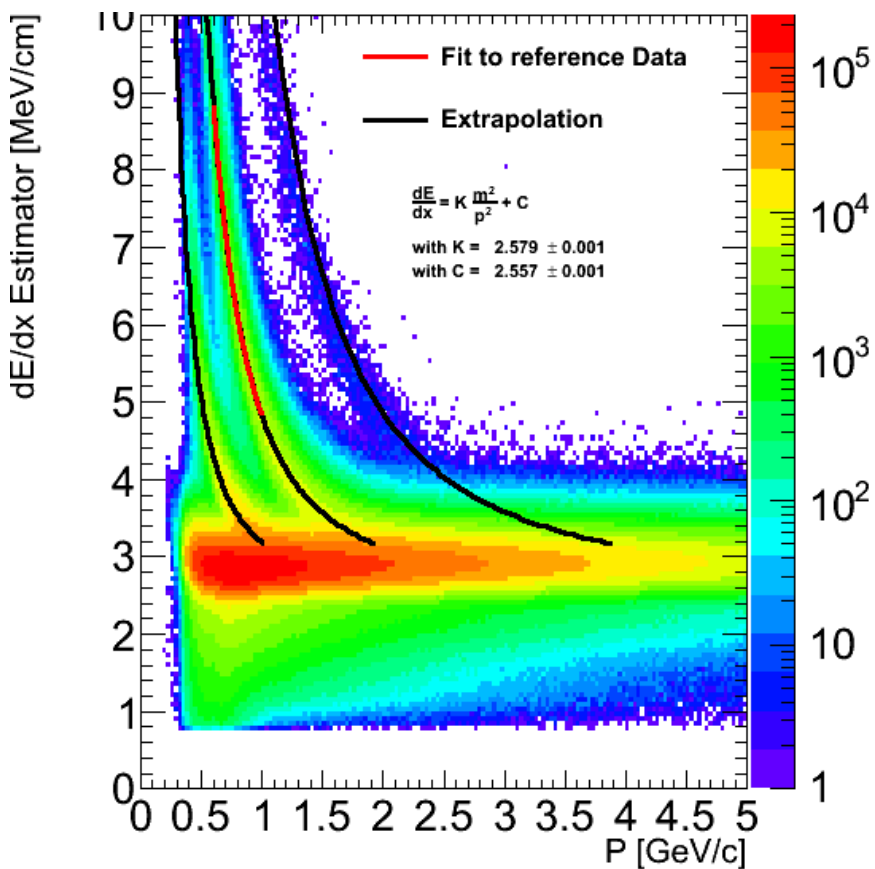


Figure 4.7: Distribution of the MP  $dE/dx$  harmonic-2 estimator against particle momentum. Mass lines using the simplified Bethe-Bloch parameterization are superimposed to the figure for the kaon, proton and deuteron particles.

## 4.4 $dE/dx$ discriminators

A better particle identification is expected to be obtained with a likelihood technique, where an estimation of the degree of compatibility of the observed charge measurements with a MIP is used. A couple of "discriminators" have been developed for a few relevant applications. Their advantages over the classical  $dE/dx$  estimators are that they make maximal use of all the available information and they are sensitive to the residual non-linear dependency of the ionization energy loss with the particle path-length in the silicon. In this respect, the CMS inner tracker has indeed detectors of different thicknesses, that are also traversed at different angles depending on the track  $\eta$ . It also includes the bias due to the strip charge cut-off at 253 ADC.

Contrary to the estimators that are computed out of a set of  $(\Delta E/\Delta x)$  measurements, the discriminators are built out of a set of probability  $P_h$  ordered by increasing values, where  $P_h$  is the probability that a MIP would release a normalized charge equal or smaller than the observed  $(\Delta E/\Delta x)$  measurement.

- The *Product discriminator* is the geometric mean:

$$I_p^d = \left( \prod_{h=1}^N P_h \right)^{\frac{1}{N}} \quad (4.6)$$

- The *Smirnov discriminator* is given by:

$$I_s^d = \frac{3}{N} \times \left( \frac{1}{12N} + \sum_{h=1}^N \left[ P_h - \frac{2h-1}{2N} \right]^2 \right) \quad (4.7)$$

- The *Asymmetric Smirnov discriminator* is given by:

$$I_{as}^d = \frac{3}{N} \times \left( \frac{1}{12N} + \sum_{h=1}^N \left[ P_h \times \left( P_h - \frac{2h-1}{2N} \right)^2 \right] \right) \quad (4.8)$$

By definition, these discriminators are built from probabilities which have therefore their values comprised between 0 and 1. The product discriminator ( $I_p^d$ ) is the most simple likelihood estimator that can be imagined.  $I_p^d$  values close to 1 indicate high incompatibility with the MIP hypothesis due to too high ionization energy loss. While values close to 0 also indicate incompatibility with a MIP, but because of too little ionization. Therefore,  $\Delta E/\Delta x$  measurements compatible with MIP energy loss have a product discriminator close to 0.5.

The Smirnov-Cramer-von Mises ( $I_s^d$ ) discriminator [59, 60, 61] is more complicated. Similarly to the well-known Kolmogorov test, it basically measures the distance between an empirical and an observed distribution function. In other words, it measures the compatibility between a set of  $\Delta E/\Delta x$  measurements and the MIP probability density function they are assumed to be coming from. If the measurement are indeed compatible with the MIP hypothesis, the  $I_s^d$  is close to 0. In the other case, the  $I_s^d$  will be close to 1. The main difference with respect to the Kolmogorov test comes from the distance definition which is the integral of square differences for the Smirnov-Cramer-von Mises test and is the supremum of the absolute difference for the Kolmogorov test.  $I_s^d$  values close to 0 (1) only indicate high compatibility (incompatibility) with the MIP hypothesis, without any information on whether there was too little or too much ionization.

The Asymmetric Smirnov-Cramer-von Mises ( $I_{as}^d$ ) discriminator is a custom modification of the  $I_s^d$  discriminator, in order to be only sensitive to incompatibility with the MIP hypothesis toward the higher charge side. Therefore values close to 1 of  $I_{as}^d$  are related to ionization in excess with respect to the MIP typical energy loss and ionization in defect is indistinguishable from the MIP hypothesis since it also has an  $I_{as}^d$  close to 0.

In order to use these discriminators, template probability density functions (pdf) for the charge released by MIPs for fixed path-length values must be computed from a reliable control sample; 28 different pdf distributions, each corresponding to a bin in path-length of width 50  $\mu\text{m}$  ranging from 0.2 to 1.6 mm are obtained from tracks having sufficiently high  $p$  ( $p > 5 \text{ GeV}/c$ ) to behave as MIPs, see Figure 4.8.

The Figure 4.9 shows the one dimensional distribution of the  $dE/dx$  discriminator for minimum ionizing particles ( $p > 5 \text{ GeV}/c$ ); a reasonable agreement between data and simulation is observed. The correlation of  $dE/dx$  discriminator of a track with its momentum is shown on Figure 4.10 for the different discriminators for data (bottom) and simulation (top). Identification of low momenta hadrons is again well visible.

Once again, it is difficult to state which is the best discriminator. The three have shown comparable performances for low momenta hadrons identification. The  $I_{as}^d$  discriminator is clearly preferred for the HSCP search since by construction it is only sensitive to incompatibilities toward higher charge.

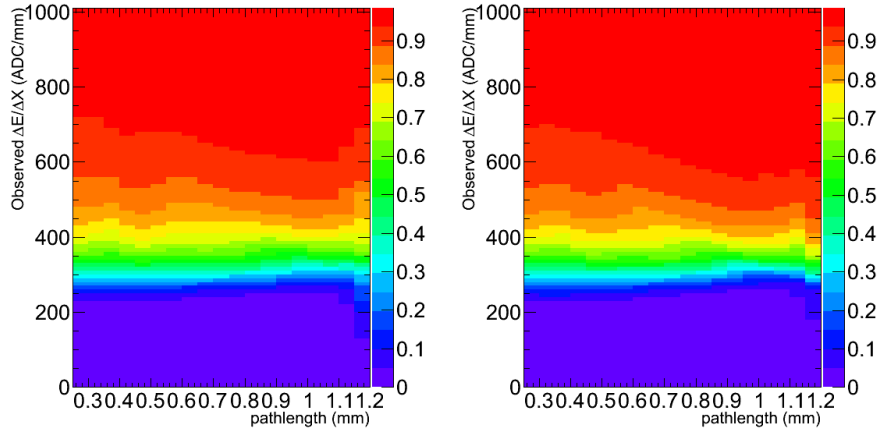


Figure 4.8: Templates used by the  $dE/dx$  discriminators, shows the probability that a MIP would release as much or less energy than what has been observed (on the x-axis) as a function of the particle path-length through the silicon sensor. Left template is for real data and right is for simulated data.

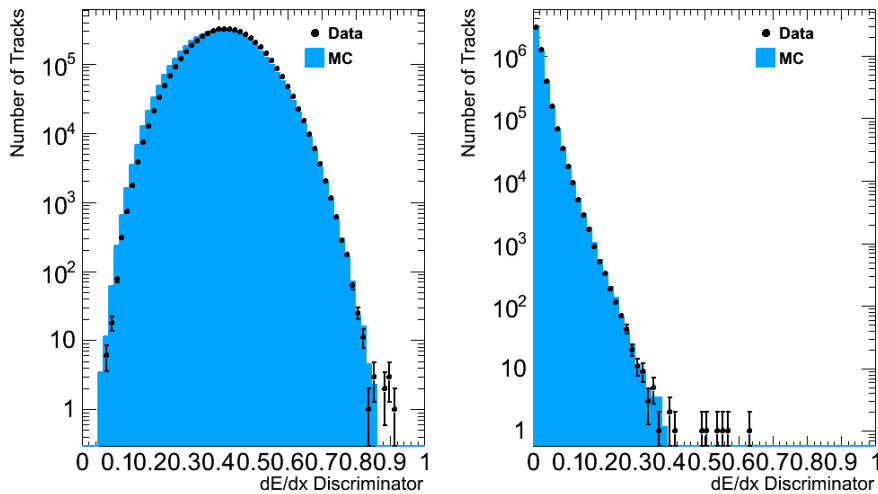


Figure 4.9: Distribution of the  $dE/dx$  discriminator for good quality tracks of high momentum ( $p > 5$  GeV/c) coming from 7 TeV collision events. Calibration with particle is used. Left distribution is built with the product discriminator, while the right is for the asymmetric Smirnov discriminator.

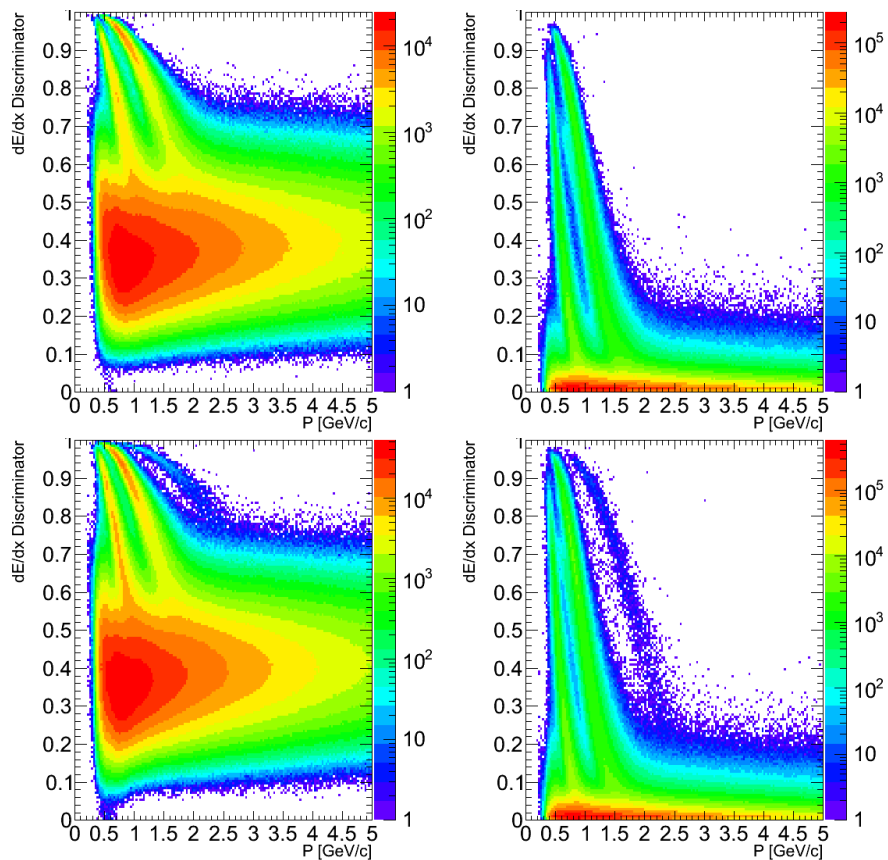


Figure 4.10: Distribution of the  $dE/dx$  discriminator versus the track momentum for good quality tracks coming from simulated (top) and real (bottom) 7 TeV collision events. Product discriminator is used on the left and Asymmetric Smirnov discriminator on the right.

By construction, the discriminators are more powerful for particle identification. The  $I_h^h$  estimator has been compared to the  $I_{as}^d$  discriminator for the HSCP identification, see Figure 4.11. The  $I_{as}^d$  discriminator will be used for the HSCP search since it is clearly more powerful than the estimator when a background selection efficiency of about  $10^{-3} - 10^{-4}$  is used, which is the typical background rejection needed for the HSCP analysis.

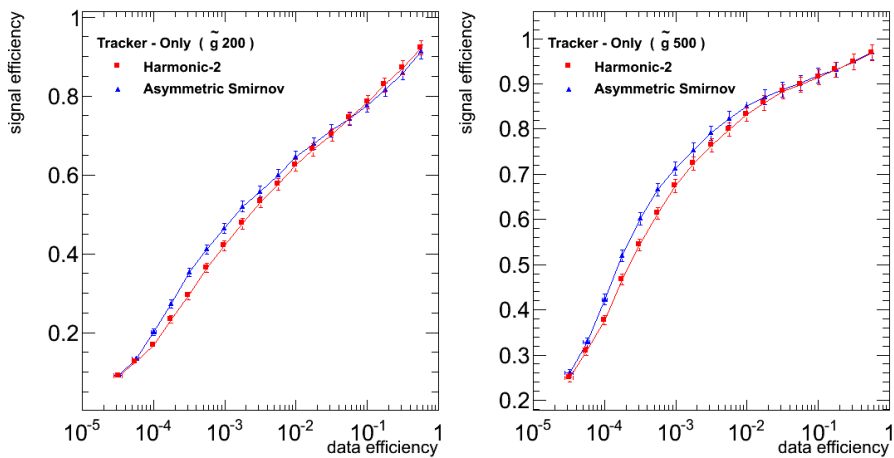


Figure 4.11: Signal and background selection efficiency for a selection only based on a cut on the  $I_h^h$  estimator or on the  $I_{as}^d$  discriminator of high quality tracks with a transverse momentum of 15 GeV/c. The signals used are 200 (left) and 500  $\text{GeV}/c^2 \tilde{g}$  (right). The background are real 7 TeV LHC data.

## 4.5 Validation of the particle identification tools

A validation of the  $dE/dx$  estimators and discriminators based on data collected with the CMS detector during LHC commissioning in December 2009 at a center-of-mass energy of 900 GeV is presented in this section [58].

The pure proton sample exploited in this validation is built from  $V^0$  decay, in particular from the  $\Lambda$  to  $p\pi$  decay. Protons resulting from the decay of a  $\Lambda$  can easily be identified, since the proton is always the hardest track when  $p_\Lambda > 300$  MeV [57]. Standard CMS  $V^0$  reconstruction algorithm is used to identify the  $\Lambda$  decays. In this algorithm, the proton is assumed to be always the hardest track, since reconstruction efficiency of  $\Lambda$  decay with  $p_\Lambda < 300$  MeV is almost null. The Figure 4.12 shows the reconstructed invariant mass distribution passing the  $\Lambda$  selection. The softest track of

the decay is used to build a pure  $\pi$  sample. The  $p\pi$   $dE/dx$  separation can therefore be measured as a function of the particle momentum. The  $dE/dx$  vs  $p$  distribution of the purely identified protons and pions is visible on Figure 4.13. Similar distributions for the  $dE/dx$  discriminators are shown on Figure 4.14.

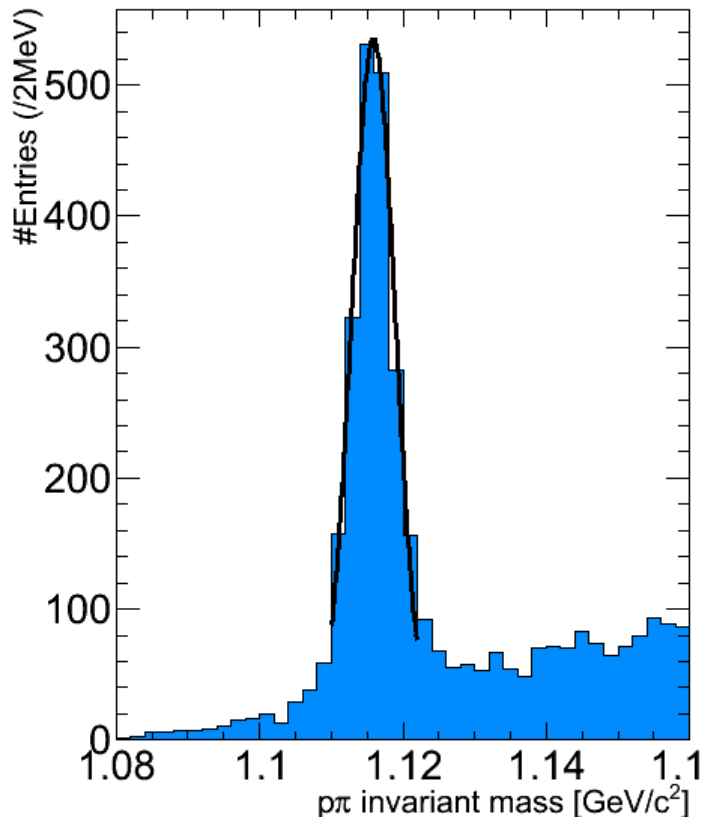


Figure 4.12: Invariant mass distribution of the reconstructed  $\Lambda$  decay into a pion and a proton. Bulk of the distribution is used to identify pure proton and pion sample.

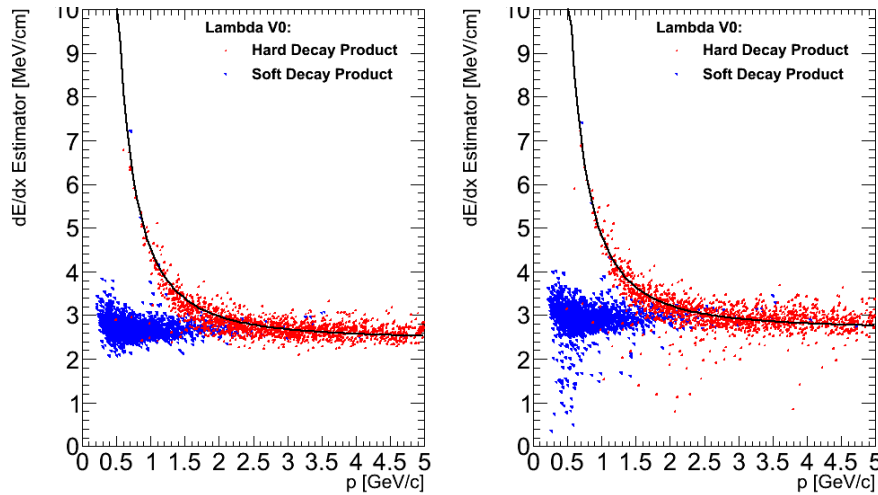


Figure 4.13: Distribution of the MP  $dE/dx$  estimator versus the track momentum for hardest track (assumed to be protons) and softest track (assumed to be pions) from  $\Lambda$  decays. Left is for truncated-40 estimator and right is for harmonic-2 estimator. On the right plot, the points falling far from the proton line are again due to the high sensitivity of the harmonic-2 estimator to clusters with a small charge.

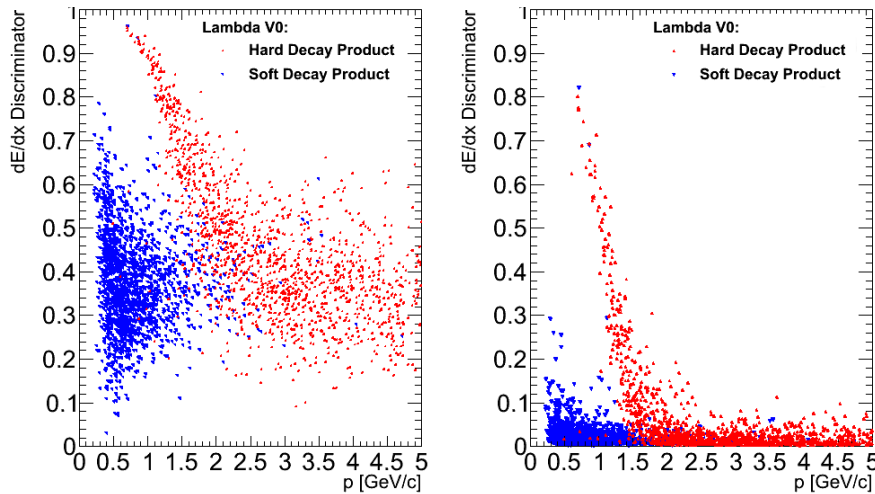


Figure 4.14: Distribution of the  $dE/dx$  discriminator versus the track momentum for hardest track (assumed to be protons) and softest track (assumed to be pions) from  $\Lambda$  decays. The left plot is for product discriminator and right is for asymmetric Smirnov discriminator.

## 4.6 Cluster Cleaning Algorithm

Despite the precautions taken to define MP  $dE/dx$  estimators and discriminators, avoiding bias toward higher charge by few strip cluster with an anomalously high charge, such clusters are still the main contribution to the HSCP background. It is important to avoid the use of pathological clusters in the search for HSCP. Therefore, a cluster cleaning algorithm [62, 63] has been defined to tag the clusters with an unexpected shape. These clusters are due to overlapping MIP tracks, nuclear interactions or  $\delta$ -rays in the silicon strip tracker detectors. Examples of such cluster with an unexpected shape are visible on Figure 4.15 and Figure 4.16. The first example shows the cluster resulting from the passage of two MIPs in the same sensor area. The cluster resulting from each MIPs overlaps to form a unique cluster with two maxima. The second example shows the cluster resulting from the production of an hard  $\delta$ -ray by the incident ionizing particle. The  $\delta$ -ray is energetic enough to ionize the silicon sensor. The reconstructed cluster has a unique maximum but an anomalous tail on the  $\delta$ -ray side. The tagged ( $\Delta E/\Delta x$ ) measurements are then simply ignored by the estimators and discriminators. These clusters are still used by the tracking algorithm, so the measured particle momentum is not affected by this cleaning.

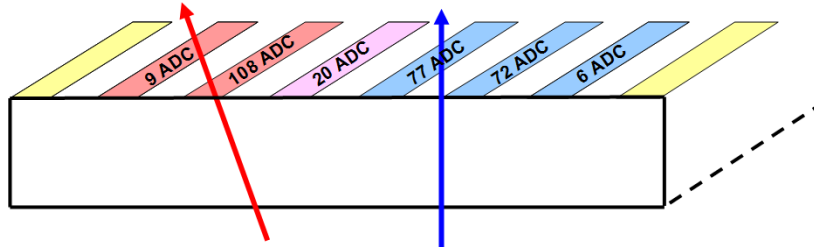


Figure 4.15: Illustration of a silicon strip cluster with a clear double maximum induced by the passage of two particles in the same silicon area.

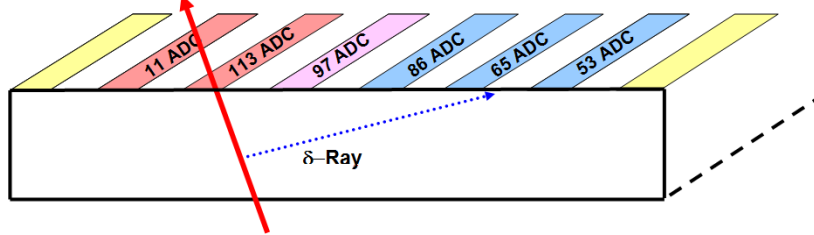


Figure 4.16: Illustration of a silicon strip cluster induced by the passage of a MIP in the silicon sensor. The cluster shape is affected by an hard  $\delta$ -ray emission.

Genuine single tracks produce clusters with most of the physical charge distributed over one or two neighboring strips and with other strips carrying only the fraction of this charge that is induced via capacitive coupling or cross-talk effects. Clusters with multiple charge maxima, as well as clusters with more than two consecutive strips containing high and comparable charge are tagged by the cleaning algorithm. A further check is performed on the strips that do not carry the largest or the second largest fraction of the overall cluster charge. It verifies that the charge on these strips is not highly incompatible with the strip noise plus the charge induced from the two strips carrying the largest fraction of the cluster charge. In a first approximation the induced charge is assumed to be equal to  $10^{-n}$  the charge of the two strips with the higher charge, where  $n$  is the distance in units of strips.

This algorithm was tested on data using high quality tracks with a low momentum ( $p < 5 \text{ GeV}/c$ ) and at least 8 hits. The Figure 4.17 shows the distribution of the charge and the size of cluster reconstructed on the first layer of the TIB. As it is visible on this figure, a large fraction of clusters rejected by the algorithm has an anomalously high charge and/or number of strips. That implies an important reduction of the HSCP background. The fraction of rejected clusters is 22% of the total.

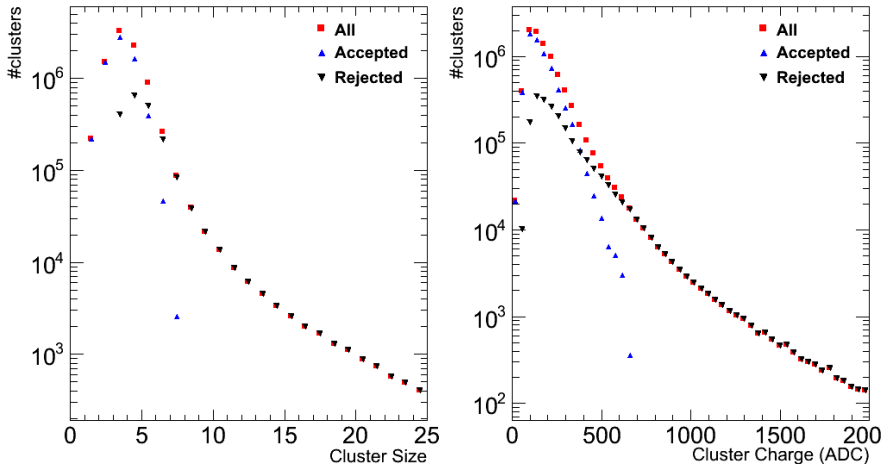


Figure 4.17: Silicon strip cluster size (left) and charge (right) for high quality tracks of  $>7$  hits and a low momentum ( $p < 5 \text{ GeV}/c$ ).

In order to use this algorithm for the search for HSCP, it is important to show that it is not rejecting clusters compatible with an HSCP signature and that the algorithm is not therefore reducing the HSCP signal efficiency of the analysis. Two techniques are used for this validation. The first method is simply based on the simulation of HSCP tracks ( $200$  and  $500 \text{ GeV}/c^2 \tilde{g}$ ). The cluster size and cluster charge distributions

of such events are shown for the first TIB layer on Figure 4.18. It is observed that, as expected, the distribution are similar to the one shown before with tracks of low momentum. The fraction of rejected cluster in  $\sim 20\%$  and  $\sim 30\%$  of the total for 200 and 500  $\text{GeV}/c^2 \tilde{g}$  respectively.

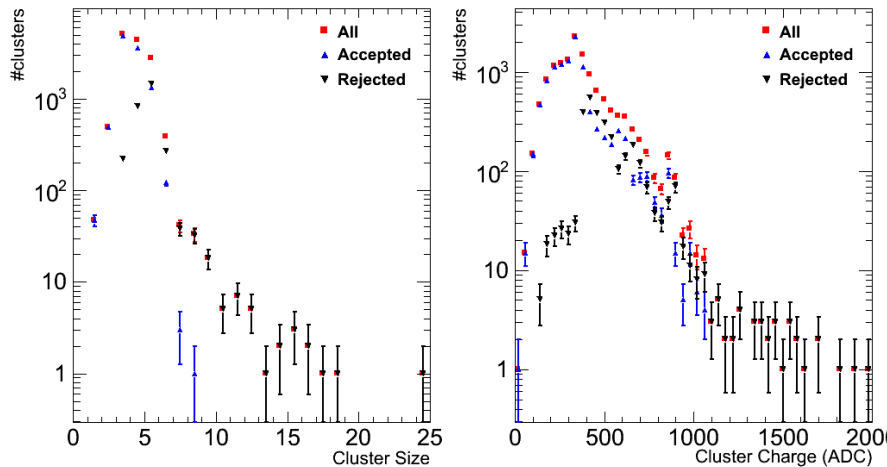


Figure 4.18: SST cluster size and charge for 200  $\text{GeV}/c^2 \tilde{g}$  tracks of  $>7$  hits.

The second test is not based on the simulation but instead on the LHC data. The idea is to use the identified deuterons as candle for highly ionizing particles like the HSCPs. The main difference between the deuterons and the HSCP resides in their momentum spectrum which is much stronger for HSCP. Therefore, the deuterons are expected to be slightly more bent and therefore to have a larger cluster size. Larger cluster are rejected more frequently by the cleaning algorithm so the results obtained with the deuteron candle are thus expected to be a pessimistic expectation for HSCP with similar ionization. Deuterons are selected in a mass windows ( $1.3 \text{ GeV}/c^2 < m < 2.2 \text{ GeV}/c^2$ ) and with a MP  $dE/dx$  threshold ( $>4.5 \text{ MeV}/\text{cm}$ ). Moreover, in order to avoid deuterons significantly bent, it is also required that the identified deuterons satisfy the following conditions:  $|\eta| < 0.3$  and  $p_T > 1.1 \text{ GeV}/c$ . The results with such tracks are shown on Figure 4.19. The number of rejected cluster is also about 20%.

Losing 20% to 30% of the  $(\Delta E/\Delta x)$  measurements is not dramatic for the signal search, since in average the HSCP tracks are made of  $\sim 15$  measurements. And indeed, the MP  $dE/dx$  estimator or  $dE/dx$  discriminator distributions are not strongly affected by the removal of the tagged cluster, it is even improved in several cases. On

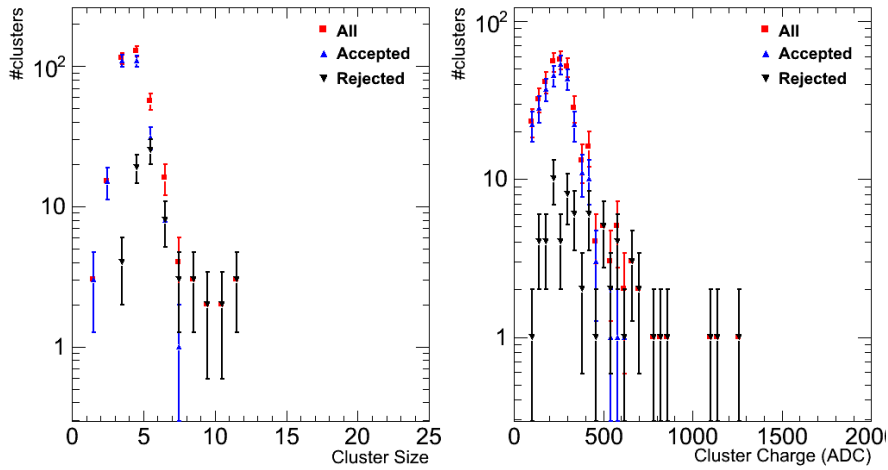


Figure 4.19: SST cluster size and charge for tracks of  $>7$  hits with a high ionization and identified as deuteron.

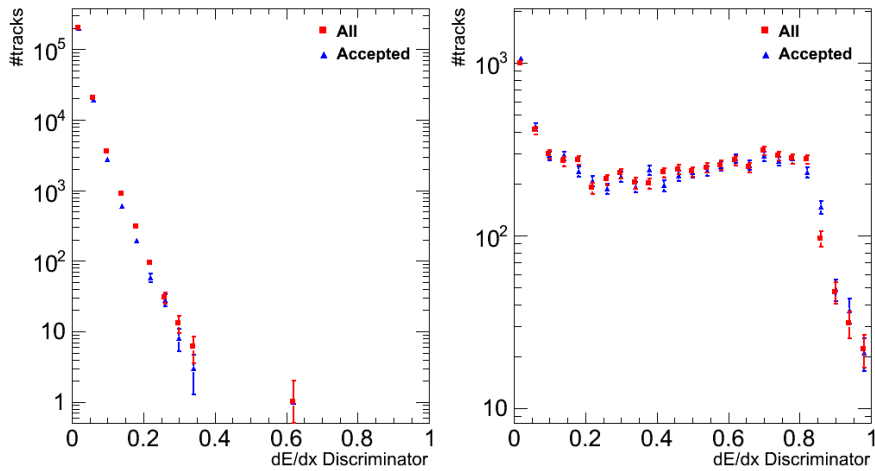


Figure 4.20: Distribution of the  $I_{as}^d$  discriminator for minimum ionizing particles (left) and for  $200 \text{ GeV}/c^2 \tilde{g}$  (right). The discriminator is built from all the SST clusters associated to the track or only from the ones accepted by the cluster cleaning algorithm.

the other hand, the tail of the background distribution is significantly reduced. This two observations are illustrated by the Figure 4.20.

## 4.7 Conclusion

Particle identification tools developed in this chapter have been completely validated using low momenta hadrons from  $pp$  collisions. Relatively good agreement between data and Monte Carlo is found at the exception of the lack of deuterons in the simulation. It was highlighted that these nuclei are never produced by the PYTHIA generator. This discrepancy in the particle content of the simulation with respect to real collisions is not expected to have any impact on the HSCP search, since in this analysis, only tracks of high momentum are considered. A procedure for mass reconstruction based on the ionization energy loss was developed and validated as well.

Finally, a cluster cleaning algorithm was described and the impact of its usage for the HSCP search has been quantified. This algorithm can certainly be fine-tuned further to lower the rejection of clusters compatible with an HSCP signal without reducing too much the cleaning of "background" clusters. However, it was shown that the current tuning is not problematic for the analysis, since the signal  $dE/dx$  distribution is not strongly affected by the 20% to 30% of removed clusters.

$dE/dx$  tools are therefore ready to be used for the search for Heavy Stable Charged Particles.



Chapter **5**

# Search for Heavy Stable Charged Particles

This chapter is the core of this document, it is divided in several sections. The first one introduces to the presented analysis. The second section details the data, monte carlo backgrounds and signal samples used. The online and offline selections are presented in the third and fourth sections. Then, performances of the HSCP mass reconstruction using  $dE/dx$  are discussed. A data-driven technique for the prediction of the number of analysis backgrounds is explained in the section 5.6. Finally, the results for this search are given as well as the systematic uncertainties affecting these results and some perspectives for the future.

The results presented in this chapter have also been summarized in a CMS Physics Analysis Summary [64, 65], published for the ICHEP2010 conference where early results of LHC experiments have been presented for the first time. A paper to be published in a scientific journal is also being written.

## 5.1 HSCP Signature

As detailed in chapter 1, the Heavy Stable (or long-lived) Charged Particles (HSCPs) appear in various extensions to the Standard Model. If the lifetime is long compared to the transit time through the detector, then the particle may escape the detector, thereby evading the limits imposed by direct searches for decay products. Nevertheless, a HSCP will be directly observable in the detector through the distinctive signature of a

slowly moving, high momentum particle. The low velocity results in an anomalously long time-of-flight and large ionization-energy loss rate ( $dE/dx$ ). Even if strongly interacting (R-hadron), HSCP will be highly penetrating and will most likely be identified as a muon.

The HSCPs have therefore a unique signature since they are reconstructed track:

- with a high momentum ( $p$ )
- with a high ionization energy loss ( $dE/dx$ )
- with a high time-of-flight (TOF) measured by the muon system/calorimeters
- identified as muon (pointing to activated muon chambers)

These four independent signatures can be combined to suppress the background to an almost null level, this was demonstrated on a MC study with  $1 \text{ fb}^{-1}$  [66]. But, at this stage, the time-of-flight technique is not yet commissioned and can therefore not be used.

Also, the interactions experienced by R-hadrons in matter can lead to charge-flipping, meaning that the particle can change its electric charge to become neutral or oppositely charged. A recent study shows that the probability for gluino or sbottom-based R-hadrons to emerge as neutral particles in the muon systems is close to unity [11]. If this prediction reveals to be true, the HSCP R-hadrons will be unobservable in the muon system. Consequently, both the long time-of-flight signature and the muon identification of the track are therefore unusable in that situation. For these reasons, the search is performed with two complementary candidate selections on tracks reconstructed in the inner tracker detector:

1. tracker-only selection: tracks are required to have a high  $dE/dx$  and high  $p_T$
2. tracker+muon selection: tracks are required, in addition of having a high  $dE/dx$  and high  $p_T$ , to be loosely identified as muons or simply pointing toward region of the muon detector where some activity is detected.

The analysis isolates HSCP candidates by selecting tracks reconstructed in the inner tracker detector with high  $dE/dx$  and high  $p_T$ . A second selection additionally requires that the tracks are identified as muons. For both selections, the mass of the candidate is then calculated from the measured  $p$  and  $dE/dx$  as detailed in chapter 4.

The search is performed as a counting experiment in the mass range of 75 to  $2000 \text{ GeV}/c^2$  to allow sensitivity to HSCP masses as low as  $100 \text{ GeV}/c^2$ . For the tracker+muon identification analysis, which is geared toward the detection of lepton-like HSCPs, the

100 GeV/c<sup>2</sup>  $\tilde{t}_1$  signal is used for the optimization, while the 200 GeV/c<sup>2</sup>  $\tilde{g}$  signal is used to optimize the tracker-only analysis.

## 5.2 Signal and Standard Model Background

Data from the initial LHC runs at  $\sqrt{s} = 7$  TeV, from April to September 2010, are analyzed. Data were collected with high transverse momentum ( $p_T$ ) muon, jet and missing transverse energy ( $E_T^{\gamma}$ ) triggers. These data correspond to an integrated luminosity of 3.06 pb<sup>-1</sup>. The number of triggered events is about 1.2M events.

A minimum bias MC sample enriched with events at high transverse momentum-transfer QCD interactions ( $\hat{p}_T > 30$  GeV/c) and containing approximately 0.7M triggered events is also used in the analysis for comparison with data. These MC events are weighted in order to reproduce the integrated luminosity of the analyzed datasets.

A few simulated signal samples are also used in this analysis, they are coming from the benchmark model already described in chapter 1. Events with direct production of supersymmetric scalar top squarks ( $\tilde{t}_1$ ) are produced, with masses of 130, 200, 300, 500 and 800 GeV/c<sup>2</sup>, with PYTHIA [13]. The showering and the hadronization are performed with the same tool.

The exercise of producing similar events with another generator, MadGraph [38], was also performed. The latter generator was interfaced to PYTHIA for the showering and hadronization steps. Precautions are needed to combine this two tools, in particular, the so called "MLM" [67] matching prescription was applied after showering in order to yield a realistic spectrum of associated gluons. The matching thresholds were optimized for the different masses: the  $Q_{cut}$  and  $x_{qcut}$  parameters were set respectively to 20 and 30 GeV for  $\tilde{t}_1$  masses of 130, 200 and 300 GeV/c<sup>2</sup>, and to 30 and 50 GeV for  $\tilde{t}_1$  masses of 500 and 800 GeV/c<sup>2</sup>. The kinematic distributions for the two generated samples were fully compatible. The PYTHIA sample is therefore used for the results of this chapter.

Events with direct pair production of gluino ( $\tilde{g}$ ) of different masses are generated with PYTHIA. Direct pair production of  $\tilde{t}_1$  and  $\tilde{g}$  is at leading-order model independent as the only relevant parameter is the mass of the  $\tilde{t}_1$  and  $\tilde{g}$ , respectively.

The  $\tilde{t}_1$  and  $\tilde{g}$  are treated as stable in all these samples. Their hadronization is performed by PYTHIA. The fraction of produced R-gluonballs ( $\tilde{g}g$  state) is an unknown parameter of the hadronization model and affects the fraction of R-hadrons that are neutral at production. If not stated otherwise, the fraction of produced R-gluonballs is equal to 10%, which is the usual value used in the literature. The HSCP interaction with matter is modeled as briefly explained in section 1.2 and fully described in

Ref. [68]. A more pessimistic interaction model, based on the previous one, is also considered. In the later model, the nuclear interaction of a charge R-hadron with matter always results in a charge flipping of the particle to a neutral R-hadron. This pessimistic model is motivated by the important uncertainty on the model describing the nuclear interaction of HSCPs with matter and by the conclusions of a recent study [11] which states that the probability for gluino or sbottom-based R-hadrons to emerge as neutral particles after traversing an amount of material typical of the calorimeters or iron yokes of the LEP, Tevatron [12] or LHC experiments is close to unity.

Production of supersymmetric quasi-stable leptons ( $\tilde{\tau}_1$ ) at the LHC can proceed either directly or via production of heavier supersymmetric particles (mainly squarks and gluino pairs), which decay leading to one or more  $\tilde{\tau}_1$  particles at the end of the decay chain. The latter process is in general dominant due to the electroweak nature of the direct production process.

In this analysis, the minimal gauge mediated supersymmetry breaking (mGMSB) model [69] is selected as a benchmark for lepton-like HSCPs. Two benchmark points on the SPS line 7 [70] are considered. The particle mass spectrum and the decay table are produced with the program ISASUGRA [71] version 7.69. The common parameters for the two considered points are:  $\tan \beta = 10$ ,  $\text{sign}(\mu) = 1$ ,  $c_{\text{grav}} = 10000$ , while the changing part is:

- $\tilde{\tau}_1(156) : N = 3, \Lambda = 50 \text{ TeV}, M = 100 \text{ TeV}$
- $\tilde{\tau}_1(247) : N = 3, \Lambda = 80 \text{ TeV}, M = 160 \text{ TeV}$

The corresponding  $\tilde{\tau}_1$  masses are 155.8 and 247  $\text{GeV}/c^2$ . The squark and gluino masses are of about 1.1 and 1.7  $\text{TeV}/c^2$ , respectively. A few more mass points are obtained by varying the  $\Lambda$  parameter in order to cover a mass range from 100 to 300  $\text{GeV}/c^2$ . For all points, the squark and gluino production cross sections are between one and two orders of magnitude higher than that of direct  $\tilde{\tau}_1$  pair production.

### 5.3 Online Selection

The events used in this analysis are collected with three types of triggers: triggers requiring a single muon ( $p_T > 9 \text{ GeV}/c$ ) or a pair of muons ( $p_T > 3 \text{ GeV}/c$ ), triggers requiring  $E_T > 100 \text{ GeV}$  (to search for HSCPs emerging mainly neutral after traversing the calorimeters or for HSCPs failing the muon HLT reconstruction) or triggers requiring important hadronic activity: one jet ( $p_T > 100 \text{ GeV}/c$ ), two jets ( $\langle p_T \rangle > 100 \text{ GeV}/c$ ) or four jets ( $p_T > 25 \text{ GeV}/c$ ). The jet triggers are mainly used to search for HSCPs accompanied by substantial hadronic activity.

Trigger and reconstruction efficiencies in the muon detectors are limited by requirements on the arrival time of the tracks to the muon system. These requirements can affect the efficiency for detecting slow HSCPs. The dependence of the muon trigger efficiency on the particle  $\beta$  is studied using Monte Carlo (MC) simulations. The muon trigger efficiency starts dropping linearly at  $\beta = 0.7$  and reaches very low values at  $\beta = 0.3$ , as shown on Figure 5.1 for a 200 GeV/c<sup>2</sup> gluino and a 100 GeV/c<sup>2</sup>  $\tilde{\tau}_1$  MC sample. Heavier particles are generally slower, therefore the muon trigger efficiency is lower for these HSCPs. However, these heavier HSCPs are generally produced with a significant number of accompanying hadronic particles, resulting in the presence of a significant amount of hadronic energy in the calorimeters that leads to a high trigger efficiency. For the pessimistic HSCP models, the efficiencies of the muon paths are almost null (< 1%).

Signal event selection efficiencies for the various trigger path considered in this analysis are visible on Figure 5.2. The left part of the figure shows the absolute trigger efficiency for HSCP MC events, it is defined as the number of events passing a given HLT path divided by the total number of events considered. The three last columns are efficiencies for the total muon efficiency (OR of all the muon paths), the total JetMET efficiency (OR of all the Jet+ $E_T$  paths) and for the total overall efficiency (OR of all the paths). The right part of the figure shows the incremental trigger efficiencies that are defined as the number of events that are passing a given HLT path but not the previous ones. Given that the single muon path is the first path, its incremental efficiency is strictly equal to the absolute one.

The two behaviors discussed before are well visible: The muon trigger efficiency decreases for higher HSCP masses and the JetMET trigger efficiency increases for higher HSCP masses.

It is also clear that the muon trigger efficiency is significantly lower for R-hadron HSCPs. The main reason for this difference is simply that a significant fraction of these events are not containing any charged R-hadrons and therefore can not be triggered by the muon system. For pair-produced  $\tilde{g}$  hadronizing into R-gluonballs in 10% (50%) of the cases, the fraction of events containing two neutral R-hadrons at production is 30% (60%). Also the muon  $\eta$  spectrum of the R-hadron HSCPs ( $\tilde{g}$  and  $\tilde{\tau}_1$ ) is less central than for  $\tilde{\tau}_1$ , see Figure 1.4. Finally, the  $\tilde{\tau}_1$  production, dominated by a decay chain mechanism of heavier particles, results in the production of a significant amount of hadrons that allows for a high JetMET trigger efficiency.

In conclusion, the trigger efficiencies for the signal are as follows: for R-hadrons, the jet and  $E_T$  trigger efficiencies range from 10% (low mass) to 45% (high mass), while the muon trigger efficiencies range from 10% (high mass) to 25% (low mass). For the

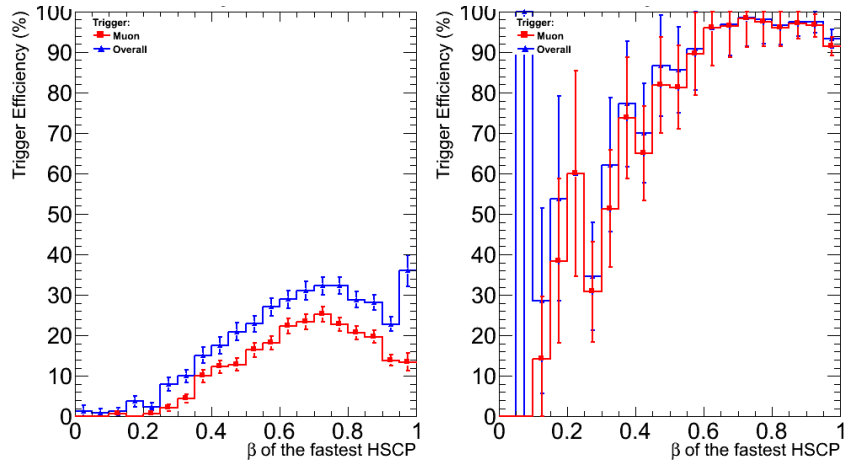


Figure 5.1: Total and Muon trigger selection efficiencies as a function of the velocity ( $\beta$ ) of the fastest HSCP in the event for a  $200 \text{ GeV}/c^2$  gluino (right) and a  $100 \text{ GeV}/c^2 \tilde{\tau}_1$  (left) MC sample. The trigger muon efficiency is slightly lower for  $\beta \sim 1$  due to kinematics acceptance, indeed HSCPs with  $\beta \sim 1$  are generally produced at high  $\eta$ .

$\tilde{\tau}_1$  signal, the jet and  $E_T$  trigger efficiencies are above 50%, while the muon triggers are above 90% efficient. The resulting total trigger efficiency, defined as the logical OR of these triggers, is greater than 20% for R-hadrons and 90% for the  $\tilde{\tau}_1$  signal.

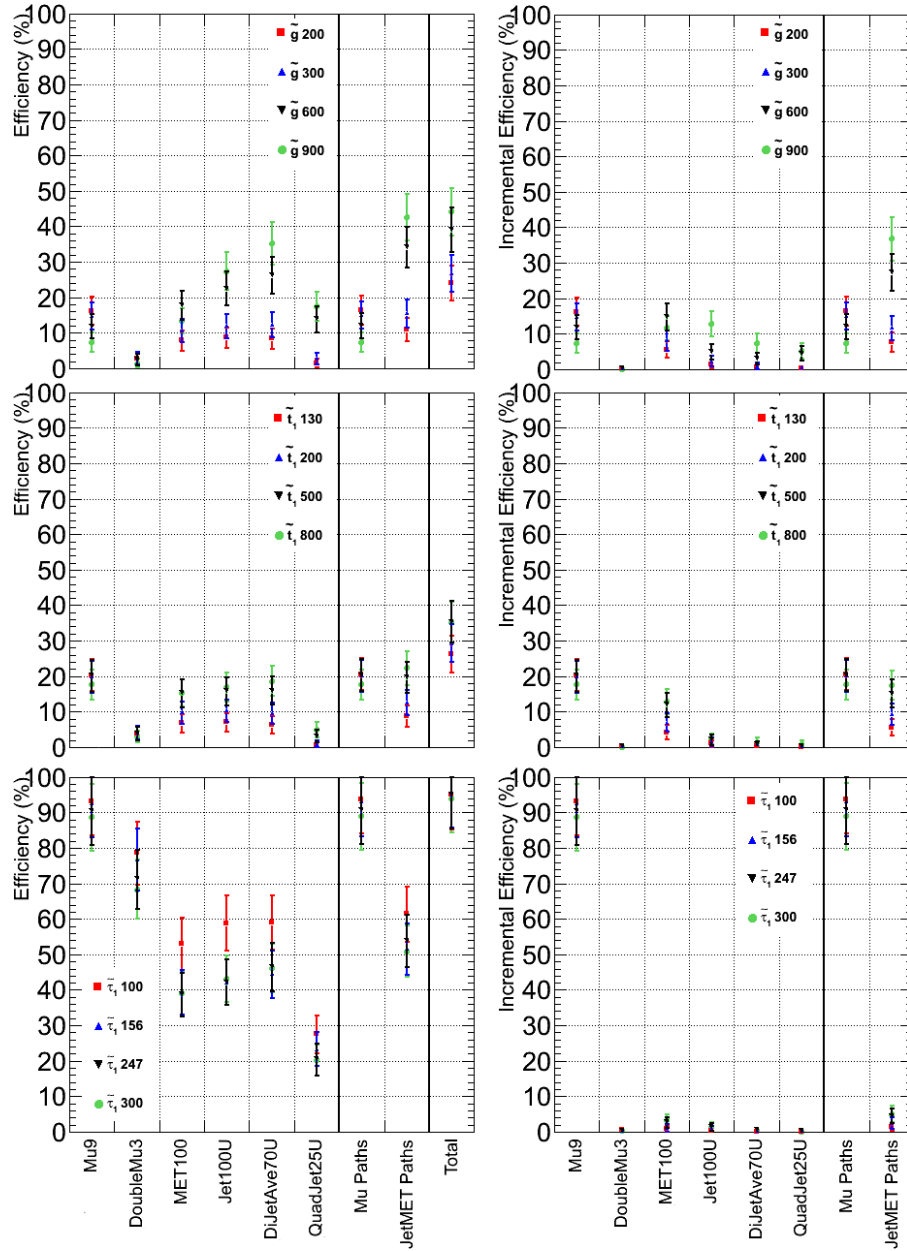


Figure 5.2: Trigger absolute and incremental selection efficiencies, as defined in the text, for the various considered trigger paths and for different HSCP models and masses.

## 5.4 Offline Selection

As already anticipated, two selections are used in this analysis to define HSCP candidates: a "tracker-only" and a "tracker+muon" identification selections. Both selections require an individual track, reconstructed in the inner tracker detector, which satisfies the standard CMS track reconstruction algorithm [58]. For the muon-like selection, additionally, the track must be loosely identified as a muon or simply points toward a detector area with muon activity (it must be either a "global muon" or "tracker muon" [72]). Same triggers are used for these two selections.

For both selections, only the associated silicon tracker track is used for the  $p$  and  $dE/dx$  measurements. The particle momentum is taken as the measurement of the track momentum at the point of closest approach to the reconstructed primary vertex. Muon candidates sharing the same inner tracker track are vetoed.

Candidates, defined as inner track of high quality with a  $p_T$  greater than 15 GeV/c, must have at least three  $\Delta E/\Delta x$  SST measurements, in order to have a reliable MP  $dE/dx$  estimation or discriminating value. Candidates are further pre-selected by requiring a relative uncertainty on the measured  $p_T$  smaller than 40% and a longitudinal (transverse) impact parameter with respect to the reconstructed primary vertex,  $dz$  ( $dxy$ ), smaller than 2 (0.25) cm. The Figure 5.3 and 5.4 show the distributions of the previous quantities before the threshold is applied. The second (third, fourth, etc.) distribution of the figure only contains the candidates that pass the threshold, on the first (second, third, etc.) distribution, applied at the previous step. A reasonable agreement between data and MC is also shown on these figures. The main disagreement between the data and the simulation comes from the visible tail on the  $dz$  distribution, it is due to pile-up events that are not simulated in the MC samples used.

The various efficiencies of the candidate pre-selection for data, minimum bias MC and two signal benchmarks for the tracker+muon and tracker-only selections are summarized in the Table 5.1. This table highlights that this pre-selection is very soft and only reduces the far tail of the data distributions. It is mandatory to keep a sufficiently high number of tracks after the pre-selection in order to precisely predict the number of background tracks of the analysis.

Clean separation between HSCPs and SM particles can be achieved by selecting tracks with high  $p_T$  and high  $dE/dx$ . These two quantities are expected to be uncorrelated for MIPs, while a slow-moving HSCP would have a large  $dE/dx$  even at high  $p_T$ .

The  $dE/dx$  asymmetric Smirnov discriminator ( $I_{as}$ ) is used for the selection based on  $dE/dx$  since, contrary to the other discriminators, it measures the incompatibility

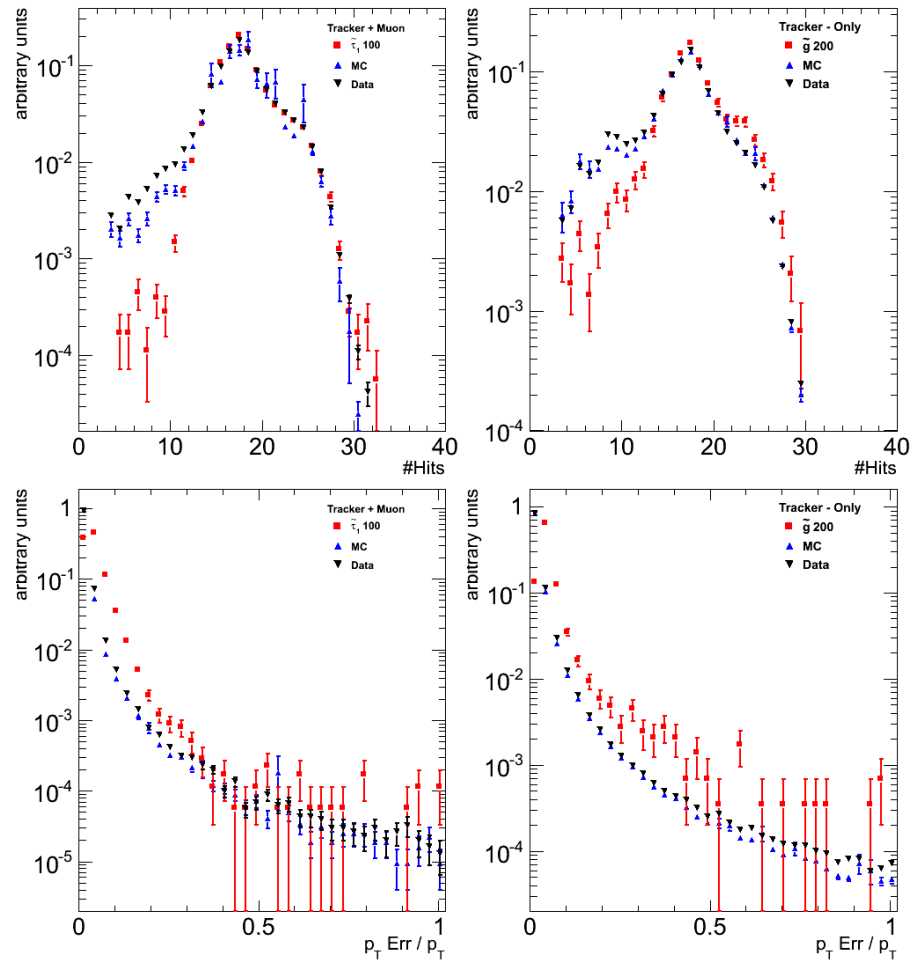


Figure 5.3: Top: Distribution of the number of  $\Delta E/\Delta x$  SST measurements of candidates before pre-selection. Bottom: Distribution of the relative error on  $p_T$  for the tracks of the above selection that have at least 3  $\Delta E/\Delta x$ . Plots on the left (right) are for the tracker+muon (tracker-only) selection in data, minimum bias MC, and signal.

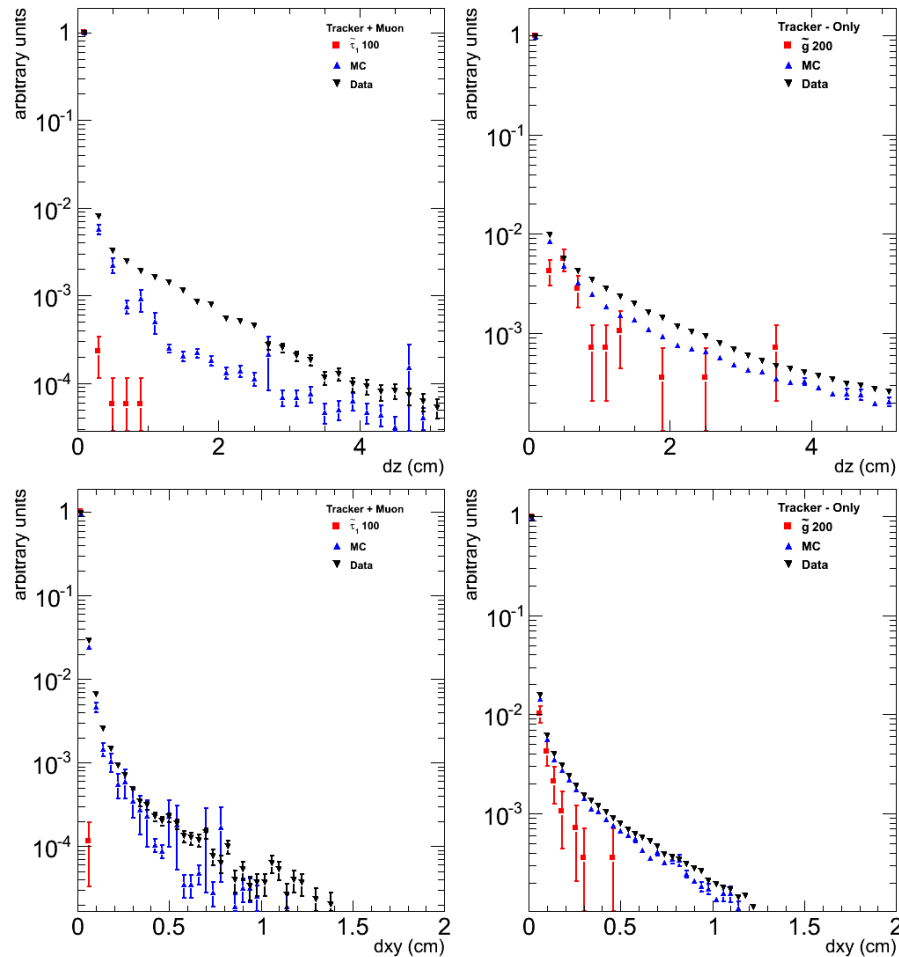


Figure 5.4: Top: Distribution of the longitudinal impact parameter ( $dz$ ) for candidates passing the previous cuts. Bottom: Distribution of the transverse impact parameter ( $dxy$ ) for candidates passing the previous cuts. Plots on the left (right) are for the tracker+muon (tracker-only) selection in data, minimum bias MC, and signal.

Tracker+muon	data	mc mb	$200 \text{ GeV}/c^2 \tilde{g}$	$100 \text{ GeV}/c^2 \tilde{\tau}_1$
initial n.o.candidates	314K	311K	452	7.10
n.o.hits ( $\Delta E/\Delta x > 3$ )	98.9%	99.2%	98.2%	99.9%
High quality track	99.7%	99.8%	99.9%	99.9%
Error on $p_T < 40\%$	99.8%	99.9%	98.9%	99.8%
$ dz  < 3 \text{ cm}$	99.4%	99.7%	99.9%	99.9%
$ dx_{\parallel}  < 0.25 \text{ cm}$	99.6%	99.7%	99.9%	99.9%
pre-selection efficiency	97.6%	98.5%	96.8%	99.7%
final n.o.candidates	306K	309K	438	7.08

tracker-only	data	mc mb	$200 \text{ GeV}/c^2 \tilde{g}$	$100 \text{ GeV}/c^2 \tilde{\tau}_1$
initial n.o.candidates	2.41M	2.29M	501	7.33
n.o.hits ( $\Delta E/\Delta x > 3$ )	96.4%	96.3%	97.4%	99.2%
High quality track	97.9%	98.4%	99.9%	99.9%
Error on $p_T < 40\%$	99.5%	99.6%	98.7%	99.7%
$ dz  < 3 \text{ cm}$	98.2%	98.6%	99.9%	99.9%
$ dx_{\parallel}  < 0.25 \text{ cm}$	98.4%	98.7%	99.9%	99.9%
pre-selection efficiency	90.9%	91.8%	96.0%	99.0%
final n.o.candidates	2.19M	2.11M	481	7.25

Table 5.1: Pre-selection efficiencies for data, simulated minimum bias background (mc mb), and two simulated signal benchmarks. The first (last) row indicates the number of candidates before (after) the pre-selection. Before this pre-selection, the candidates are just tracks with a  $p_T$  greater than 15 GeV/c. For the tracker+muon selection, the initial candidates also have a muon identification. All the numbers presented in this table are scaled to an integrated luminosity of  $3.06 \text{ pb}^{-1}$  in order to be comparable with the data column.

with the MIP hypothesis in terms of high ionization and not low one. Non-relativistic HSCP candidates will have  $I_{as}$  approaching unity. The cluster cleaning algorithm, described in chapter 4, was used to clean the input  $\Delta E/\Delta x$  collection used by the estimator and discriminator from the SST clusters affected by anomalous ionization contributions due to overlapping MIP tracks, nuclear interactions and hard  $\delta$ -rays in the silicon strip tracker detectors. It was shown that this cleaning has no significant impact on the value of the  $dE/dx$  estimator/discriminator for genuine HSCP track, but reduces significantly the background rates due to MIPs faking an HSCP signal.

Relatively good agreement between the data and the minimum bias MC sample, as well as strong discriminating power for the HSCP signal using  $I_{as}$  and  $p_T$ , is shown on Figure 5.5. The stability of these two variables from runs to runs was also studied as shown on Figure 5.6. The mean and R.M.S. of the  $I_{as}$  and  $p_T$  distribution are quite stable with time. Only few runs have a slightly different mean, this is a statistical effect appearing only in short runs, for which the mean is not properly estimated because of the small statistic available in the distributions.

The Figure 5.7 shows the  $I_{as}$  distributions for the candidates of the tracker-only selection in the data and MC sample passing the pre-selection with and without the cluster cleaning procedure, as well as the same distributions for the signal MC sample corresponding to a gluino with mass  $200 \text{ GeV}/c^2$  and  $900 \text{ GeV}/c^2$ , where only reconstructed tracks matched to the simulated HSCP particles are considered. The cluster cleaning procedure rejects background at high ionization without a significant impact on the signal. The background rejection is found to be lower for the muon-like candidates, most likely because muons do not undergo nuclear interactions.

As illustrated by Figure 5.9, the  $I_{as}$  distribution in data depends on the number of silicon strip clusters used for the  $dE/dx$  measurement. Small differences in the distribution are also observed for a fixed number of hits but for different  $\eta$  ranges. The latter differences are due to the different typical path-lengths in the different  $\eta$  regions, which results in improved  $dE/dx$  resolution. Differences in material may also results in different rates of secondary particle production. Therefore, in order to increase sensitivity, HSCP candidates are divided into subsamples according to the number of silicon strip hits and  $\eta$  intervals:  $0 < \eta < 0.5$ ,  $0.5 < \eta < 1$ ,  $1 < \eta < 1.5$ ,  $1.5 < \eta < 2$  and  $2.0 < \eta < 2.5$ .

As previously said, the actual signal selection is based on  $p_T$  and  $I_{as}$  thresholds applied to the pre-selected candidates. These thresholds are *a priori* different from one subsample to another. Because of this and due to the important number of subsamples, is it relatively complicated to fix individually all the thresholds. Instead, it was

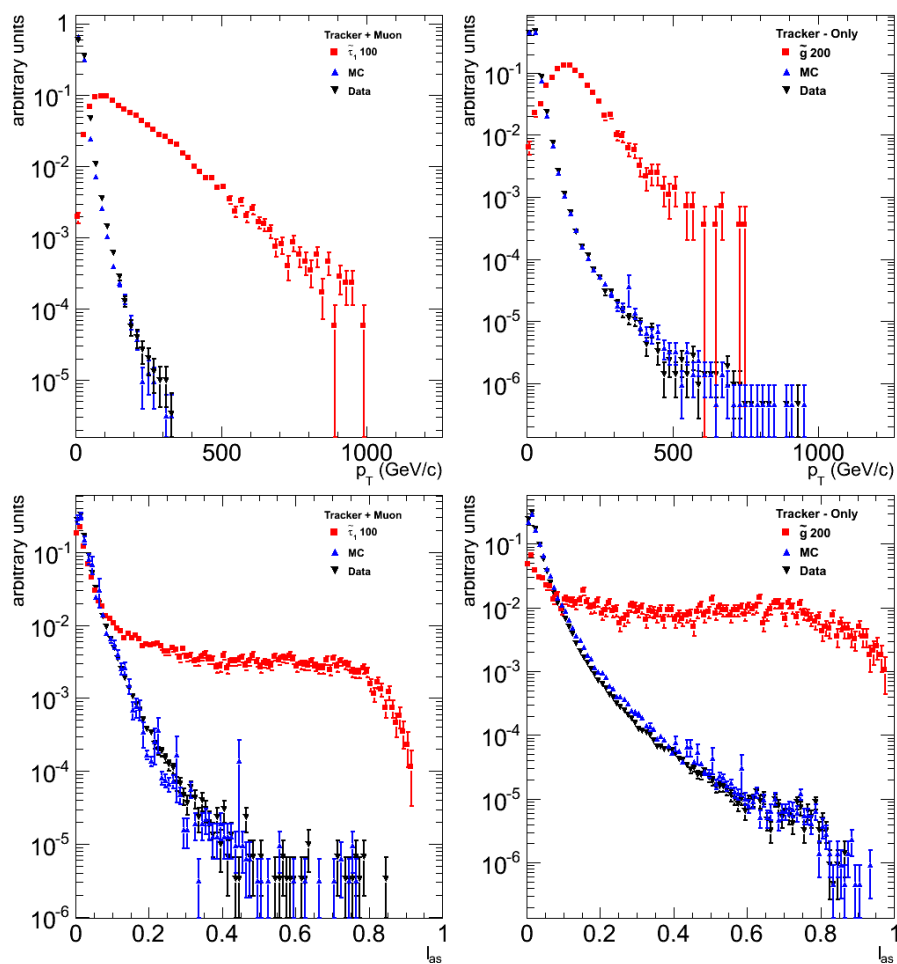


Figure 5.5: Distributions of  $p_T$  and  $I_{as}$  for candidates passing the pre-selection. Plots on the left (right) are for the tracker+muon (tracker-only) selection in data, minimum bias MC, and signal.

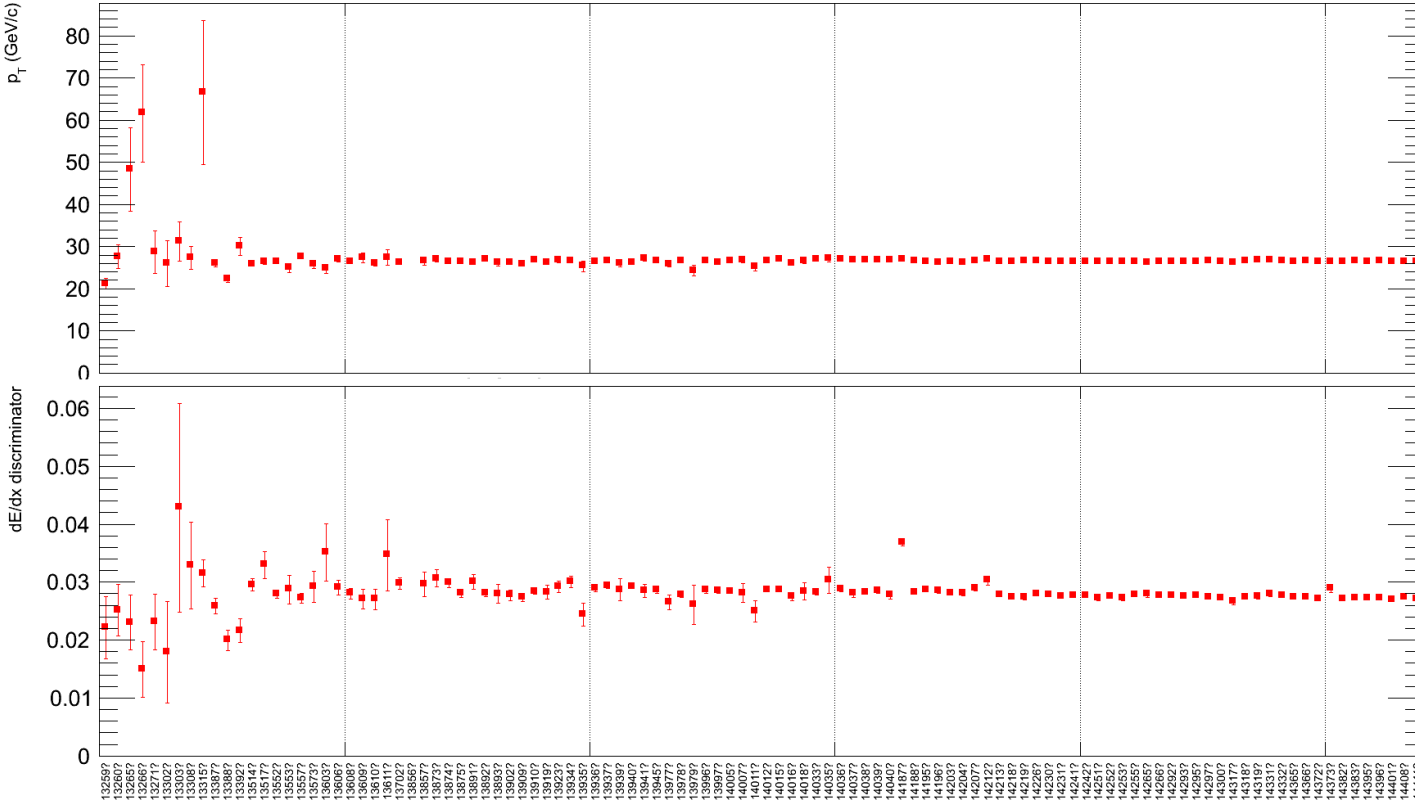


Figure 5.6: Distribution of the mean  $p_T$  (top) and mean  $I_{as}$  (bottom) for the pre-selected candidates as a function of the run of data taking. The error bars represent the R.M.S. of the distribution. The few outliers are due to statistical fluctuation affecting short runs. Runs are packed by 10 in order to have a readable X axis.

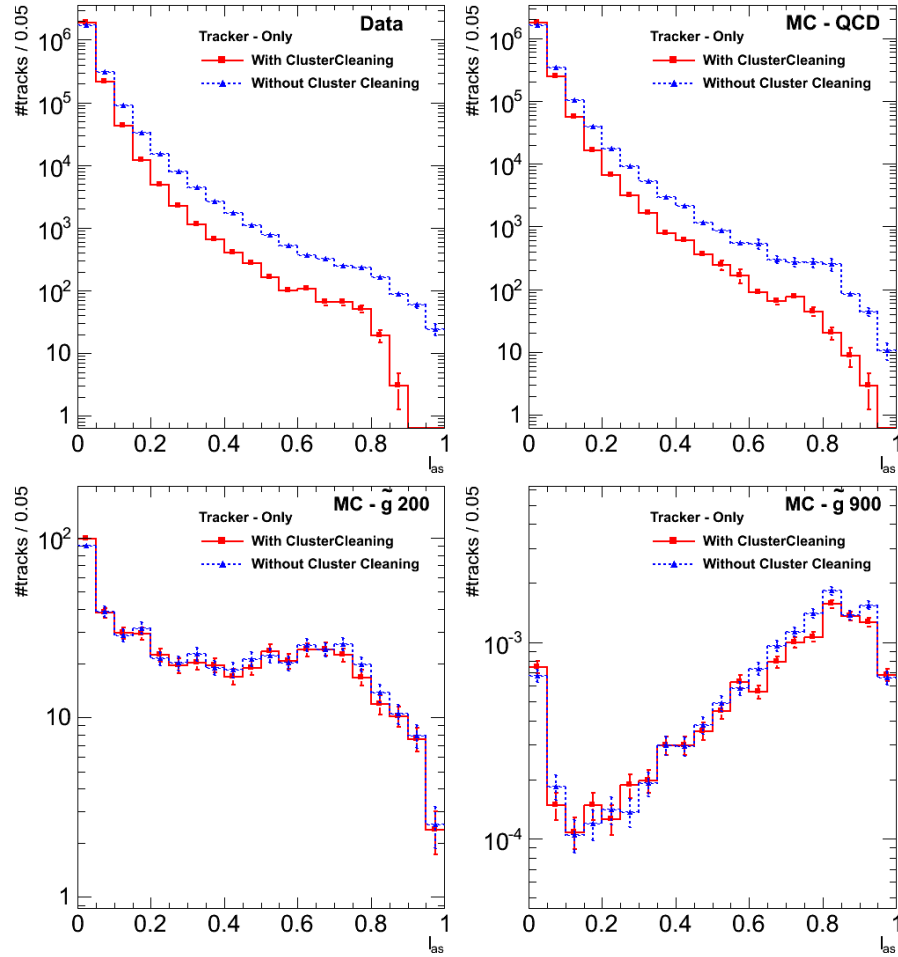


Figure 5.7: Top: distribution of  $I_{as}$  for the tracker-only data (left) and MC (right) candidates passing the pre-selection with and without the cluster cleaning procedure. Bottom: same distributions for a 200  $\text{GeV}/c^2$  (left) and 900  $\text{GeV}/c^2$  (right) gluino MC sample, where only reconstructed tracks matched to the simulated HSCP particles are considered. These distributions are normalized to the integrated luminosity of the analyzed datasets.

decided to fix the data selection efficiency obtained in each subsample with the  $p_T$  or  $I_{as}$  selection alone. Therefore, the threshold value is, in general, different from one subsample to another, but the resulting background efficiency is common to all subsamples. And the selection is entirely defined by the two selection efficiencies. In order to have a comparable number of entry in each subsample, and therefore comparable thresholds, the subsamples with less than 8 hits are merged together into one super-subsample. A similar procedure is applied on subsamples with more than 17 hits. Subdivision in eta for these two super-subsamples remains unchanged.

A study performed on MC [73] indicates that a selection using the  $I_{as}$  discriminator in the place of the  $I_h$  estimator increases the signal-to-noise ratio by a factor 3. The division in subsamples according to the track number of hits ( $\eta$ ) brings an additional increase by a factor 8 (1.3). The Figure 5.8 shows the increase in selected signal for a same number of predicted background events of this optimized selection with respect to other selections. The procedure to obtain the number of predicted events is defined later in this chapter. The optimization used (#hits +  $\eta$  splitting) clearly shows the best signal-to-noise ratio for both the tracker+muon and the tracker-only analysis.

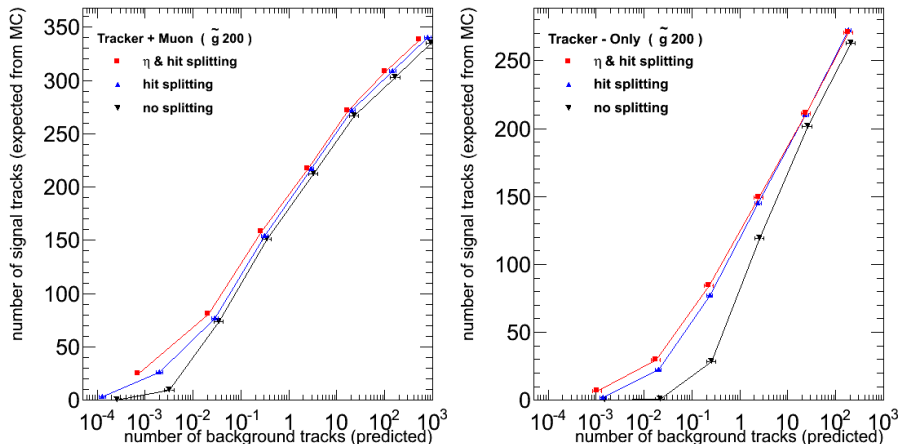


Figure 5.8: Expected number of signal candidates, as predicted by MC, versus the expected number of background candidates from a data-driven prediction in the search region. Left is for the tracker+muon selection; Right is for the tracker-only selection. In the two cases, the signal considered are  $200 \text{ GeV}/c^2 \tilde{g}$  R-hadrons. Three different selection optimizations are considered. Only tracks with at least 9 hits are used for the selection where no splitting in subsamples is applied. Otherwise, the background rate due to badly reconstructed tracks is too high.

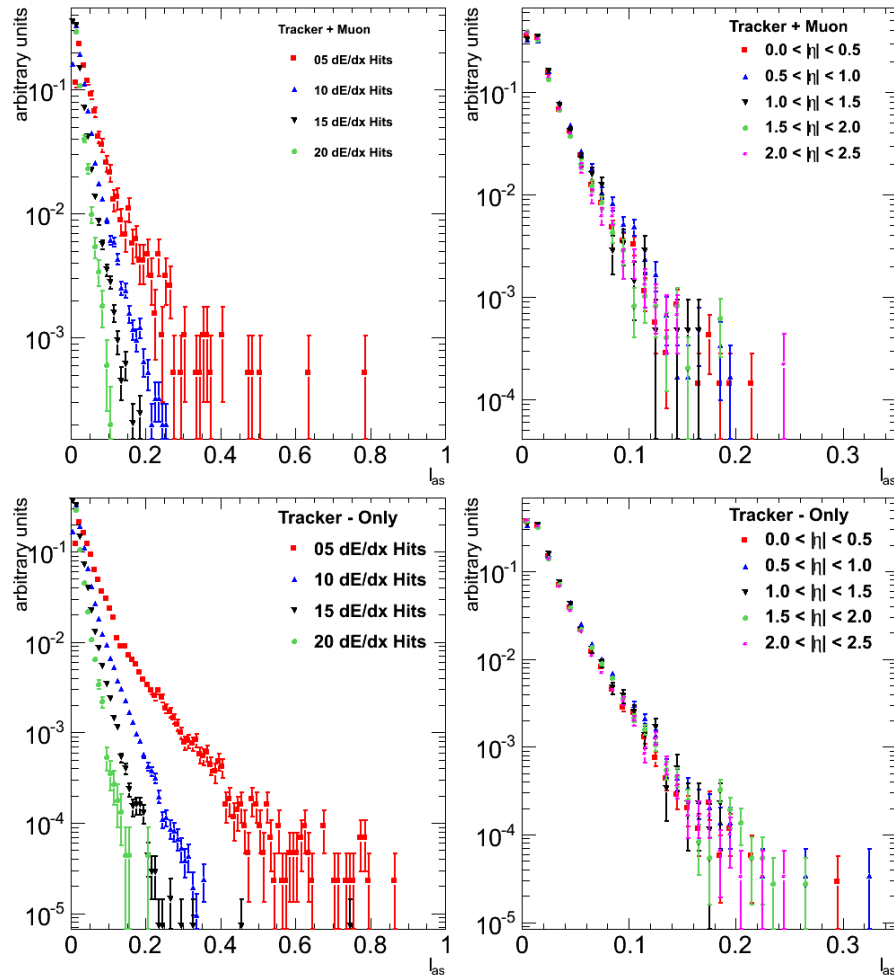


Figure 5.9: Left: Distributions in data of the  $I_{as}$  discriminator for tracks with different number of  $dE/dx$  measurements. Right: Distributions in data of the  $I_{as}$  discriminator for tracks with 15  $dE/dx$  measurements and in different  $\eta$  regions. Upper figures are for the tracker+muon selection; lower figures are for the tracker-only selection.

The Figure 5.10 shows, for the optimized selection where candidates have been split into subsamples, the number of data and signal observed for various imposed selection efficiency on data. The x-axis (y-axis) of these plots shows the selection efficiency imposed in each subsample using the  $p_T$  ( $I_{as}$ ) threshold alone. Because these two variables are uncorrelated, in first approximation the total selection efficiency imposed in one cell is therefore the product of the selection efficiency imposed on each axis.

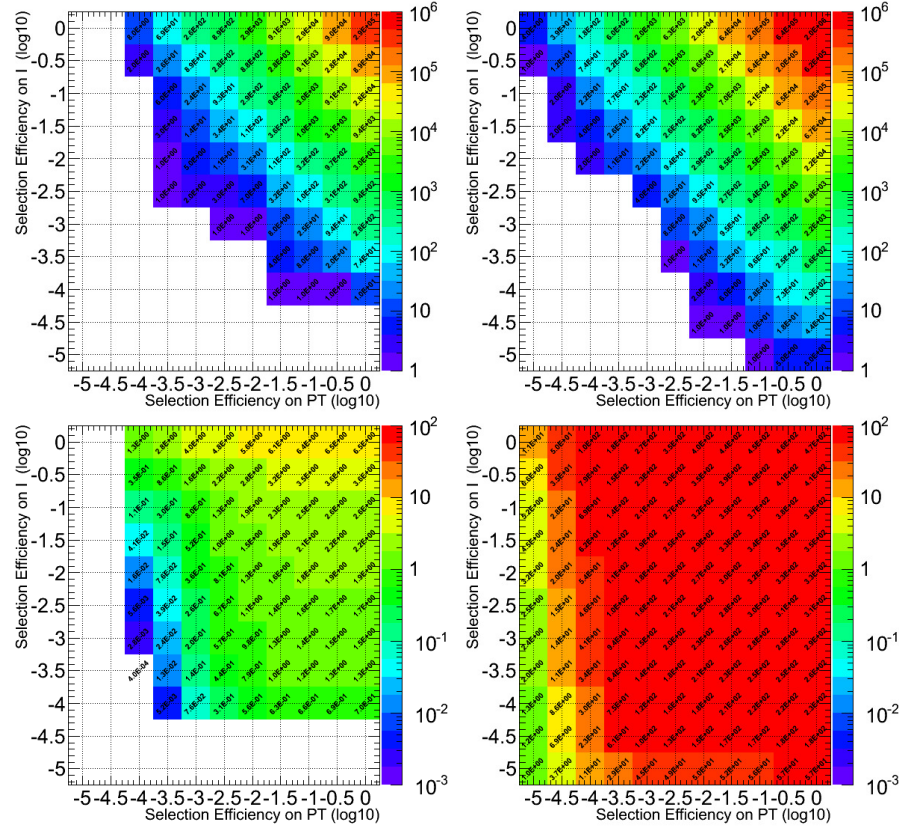


Figure 5.10: Observed number of candidates for various selection on  $p_T$  and  $I_{as}$ . Top left (Bottom left) is the number of candidates observed for data ( $100 \text{ GeV}/c^2 \tilde{\tau}_1$  signal) for the tracker+muon selection. Top right (Bottom right) is the number of candidates observed for data ( $200 \text{ GeV}/c^2 \tilde{g}$  signal) for the tracker-only selection. See text for more details. It was checked that the track surviving the selection up to  $\epsilon_{p_T} = 10^{-35}$  and  $\epsilon_{I_{as}} = 10^{-2.5}$  is not a strong HSCP candidate: its  $I_{as}$  is at 0.13 while the threshold for this subsample is at the same value, the value of the track MP  $dE/dx$  estimator is 3.61 MeV/cm, so not really far from the expected value for a MIP.

## 5.5 Mass Reconstruction

The mass of highly ionizing particles can be estimated using their specific energy loss and their momentum. For this analysis, the most probable value of the particle  $dE/dx$  is estimated using the harmonic-2 estimator ( $I_h$ ) and the simplified parameterization of the Bethe-Bloch formula, both described in chapter 4.

For mass values of  $100 \text{ GeV}/c^2$  or higher, the mass resolution is expected to be significantly worse than for low momenta hadrons mainly because of the deterioration of the resolution on the  $p$  measurement. Both the mass scale and the mass resolution are also affected by the silicon strip tracker ADC cut-off, which becomes increasingly more important as the HSCP  $\beta$  spectrum becomes softer.

Indeed, the lower the HSCP  $\beta$ , the higher its  $dE/dx$  and, therefore, the higher the chance of having some of its charge measurements truncated. For  $320 \mu\text{m}$  of silicon, truncation starts at  $\beta$  values as low as 0.55. This  $\beta$  threshold grows with the square root of the path length and reaches 1 (MIPs) for path lengths as long as  $900 \mu\text{m}$ . As a consequence, the measured HSCP  $I_h$  value will be underestimated and the resulting point in the 2-dimensional  $p$ - $I_h$  plane will depart from the corresponding constant-mass curve and populate regions at lower mass values. These effects are visible in Figure 5.11, which has been obtained using the MC  $\tilde{t}_1$  signal samples. The distributions of  $I_h$  and  $p$  for all reconstructed tracks passing the pre-selection and matching ( $\Delta R < 0.03$ ) a simulated HSCP in the event are shown in Figure 5.11 (left) along with the curves resulting from Eq. 4.2, where  $m$  is set to the nominal mass value. The small cloud of tracks in the lower left corner of the figure is due to mismatched reconstructed tracks produced by non-HSCP particles. The Figure 5.11 (right) shows the resulting mass spectra, normalized to the number of events expected for the integrated luminosity used in this analysis.

The degraded mass resolution and the bias in the mass peak position are not relevant for the analysis presented in this document, which is based on a counting experiment, as described in the next sections.

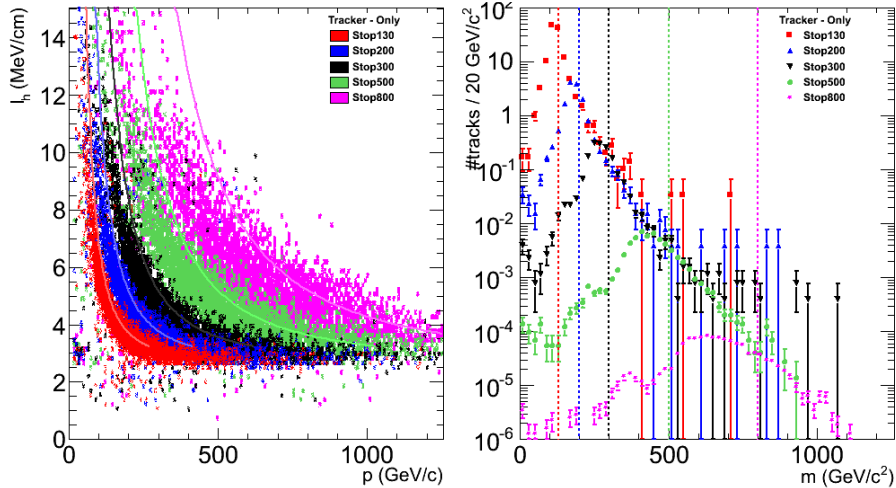


Figure 5.11: Left: Distributions of the reconstructed  $p$  and  $I_h$  for all tracks passing the pre-selection and matched to HSCP particles in the MC samples. The curves  $I_h = Km^2/p^2 + C$ , for the 5 nominal values of the mass, are also drawn. Right: reconstructed mass spectra for these tracks.

## 5.6 Data-Driven Background Determination

The estimation of the background is performed by exploiting the absence of significant correlation between the  $p_T$  and  $dE/dx$  measurements. The distributions of  $I_{as}$  and  $I_h$  for data for a control sample composed of candidates with  $7.5 < p_T < 20$  GeV/c and a signal-like sample composed of candidates with  $p_T > 20$  GeV/c are shown in Figure 5.12. The results obtained for both the tracker+muon and tracker-only candidates are presented. In both cases, the control and signal-like distributions are normalized to unity to allow the shapes to be compared. Good agreement is observed between the two distributions, which indicates that the assumption of lack of correlation between momentum and  $dE/dx$  is correct to a good approximation.

A data-driven method that exploits this lack of correlation is therefore used to estimate the background from MIPs. An estimation of the absolute number of background events passing the selection applied to the  $i^{th}$  subsample is obtained as  $D_i = B_i C_i / A_i$ , where  $A_i$  is the number of tracks in the  $i^{th}$  subsample that pass neither the  $I_{as}$  threshold nor the  $p_T$  one chosen for that subsample,  $B_i$  ( $C_i$ ) is the number of tracks that pass only the  $I_{as}$  ( $p_T$ ) threshold, and  $D_i$  is the number of background tracks that pass both thresholds. In addition to the non-correlation assumption, the technique above requires the implicit assumption that the signal contamination in the

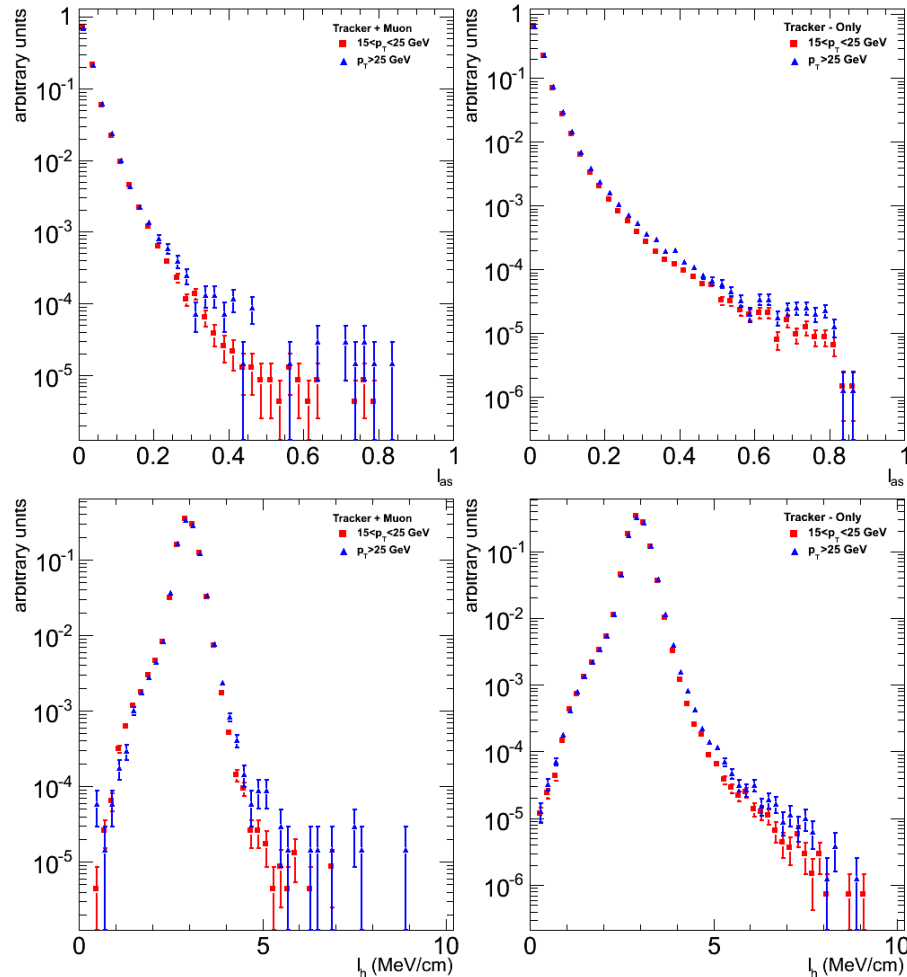


Figure 5.12: Measured  $I_{as}$  (top) and  $I_h$  (bottom) distributions for two momentum ranges for the Tracker+muon (left) and tracker-only (right) selections.

region  $A_i$ ,  $B_i$ ,  $C_i$  is negligible with respect to the number of background track in these three regions. This assumption is obviously correct which allows to estimate the number of background candidates in the signal region ( $D_i$ ).

In addition of the prediction of the absolute number of candidates in the region  $D_i$ , the method also allows to predict the shape of the mass distribution of the background candidates in the signal region. This requires a change of variables. Indeed, the mass can not be extracted from the  $(p_T, I_{as})$  pair, it is therefore necessary to use the  $(p, I_h)$  pair instead. The idea is the following: The shape of the mass distribution is nothing but the probability function for a background candidates falling in the signal region to have a mass  $m$ . This probability can be obtained by summing the probability of all the  $(p, I_h)$  pair corresponding to backgrounds of mass  $m$ . The  $p(I_h)$  distribution of background candidates in the region  $D_i$  is supposed to be strictly equal to the same distribution in the region  $B_i$  ( $C_i$ ) because of the un-correlation between  $p/p_T$  and  $dE/dx$ . Therefore, the probability for a background candidate to fall in a cell  $(p, I_h)$  of the region  $D_i$  is equal to the probability to fall in a cell  $(p)$  of the region  $B_i$ , times the probability to fall in a cell  $(I_h)$  of the region  $B_i$ .

$$P_{D_i}(m) = \sum_{M(p, I_h)=m} P_{D_i}(p, I_h) = \sum_{M(p, I_h)=m} P_{B_i}(p) \times P_{C_i}(I_h)$$

In order to have the final mass spectrum in the signal region, the mass probability function only needs to be rescaled by the expected total number of background candidates in that region:  $D_i = B_i C_i / A_i$ . Last but not least, the contributions of all the subsamples are summed in order to get the predicted mass distribution in the total signal region:  $D = \sum D_i$ .

The expected number of retained background events in the search region as predicted by the data-driven technique is computed as a function of the selection, which is defined by the two background efficiency values, common to all subsamples, obtainable with the  $p_T$  and the  $I_{as}$  selection alone, respectively. These background efficiency values are referred to as  $\epsilon_I$  and  $\epsilon_{p_T}$ , respectively.

The choice of the selection is, however, also driven by the knowledge of a possible systematic uncertainty on the background estimation. The systematic uncertainty on the expected background in the signal region is estimated by comparing observations and predictions in a control region of the mass spectrum that corresponds to masses smaller than  $75 \text{ GeV}/c^2$ , following the procedure outlined below. All possible different selections that provide at least 20 entries in the control region and a total expected background efficiency of at least  $10^{-2}$  are considered, where the total background efficiency is defined as the product of the efficiencies defining the selection. The possible selections satisfying the above criteria are shown on the Figure 5.13, the cell

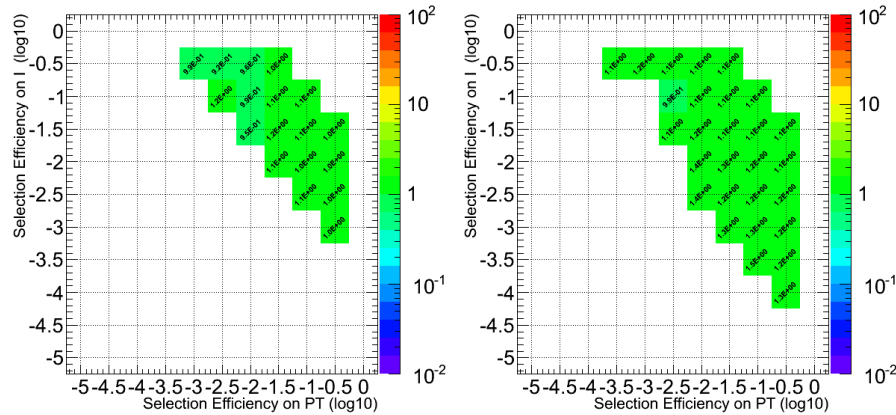


Figure 5.13: Ratio between the number of observed and predicted candidates in the control region defined in the text for different selections given by the  $x$  and  $y$ -axis coordinates. Only selections that provide 20 entries in the control region and that have a background efficiency lower than  $10^{-2}$  are considered.

color reflects the ratio between the number of observed and predicted candidates in the control region.

It turns out that for both the tracker-only and the tracker+muon selection the prediction systematically underestimates the observation. The average multiplicative factors that need to be applied to the prediction to match the observation are 1.19 and 1.04 for the tracker-only and tracker+muon selection, respectively. The observed discrepancies could be due to a residual correlation between momentum and  $dE/dx$ . For instance, the relativistic rise in the Bethe-Bloch model is not accounted for in the method adopted to estimate the background. Consequently, all predictions in the signal region are corrected by the scale factors indicated above. It was shown in section 3.3.3 that the "rise" effect is small but still present for particles with a momentum in the range from 15 GeV/c to 20 GeV/c. When sufficiently statistic will be available, only particles with momentum above 20 GeV/c should be used for the background prediction.

After correcting the prediction for these scale factors, the R.M.S. of the distribution of the prediction-to-observation ratio is 0.10 (0.06) for the tracker-only (muon-like) candidates. The relative systematic uncertainty on the corrected background prediction is assumed to be twice these R.M.S. values, the factor of two being a simple safety factor, given that the prediction in the signal region is the relevant quantity for both the choice of the selection and the final results. These uncertainties are much larger than the purely statistical uncertainties for the typical selections adopted in this analysis.

In both selections, the signal retention does not show a strong dependence on the selection for which 0.01 to 10 background events are expected, see Figure 5.8. An optimal selection is therefore one that retains an expected number of background events of the order of 0.1. This selection reduces the probability of having one background event in the search region without an excessive reduction of the signal yield. The ideal selection is chosen based on the information contained in the Figure 5.14. The figure is similar to Figure 5.10, but is different in two main points. First, the top part of the figure is showing the number of predicted candidates instead of the number of observed candidates as it was done before. Then, the color is reflecting the number of candidates falling in the signal region ( $D$ ) that have a mass above  $75 \text{ GeV}/c^2$ . The latter requirement was not used in the previous figure. The chosen selections are given in Table 5.2 and correspond to a remaining background level of about 0.1 events, after correction. A looser selection is also shown.

LOOSE	$\epsilon_{p_T}$	$p_T^{cut}$	$\epsilon_I$	$I_{as}^{cut}$
Tracker+muon	$10^{-1.5}$	43 - 73	$10^{-2.0}$	0.0653 - 0.3413
Tracker-only	$10^{-2.0}$	74 - 101	$10^{-2.5}$	0.0915 - 0.4984

TIGHT	$\epsilon_{p_T}$	$p_T^{cut}$	$\epsilon_I$	$I_{as}^{cut}$
Tracker+muon	$10^{-3.0}$	97 - 236	$10^{-3.0}$	0.0951 - 0.7691
Tracker-only	$10^{-3.0}$	110 - 228	$10^{-4.0}$	0.1836 - 0.8098

Table 5.2: Selections used in the analysis. The actual  $p_T$  and  $I_{as}$  thresholds depend on the subsample as explained in the text and are therefore expressed here as a range of values corresponding. The value of the threshold itself only depends on the required efficiency and on the statistic in the considered subsample. Top: loose selection. Bottom: full (tight) selection.

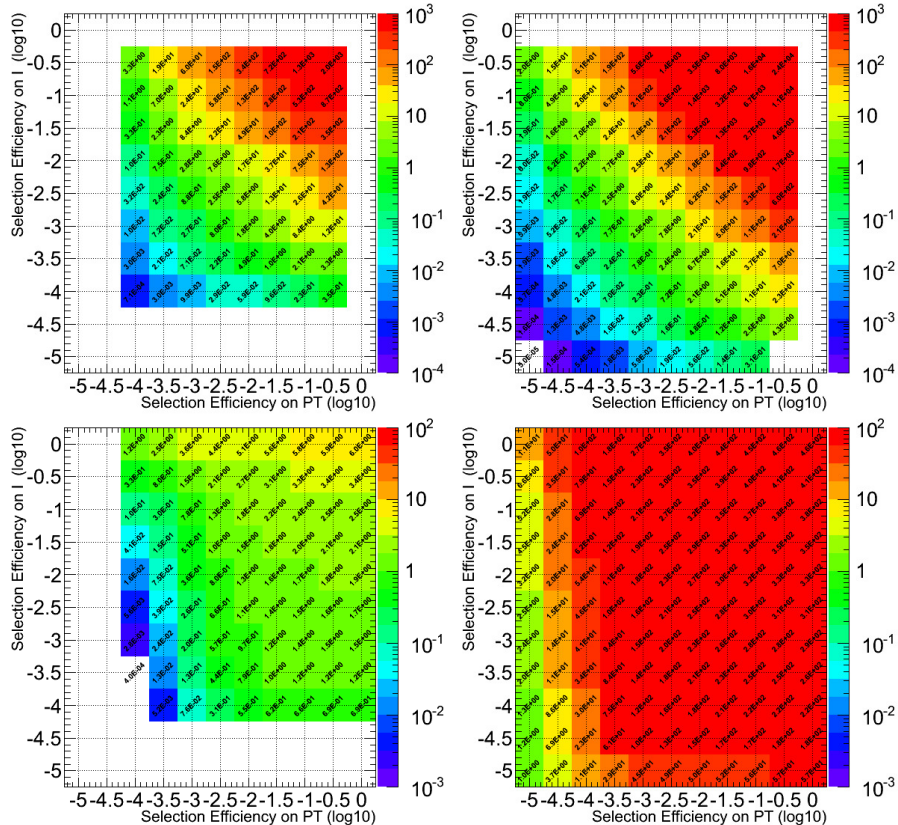


Figure 5.14: Predicted number of candidates after rescale for various selections on  $p_T$  and  $I_{as}$ . Top left (Top right) is the number of background candidates predicted for the tracker+muon selection (tracker-only selection). Bottom shows the expected number of  $100 \text{ GeV}/c^2 \tilde{\tau}_1$  signal using the tracker+muon selection (left) and the expected number of  $200 \text{ GeV}/c^2 \tilde{g}$  signal using the tracker-only selection. Only candidates with a reconstructed mass above  $75 \text{ GeV}/c^2$  are counted.

## 5.7 Results

The results of the HSCP search for the loose and tight selections are enumerated in the Table 5.3. No candidate HSCP track is observed in the search mass window in the case of the tight selection for both the tracker+muon and tracker-only analyses. The Figure 5.15 shows the resulting mass spectra using the loose selection and the corrected predictions. Despite a small underestimation of the prediction with respect to the observation and to the MC for the tracker+muon selection, also visible in Table 5.3, the agreement between MC, corrected data-driven prediction and data in both shape and absolute normalization is satisfactory. This underestimation is assumed to be coming from unlikely phenomena, that are not taken into account by the data-driven background prediction procedure, like bias of the  $dE/dx$  due to clusters affected by overlapping tracks, hard  $\delta$ -ray emission or nuclear interactions that have not been vetoed by the cluster cleaning algorithm. However, these phenomena seem to be well reproduced by the MC. Which indicates that the observed difference is not due to signal evidences.

The distribution of  $I_h$  versus  $p$  for all the candidates that pass the loose selection is shown on Figure 5.16. The properties of these candidates passing the loose selection and that have a mass above  $400 \text{ GeV}/c^2$  are listed in Table 5.4. All the candidates are in the forward region ( $|\eta| > 2.0$ ) and most of the tracker-only candidates are characterized by low  $I_{as}$  values that are just above the threshold applied in the corresponding subsample. Also, most of them have a relatively large error on their momentum, which may also explains their anomalously high reconstructed mass. At the exception of two candidates that have a significantly high energy loss, all the candidates have  $I_h$  values close to two  $4 \text{ MeV}/\text{cm}$ , which is just 1.4 times higher than the expected value for a MIP. The two candidates with a high energy loss ( $I_h > 5 \text{ MeV}/\text{cm}$ ) are candidates being in a forward jet environment, for which the  $dE/dx$  estimation is made out of clusters affected by overlapping tracks. A tighter tuning of the cluster cleaning algorithm would likely help to suppress these candidates, however the current tuning is already working relatively well since more than 50% of the clusters associated to the candidates are vetoed by the algorithm. Despite that this technique is not fully commissioned, it was checked that the time-of-flight of the tracker+muon candidates measured with the DT muon system is compatible with a muon. It is important to recall that these are candidates passing a loose selection. The main goal of this loose selection is to demonstrate the performance of the background prediction. It is in no manner a selection for the actual HSCP search that is performed with the tight selection.

LOOSE	E.S.	O.S.	E.F.S.	O.F.S.
Tracker+muon	$37 \pm 5$	47	$97 \pm 12$	110
Tracker-only	$62 \pm 13$	75	$81 \pm 17$	95

TIGHT	E.S.	O.S.	E.F.S.	O.F.S.
tracker+muon	$0.268 \pm 0.033$	0	$0.270 \pm 0.033$	0
Tracker-only	$0.227 \pm 0.047$	0	$0.227 \pm 0.047$	0

Table 5.3: Counting experiment results for the loose (top) and tight (bottom) selections. First two columns: corrected expected (E.S.) and observed (O.S.) number of events in the search region of the mass spectrum. Last two columns: corrected expected (E.F.S.) and observed (O.F.S.) number of events in the full mass spectrum.

tracker+muon	m (GeV/c <sup>2</sup> )	$p_T$ (GeV/c)	$I_{as}$	$I_h$ (MeV/cm)	#Hits
Candidate 1	732	$252 \pm 56$ ( 51)	0.19 (0.12)	3.81	16/ 9/2
Candidate 2	471	$141 \pm 33$ ( 49)	0.20 (0.09)	3.95	14/11/3

tracker-only	m (GeV/c <sup>2</sup> )	$p_T$ (GeV/c)	$I_{as}$	$I_h$ (MeV/cm)	#Hits
Candidate 1	629	$142 \pm 33$ (100)	0.68 (0.49)	6.27	14/ 3/1
Candidate 2	471	$141 \pm 33$ ( 87)	0.20 (0.18)	3.95	14/11/3
Candidate 3	419	$124 \pm 24$ (100)	0.50 (0.49)	5.41	12/ 4/0
Candidate 4	408	$110 \pm 24$ ( 87)	0.22 (0.18)	4.14	15/11/1
Candidate 5	400	$93 \pm 17$ ( 85)	0.21 (0.21)	4.13	17/10/0

Table 5.4: Properties of the candidates passing the loose selection and having a mass above 400 GeV/c<sup>2</sup>. The first column contains the reconstructed mass of the candidates. The second and third columns give the  $p_T$  and  $I_{as}$  of the candidates. The actual threshold applied on this variable for the candidate subsample is also shown in parenthesis. The fourth column gives the MP  $dE/dx$  of the candidates while the last column indicates, respectively, the number of tracking hits associated to the track, the number of SST clusters used for the  $dE/dx$  computation and the number of clusters affected by the saturation effect. The second candidate of the tracker+muon selection is actually the same as the second candidate of the tracker-only selection.

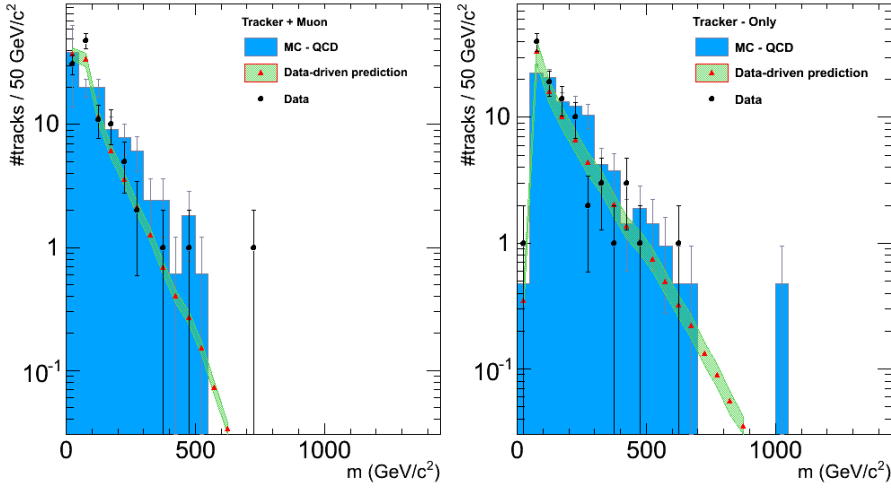


Figure 5.15: Mass spectra for the loose selection. Left: tracker+muon candidates. Right: tracker-only candidates. Observed spectrum (black dots), data-driven corrected predicted background spectrum (full red triangle) with its uncertainty (green band), MC background spectrum (blue histogram).

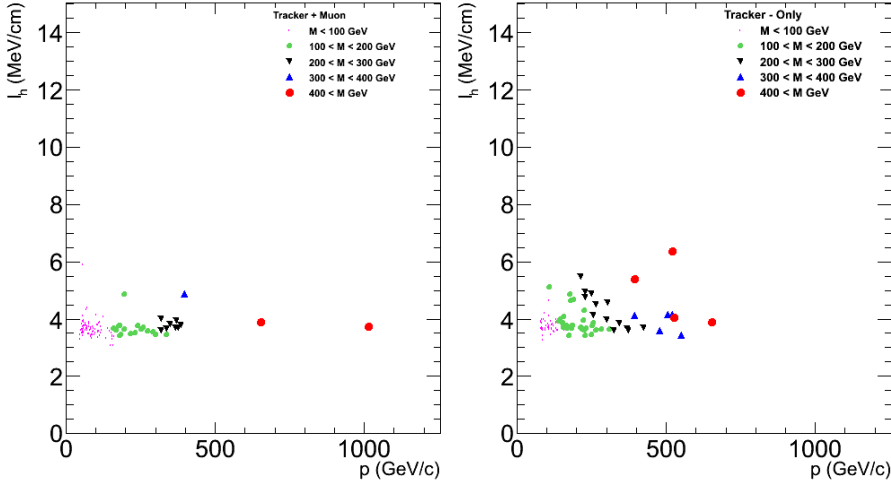


Figure 5.16: Distribution of the measured  $p$  and  $I_h$  for all candidates that pass the loose selection. Left: tracker+muon candidates. Right: tracker-only candidates.

Event displays of the events containing the two tracker+muon candidates are available on Figure 5.18 and Figure 5.17. In these two cases, it is clear that the candidate shows up in a (forward) region of high track multiplicity. The candidate directions coincides with a jet of momentum and transverse momentum greater than  $1000 \text{ GeV}/c$  and  $200 \text{ GeV}/c$  respectively. It is very clear that the SST clusters of that region are subject to overlapping tracks. It is therefore very likely that some of them have not been removed by the cluster cleaning algorithm and are biasing the  $dE/dx$  measurement. The track momentum measurement can also be biased towards higher value due to tracking hits coming from other tracks. It is also clear that the candidates are not real muon track (or even loosely identified as muon), these candidates pointing to muon activity induced by the leakage of the jet energy into the first layer of the muon system. All the high mass loose candidates have been checked one by one, they all have the same topology which is indeed a topology that does not satisfy the data-driven background prediction assumptions.

Given that no candidate is observed in the search mass window with the tight selection, 95% C.L. upper limits on HSCP production can be set. The acceptance for the signal is determined from MC and is given for the two selections in Table 5.5 and Table 5.6. The cross-section upper limits at 95% C.L. are computed with a full Bayesian method that uses a lognormal prior [59, 60] for integration over the nuisance parameters. Resulting cross-section limit curves are provided for the tracker+muon (traker-only) selection in Figure 5.19 (Figure 5.20), along with theoretical expectations for the production of staus, stops, and gluinos. The systematic uncertainties discussed in section 5.8 are already included in the cross-section upper limits reported in the previous tables and figures.

The stop and gluino cross-sections have been computed at NLO+NLL [74, 75, 76] by Anna Kulesza and Michael Krammer with the PROSPINO [77] software. The relative uncertainties on these cross-sections have also been computed by the same people and they are of the order of 15% as it is displayed on the figures as green bands. For stau, given that the observed limits are one order of magnitude above the theoretical expectation, the stau cross-sections have simply been computed at LO with PYTHIA which does not provide precise incertitudes for the computed cross-sections.

From the intersection of the cross-section limit curve obtained with the tracker+muon identification (tracker-only) selection and the lower edge of the gluino theoretical cross-section band, a lower limit at 95% C.L. on the mass of pair produced stable gluinos, hadronizing into R-gluonballs in 0%, 10% and 50% of the cases can respectively be set to  $419$  ( $403$ )  $\text{GeV}/c^2$ ,  $413$  ( $395$ )  $\text{GeV}/c^2$  and  $371$  ( $354$ )  $\text{GeV}/c^2$ . Similarly, lower limit at 95% C.L. on the mass of pair produced stable stops can be set to  $210$  ( $177$ )  $\text{GeV}/c^2$ .

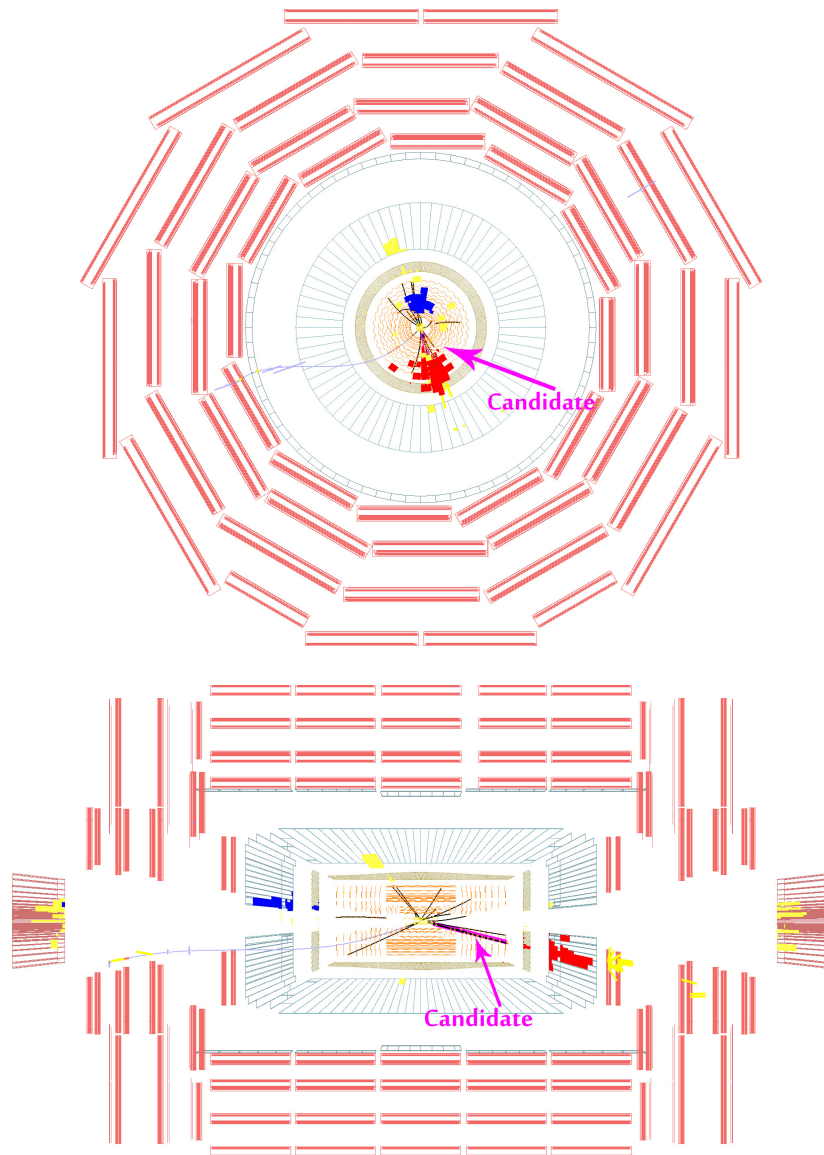


Figure 5.17: Transverse and longitudinal FROG views of the event (Run 143953 Lumi 192 Event 136389407) containing the loose candidate with a mass of  $731 \text{ GeV}/c^2$ . In this figure, the candidate track is shown in pink while the other tracks are shown in black. The two hardest jets in  $p_T$  of the event are shown in red ( $p_T = 239 \text{ GeV}/c$ ) and blue ( $p_T = 130 \text{ GeV}/c$ ), other jets are shown in yellow. The DT/CSC muon segments are displayed as thick yellow lines in the muon system and the RPC hits are displayed as light blue crosses.

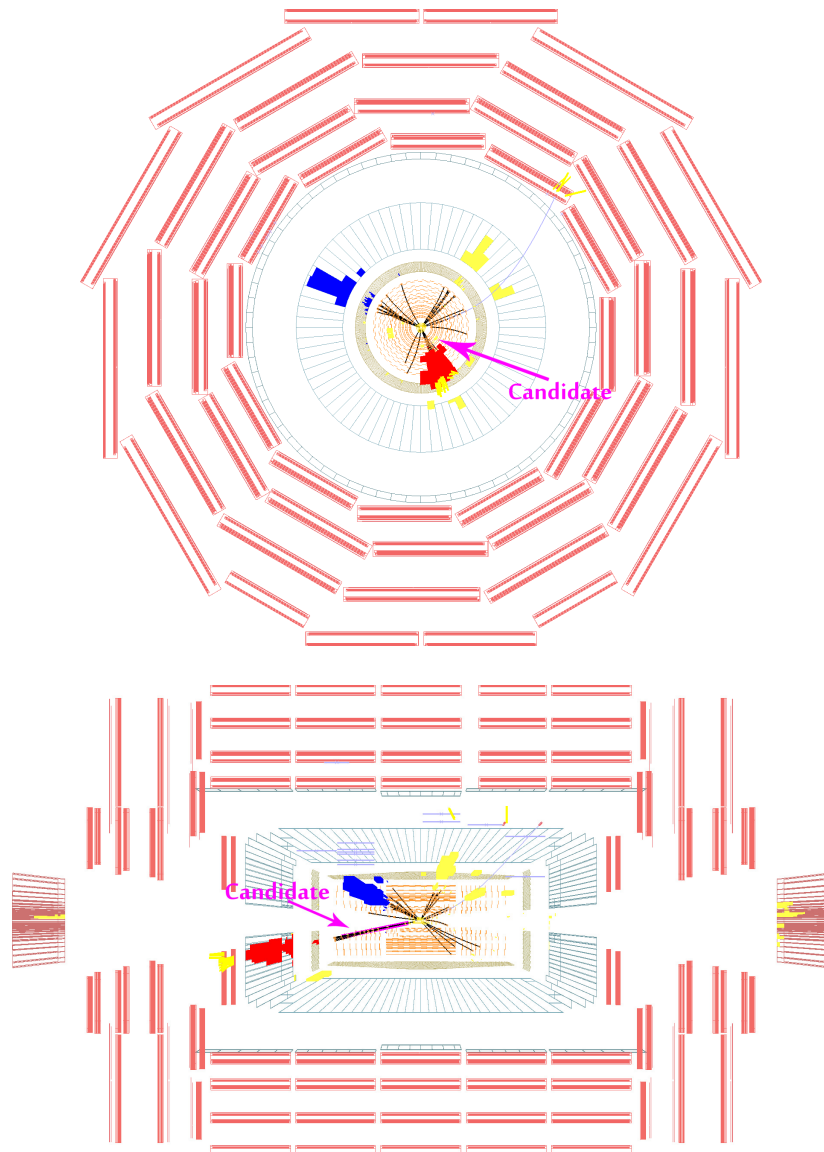


Figure 5.18: Transverse and longitudinal FROG views of the event (Run 140126 Lumi 192 Event 394929256) containing the loose candidate with a mass of  $471 \text{ GeV}/c^2$ . In this figure, the candidate track is shown in pink while the other tracks are shown in black. The two hardest jets in  $p_T$  of the event are shown in red ( $p_T = 319 \text{ GeV}/c$ ) and blue ( $p_T = 259 \text{ GeV}/c$ ), other jets are shown in yellow. The DT/CSC muon segments are displayed as thick yellow lines in the muon system and the RPC hits are displayed as light blue crosses.

The mass limits obtained using the tracker-only selection are lower basically because the optimal selection point is higher for this selection because the number of pre-selected tracks for this selection is by definition more important than for the tracker+muon selection. Therefore, in order to have the same amount of predicted background in the signal search window, the thresholds are necessarily higher and the selection tighter, which also slightly decrease the signal selection efficiency. Also, the candidates for this selection are generally made of worst quality tracks.

As discussed already, the main goal of the tracker-only selection is to search R-hadron signals that are becoming neutral before reaching the muon station. Such signals are simply not detectable by the tracker+muon selection. But the tracker-only selection allows to set limits on such models. The acceptances for such signals have been determined from the pessimistic MC samples in which the nuclear interactions of the R-hadrons with matter always make the R-hadrons neutral via the charge-flipping mechanism. For such models, lower limits on the mass of pair produced stable gluinos, hadronizing into R-gluonballs in 0%, 10% and 50% of the cases can respectively be set to  $333 \text{ GeV}/c^2$ ,  $325 \text{ GeV}/c^2$  and  $265 \text{ GeV}/c^2$ . No limit on the mass of pair produced stable stops can be computed under the hypothesis of nuclear interactions leading to the suppression of the stop R-hadron charge. This is a consequence of the very low acceptance of light stops signal, which is itself due to a three times lower trigger efficiency with respect to the stop model without charge suppression but also due to a significantly lower track reconstruction efficiency. The signal acceptance and cross-section upper limit for the pessimistic interaction models case can be found in Table 5.6, and resulting cross-section limit curves are visible in Figure 5.21.

gluino mass ( $\text{GeV}/c^2$ )	200	300	400	500	600	900
Theoretical cross section (pb)	606	57.2	8.98	1.87	0.470	0.0130
Tracker+muon; f=0.0						
Total acceptance (%)	9.57	14.06	18.30	21.68	22.39	22.85
Expected 95% C.L. limit (pb)	12.34	8.40	6.45	5.45	5.28	5.17
Observed 95% C.L. limit (pb)	10.84	7.38	5.67	4.79	4.64	4.54
Tracker+muon; f=0.1						
Total acceptance (%)	8.54	12.45	16.29	19.35	20.15	20.41
Expected 95% C.L. limit (pb)	13.83	9.49	7.25	6.10	5.86	5.79
Observed 95% C.L. limit (pb)	12.15	8.34	6.37	5.36	5.15	5.08
Tracker+muon; f=0.5						
Total acceptance (%)	4.63	6.68	8.78	10.55	11.24	11.13
Expected 95% C.L. limit (pb)	25.52	17.69	13.46	11.20	10.52	10.62
Observed 95% C.L. limit (pb)	22.41	15.55	11.82	9.84	9.24	9.33
stop mass ( $\text{GeV}/c^2$ )	130	200	300	500	800	
Theoretical cross section (pb)	120	13.0	1.31	0.0480	0.0011	
Tracker+muon						
Total acceptance (%)	4.22	11.22	17.40	25.07	26.30	
Expected 95% C.L. limit (pb)	27.96	10.52	6.79	4.71	4.49	
Observed 95% C.L. limit (pb)	24.56	9.24	5.97	4.14	3.95	
stau mass ( $\text{GeV}/c^2$ )	100	126	156	200	247	308
Theoretical cross section (pb)	1.33	0.330	0.105	0.0250	0.0080	0.0020
Tracker+muon						
Total acceptance (%)	4.99	14.23	27.55	47.85	63.03	79.34
Expected 95% C.L. limit (pb)	23.68	8.30	4.29	2.47	1.87	1.49
Observed 95% C.L. limit (pb)	20.80	7.29	3.76	2.17	1.65	1.31

Table 5.5: Acceptances and cross-section upper limit for the different models considered in which R-hadron charge is not suppressed. The tracker+muon selection is used. The systematic uncertainty is already incorporated in the quoted limits.

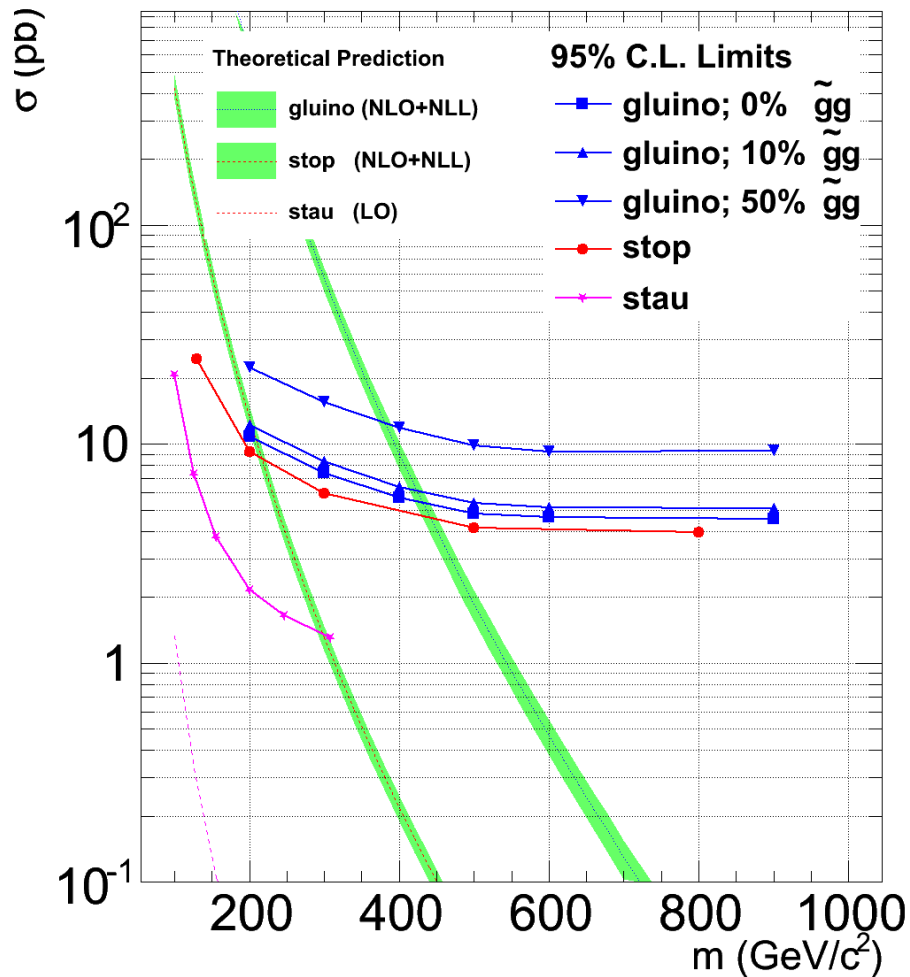


Figure 5.19: Observed, for the tracker+muon selection, 95% C.L. upper limits on the cross-section for production of the different models considered (in which R-hadron charge is not suppressed) and predicted theoretical cross-sections. The bands represent the theoretical uncertainty on the cross-section values. The systematic uncertainty is already incorporated in the limits shown on the figure.

gluino mass ( $\text{GeV}/c^2$ )	200	300	400	500	600	900
Theoretical cross section (pb)	606	57.2	8.98	1.87	0.470	0.0130
Tracker-only; f=0.0						
Total acceptance (%)	7.50	10.77	14.16	17.61	18.25	19.73
Expected 95% C.L. limit (pb)	15.45	10.76	8.19	6.58	6.35	5.88
Observed 95% C.L. limit (pb)	13.83	9.63	7.33	5.89	5.68	5.26
Tracker-only; f=0.1						
Total acceptance (%)	6.66	9.54	12.59	15.71	16.45	17.59
Expected 95% C.L. limit (pb)	17.40	12.16	9.21	7.38	7.05	6.59
Observed 95% C.L. limit (pb)	15.57	10.88	8.24	6.60	6.31	5.90
Tracker-only; f=0.5						
Total acceptance (%)	3.54	5.10	6.75	8.53	9.23	9.50
Expected 95% C.L. limit (pb)	32.79	22.73	17.17	13.60	12.57	12.21
Observed 95% C.L. limit (pb)	29.35	20.34	15.37	12.17	11.25	10.93
stop mass ( $\text{GeV}/c^2$ )	130	200	300	500	800	
Theoretical cross section (pb)	120	13.0	1.31	0.0480	0.0011	
Tracker-only						
Total acceptance (%)	2.28	9.13	14.74	22.24	25.53	
Expected 95% C.L. limit (pb)	50.98	12.70	7.87	5.21	4.54	
Observed 95% C.L. limit (pb)	45.63	11.37	7.04	4.67	4.06	
stau mass ( $\text{GeV}/c^2$ )	100	126	156	200	247	308
Theoretical cross section (pb)	1.33	0.330	0.105	0.0250	0.0080	0.0020
Tracker-only						
Total acceptance (%)	1.10	6.67	16.91	34.15	46.82	57.91
Expected 95% C.L. limit (pb)	105.16	17.37	6.86	3.39	2.48	2.00
Observed 95% C.L. limit (pb)	94.12	15.55	6.14	3.04	2.22	1.79

Table 5.6: Acceptances and cross-section upper limit for the different models considered in which R-hadron charge is not suppressed. The tracker-only selection is used. The systematic uncertainty is already incorporated in the quoted limits.

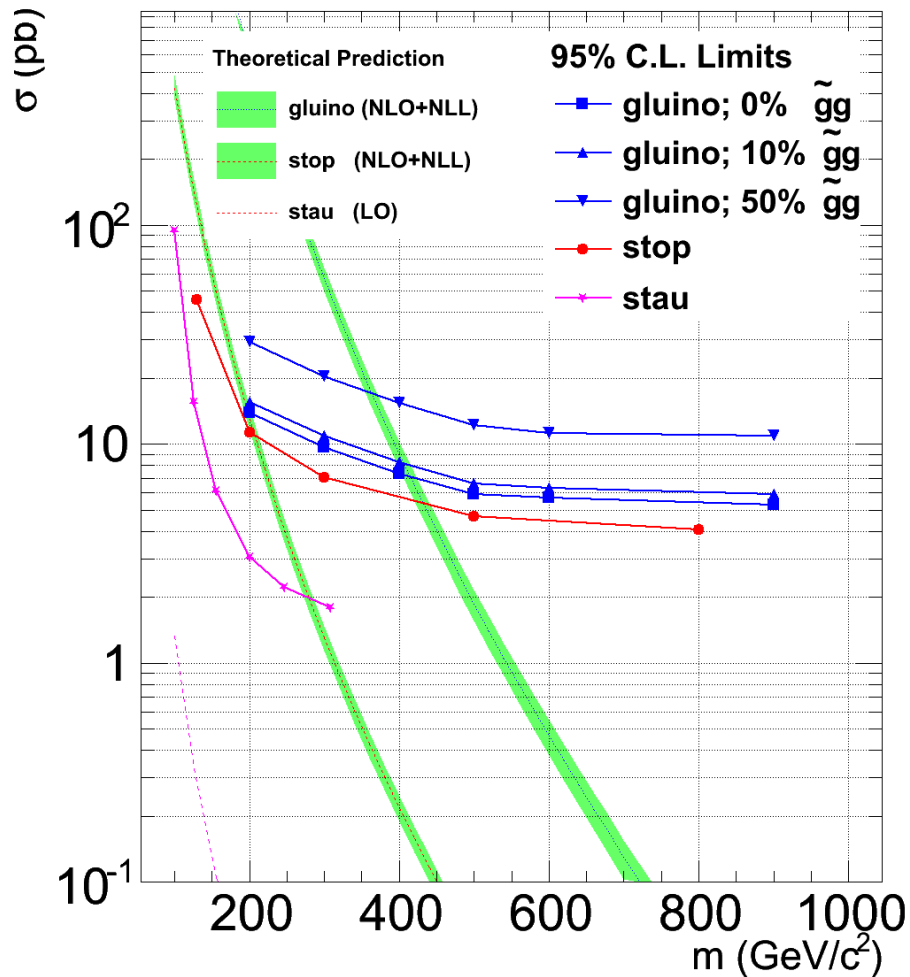


Figure 5.20: Observed, for the tracker-only selection, 95% C.L. upper limits on the cross-section for production of the different models considered (in which R-hadron charge is not suppressed) and predicted theoretical cross-sections. The bands represent the theoretical uncertainty on the cross-section values. The systematic uncertainty is already incorporated in the limits shown on the figure.

gluino mass ( $\text{GeV}/c^2$ )	200	300	400	500	600	900
Theoretical cross section (pb)	606	57.2	8.98	1.87	0.470	0.0130
Tracker-only; f=0.0; ch. suppr.						
Total acceptance (%)	1.10	3.48	5.52	8.79	12.74	16.51
Expected 95% C.L. limit (pb)	105.86	33.34	21.00	13.19	9.10	7.02
Observed 95% C.L. limit (pb)	94.73	29.83	18.80	11.81	8.14	6.28
Tracker-only; f=0.1; ch. suppr.						
Total acceptance (%)	0.99	3.08	4.93	7.81	11.42	14.80
Expected 95% C.L. limit (pb)	117.16	37.65	23.52	14.85	10.15	7.84
Observed 95% C.L. limit (pb)	104.88	33.69	21.04	13.30	9.08	7.01
Tracker-only; f=0.5; ch. suppr.						
Total acceptance (%)	0.55	1.61	2.64	4.12	6.19	8.02
Expected 95% C.L. limit (pb)	210.29	72.23	43.92	28.16	18.73	14.46
Observed 95% C.L. limit (pb)	188.23	64.65	39.31	25.20	16.77	12.94
stop mass ( $\text{GeV}/c^2$ )	130	200	300	500	800	
Theoretical cross section (pb)	120	13.0	1.31	0.0480	0.0011	
Tracker-only; ch. suppr.						
Total acceptance (%)	0.17	1.89	4.52	8.93	13.19	
Expected 95% C.L. limit (pb)	680.95	61.31	25.64	13.00	8.79	
Observed 95% C.L. limit (pb)	609.38	54.86	22.95	11.63	7.87	

Table 5.7: Acceptances and cross-section upper limit for the different models considered in which R-hadron charge is suppressed. The tracker-only selection is used. The systematic uncertainty is already incorporated in the quoted limits.

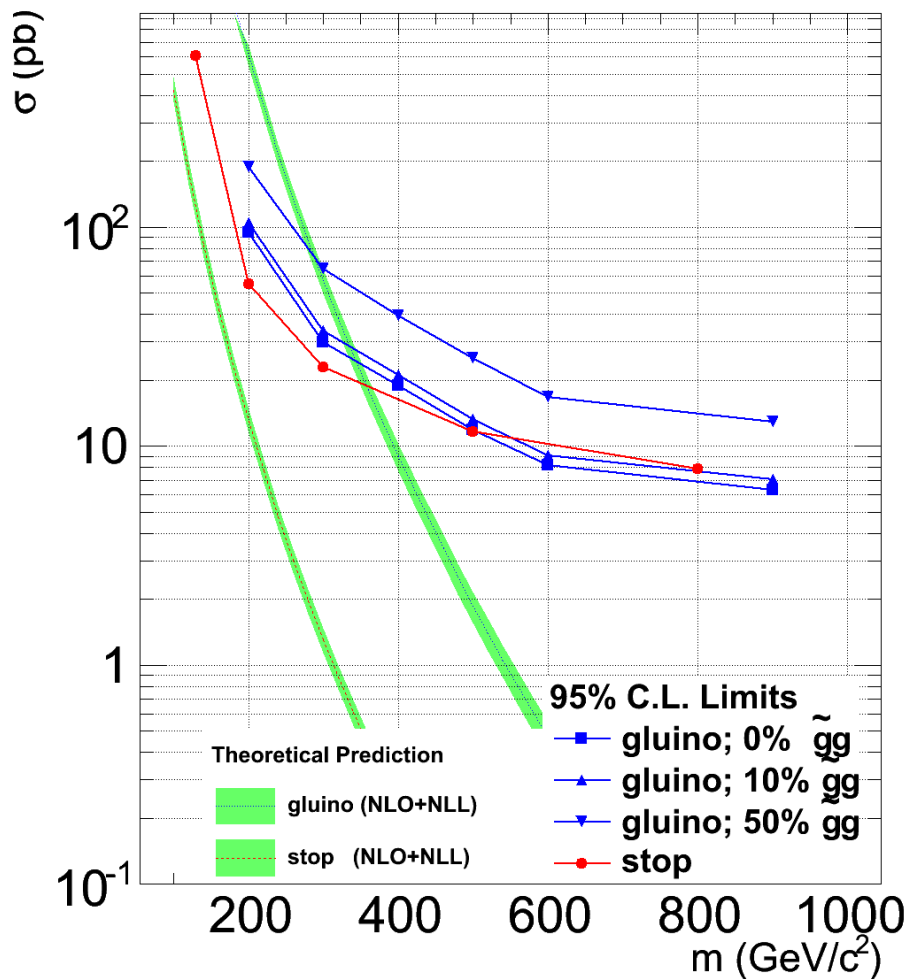


Figure 5.21: Observed, for the tracker-only selection, 95% C.L. upper limits on the cross-section for production of the different models considered (in which R-hadron charge is suppressed) and predicted theoretical cross-sections. The bands represent the theoretical uncertainty on the cross-section values. The systematic uncertainty is already incorporated in the limits shown on the figure.

## 5.8 Systematic Uncertainties

The main sources of systematic uncertainties on the cross-section upper limit and mass lower limit results, summarized in Table 5.8, are the following:

- Uncertainty on the signal acceptance. A value of 15% is assumed. It derives from the following contributions:
  - Uncertainty on the trigger efficiency is obtained from MC. The uncertainty on the jet and  $E_T^{\ell}$  trigger efficiency is expected to be dominated by the uncertainty of 10% on the jet energy scale [78]. Varying by  $\pm 10\%$  the threshold on the single jet ( $E_t^{miss}$ ) trigger resulted in a change in the corresponding trigger efficiency by < 10% for all considered signals. A disagreement of up to 10% is observed between the single muon trigger efficiency in data and MC at all energies [72]. In addition, for this specific analysis, it is expected that a further uncertainty may arise as a result of the delayed arrival of HSCPs in the muon system. Assuming a drop in the muon trigger efficiency by 15%, it was verified that the drop in the overall trigger efficiency is less than 5% for all considered signals. On the basis of these numbers, an uncertainty of 10% on the overall trigger efficiency was assumed.
  - Uncertainty on offline track (< 5%) [79] and muon (5%) [72] reconstruction efficiency.
  - Uncertainty on the track momentum scale (< 5% [79]) and  $dE/dx$  scale. The latter is estimated to be less than 5% from the level of agreement observed between data and MC for low momentum hadrons ([58] and Figure 4.6). It was verified that even a change by 5% in the momentum scale implies a less than 5% change in the signal acceptance. For the case of  $dE/dx$  the resulting variation, for the same relative change, is less than 3% for  $\tilde{t}_1$  and  $\tilde{g}$  and increases to 8% at 100 GeV/c<sup>2</sup> in the case of the  $\tilde{\tau}_1$ .
- Uncertainty on the absolute value of the integrated luminosity is assumed to be 11% [80].
- Uncertainty on the expected background. This contribution was discussed in Section 5.6 and is estimated to be 20% (12%) for the tracker-only (tracker+muon identification) analysis. This uncertainty has, however, a very minor impact on the cross-section upper limits for the case at hand of non-observed event.

Source of Systematic Error	Relative Uncertainty (%)
Expected background	20(Tk-Only) ; 12 (Tk+Mu)
Integrated luminosity	11
Trigger efficiency	10
Muon reconstruction efficiency	5
Track reconstruction efficiency	< 5
Momentum scale	< 5
Ionization energy loss scale	< 3 (8 for $100 \text{ GeV}/c^2 \tilde{\tau}_1$ )
Total uncertainty on signal acceptance	15

Table 5.8: Sources of systematic errors and corresponding relative uncertainties.

## 5.9 Perspectives

The strategy for updating results with additional data is to keep the background level constant at about  $10^{-1}$  expected background events by tightening the selection. For the selection that requires muon identification, this choice appears to be optimal certainly up to  $100 \text{ pb}^{-1}$ . For the selection based only on the inner tracker data, this limit is at  $\sim 10\text{-}20 \text{ pb}^{-1}$ . However, some adaptation will be needed before this limit in order to keep a significantly high signal acceptance for light ( $m < \sim 250 \text{ GeV}/c^2$ ) HSCPs. These adaptations need to be studied but can consist of small improvements in the candidate pre-selections. Adding an isolation requirement is expected to slightly improve the situation.

After these limits, two parallel strategies could and will be used:

1. For the lepton-like or for the R-hadrons appearing charged in the muon chambers, the time-of-flight measured by the muon system or even by the electromagnetic calorimeter will be used to strongly suppress the MIP background. Indeed, the time-of-flight measurement is completely uncorrelated to the track  $dE/dx$  and momentum measurements for MIP particles, but are obviously correlated for the HSCP signal. The current search strategy can easily be extended to this third measurement: optimized selection depending on track quality is expected to stay advantageous. The data-driven background prediction can be generalized to a third un-correlated measurement as well.
2. For the R-hadrons search with charge suppression, due to nuclear interaction of the HSCP with the detector material, a tracker-only selection is still needed since muon identification will not be possible. The idea is therefore to replace the simple counting experiment by a likelihood method making maximal use

of the data driven background prediction. Currently only the absolute number of background in the mass region [75,2000]  $\text{GeV}/c^2$  is used. In the future, the prediction of the background shape in the mass distribution may also be used by peak-search algorithms. This last method was successfully tested on MC data [73].

Upper limits on the stop production cross-section are expected to be quickly stronger than the actual limits set by Tevatron experiments. Few more  $\text{pb}^{-1}$  are expected to be enough to exclude stops below 250  $\text{GeV}/c^2$ . Since no exclusion on the gluino production cross-section has ever been published, the limits obtained by this analysis are already the reference limits, however, despite the fact that no Tevatron experiment sets limits on the gluino masses, it was estimated that they could have only been able to exclude gluino masses below  $\sim 350 \text{ GeV}/c^2$ . About  $\sim 100 \text{ pb}^{-1}$  will be needed to improve the exclusion on stau production cross-section and more generally on lepton-like HSCPs.

## 5.10 Conclusion

The search for Heavy Stable (or long-lived) Charged Particles presented in this chapter is one of the first analysis, exploiting LHC collisions at  $\sqrt{s} = 7 \text{ TeV}$ , that performed a complete search for BSM physics. It was shown to already give competitive results with just  $3.06 \text{ pb}^{-1}$  of data. Cross-section upper limits were set for various HSCP models, including models that were never considered by other experiments so far, in which the R-hadron charge is suppressed due to the charge flipping mechanism. Lower limits on the mass of split SUSY gluino hadronizing into R-gluonballs in 10% of the cases have been fixed at  $413 \text{ GeV}/c^2$ . Similar limits for pair produced top squarks are set to  $210 \text{ GeV}/c^2$ . These limits are computed at 95% C.L. using a  $dE/dx$  and track+muon identification selection.

In the case where charge flipping of the R-hadron induces a charge suppression in the muon system, a  $dE/dx$ -only selection has to be used instead of the tracker+muon selection. In the latter case, the mass lower limit for pair produced gluinos become  $325 \text{ GeV}/c^2$ .

Some information on the perspective of the analysis were also given. The analysis can remain unchanged up to  $\sim 10\text{-}20 \text{ pb}^{-1}$  and after that two possibilities of upgrade were discussed: muon time-of-flight may be used to keep the background to a null level or the counting experiment search can be replaced by a peak search using a likelihood method.

# Conclusion

The final results presented in this document are obtained with an integrated luminosity of  $3.06 \text{ pb}^{-1}$ . This amount of data comes from the very first months of LHC data taking. This search of Heavy Stable (or long lived) Charged Particles (HSCP) is one of the first Beyond the Standard Model searches performed at the LHC. This search, in addition of improving the current limits of few HSCP models, validates the HSCP analysis workflow that was prepared for the last three years. These preparations included the development of all tools needed to analyze the very first LHC data. The most important developments needed for this search are the silicon strip tracker calibration and the  $dE/dx$  based particle identification that are both mandatory for this early HSCP search.

An efficient Silicon Strip inter-calibration was developed. Contrary to the original calibration method that uses an electronic signal for the calibration, this new method is using minimum ionizing particles to equalize the response of the silicon strip tracker chips. The latter calibration procedure was commissioned for years on simulated and cosmic muon ray data and was therefore ready to be used on the very first collision data of the LHC.

Powerful tools for particle identification based on the particle ionization energy loss were developed. These tools consist at a set of MP  $dE/dx$  estimators and  $dE/dx$  discriminators that have been validated on 900 GeV collision data. The firsts have shown to be precious for  $dE/dx$  based mass reconstruction, while the seconds have shown to be optimal for HSCP identification. The bias induced by the electronic cut-off at 254 ADC counts of the strip charge was also estimated and it was shown that it is not too problematic for a counting experiment based HSCP search. Finally, a cluster cleaning algorithm was presented. It allows to improve the signal-to-noise ratio for the HSCP search by discarding number of clusters, affected by overlapping tracks, nuclear interactions or hard  $\delta$ -rays.

The presented search used inner tracker tracks with a high ionization energy loss and with a high- $p_T$  to select HSCP candidates. The search was repeated with a second selection that requires, in addition, the tracks to be pointing toward activities in the CMS muon system. This second selection aimed to detect highly penetrating HSCPs that remain charged up to the muon system. For both selections, the observed mass distribution, reconstructed using the track MP  $dE/dx$  and momentum, is consistent with the expected background from MIPs.

From this result, obtained with  $3.06 \text{ pb}^{-1}$  of integrated luminosity, a lower limit at 95% C.L. on the production mass of pair produced stable gluinos, hadronizing into R-gluonballs in 10% of the cases, was set at  $413 \text{ GeV}/c^2$ . Similar limit for pair produced top squarks was set at  $210 \text{ GeV}/c^2$ . The cross-section upper limits at 95% C.L. for both pair produced stops and gluinos have been fixed below  $\sim 20\text{pb}$ . Cross-section upper limits for the production of stable staus, in the framework of the mGMSB model, have similarly been fixed below  $\sim 20\text{pb}$ . This analysis is the first to set cross-section and mass limits on pair produced gluinos. The CDF experiment already excluded stop masses below  $249 \text{ GeV}/c^2$  and this analysis is therefore confirming this statement up to  $210 \text{ GeV}/c^2$ . Similar results have been obtained under the assumption that the nuclear interactions of charged R-hadrons with matters always make the particles becoming neutral via the charge flipping mechanism. If the latter hypothesis, considered for the first time by an experimental search, reveals to be true, the HSCP R-hadrons would be reaching the muon system as neutral particle. The selection not exploiting the muon signature was therefore used to set limits for such models. The lower limits at 95% C.L. on the mass of pair produced gluinos ( $\tilde{g}g = 10\%$ ) have been fixed to  $325 \text{ GeV}/c^2$ .

A visualization tool, FROG, was developed to solve some of the problems affecting the official CMS event display tool. It was shown to be a good compromise between execution speed and displayable level of details. Moreover, the tool is completely generic and independent of the experiment framework which allows FROG to be used by many physics collaboration including: CMS, TOTEM, ILD, GASTOF and DELPHES. In the CMS experiment, FROG was intensively used for the commissioning of the detector and outreach purposes, including the production of official animations of the first  $pp$  collisions in CMS at  $\sqrt{s} = 7 \text{ TeV}$ . These animations encountered a large success on the web.

Finally, given that CMS is expected to collect few  $\text{fb}^{-1}$  before the end of 2011, stronger limits on the HSCP production cross-sections and allowed mass will certainly appear in a very close future.

# Appendices



# Appendix A

## FROG Visualization Software

The tool presented here, the Fast and Realistic OpenGL event displayer [40] (FROG), was used at many occasions along the thesis work. This tool was developed because the available CMS visualization tools were not satisfactory on many points. The ability to precisely display the event information and to inspect the reconstructed objects and detector geometry is crucial at the early stage of a complex high energy physics experiment.

This appendix describes some technicalities of FROG: The FROG File Format (FFF) is described in more detail in Section A.1. The two parts of the code, the Producer and the Displayer, are described respectively in Section A.2 and A.3. Additional features are described in Section A.4. A few applications of FROG in specific detector setups/environments are given in Section A.5. A more complete description of the implementation can be found in [40].

The FROG library allows to display and store more than 32 primitive objects, each of them is defined in a unique C++ class. Each object, and therefore class, inherits from one unique main class called `FROG_Element_Base`. The Figure A.1 is the class diagram of all the standard displayable objects. This base class contains several methods used to read/write data from/to file and to optimize the performance of the object display itself. These classes are used both by the Displayer and the Producer. The Figure A.2 shows the diagram of the classes that are mainly used by the Displayer. Many of these are actually coding the FROG Graphical User Interface (GUI), or the objects, cameras, views and fonts properties.

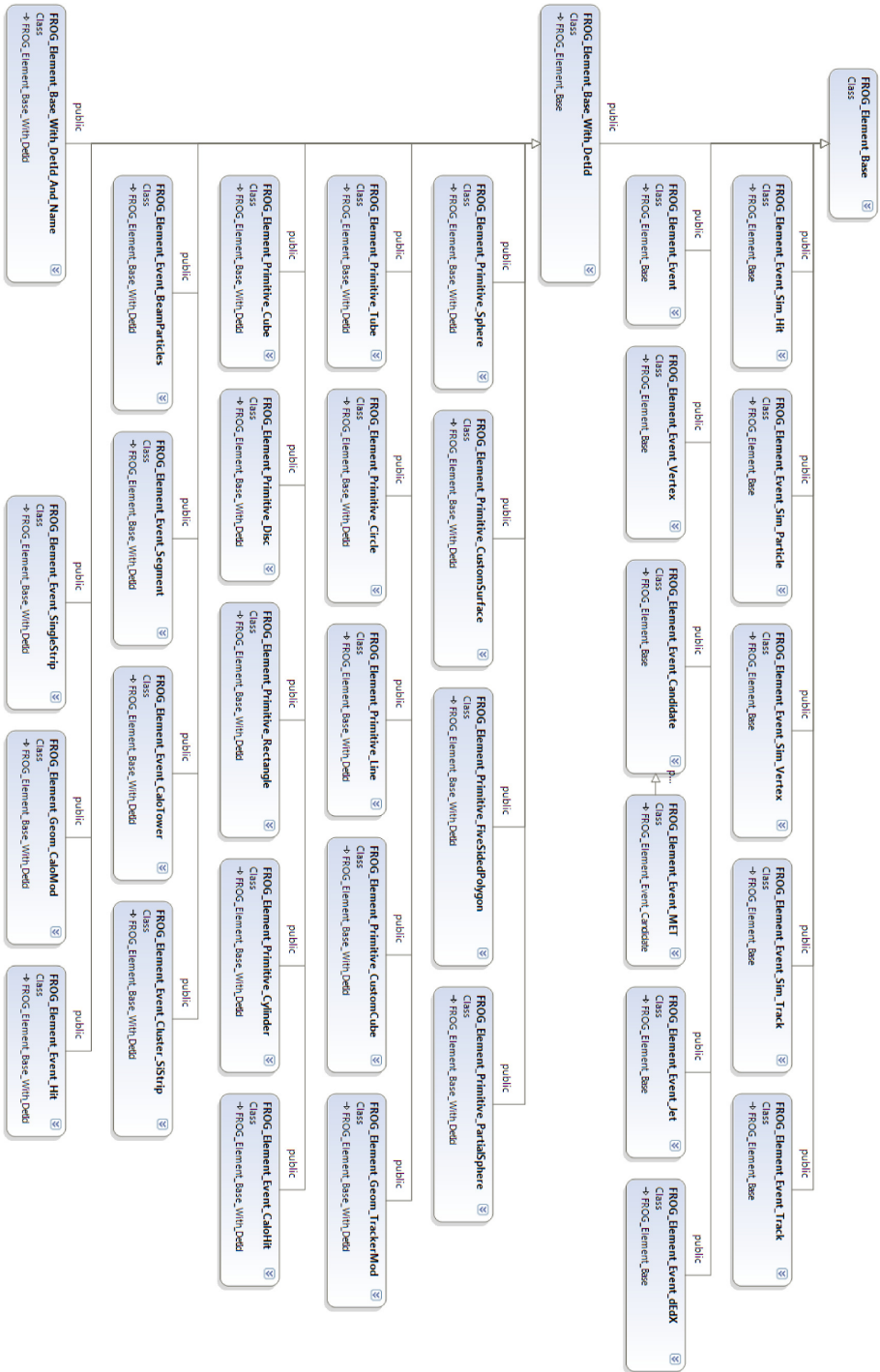


Figure A.1: Schematic view of the FROG architecture. All displayable objects inherit from a main base class.

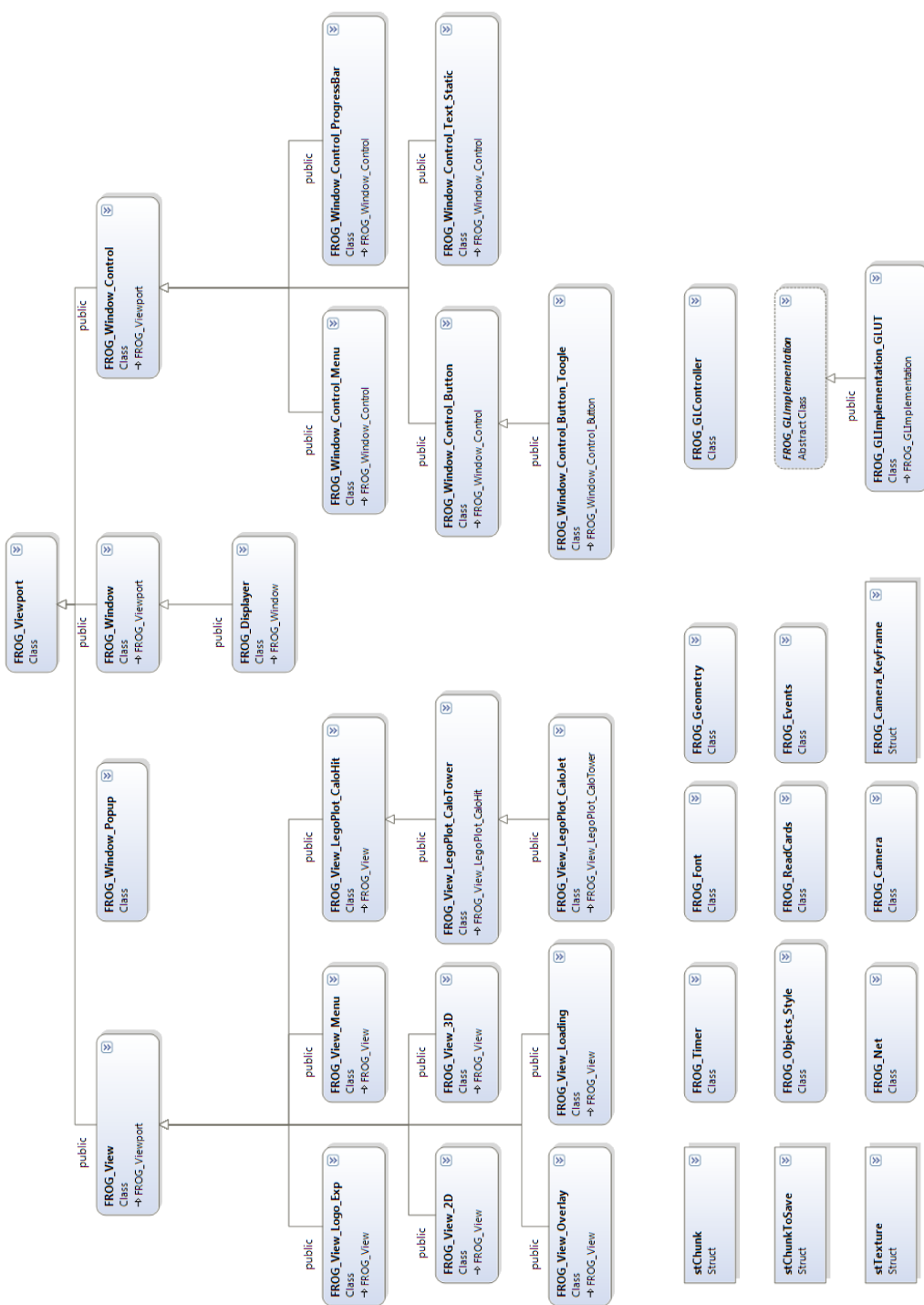


Figure A.2: Schematic view of the FROG class diagram. The upper half of the picture describes the classes coding the FROG GUI.

## A.1 FROG File Format

The FROG File Format (FFF) is of crucial importance and has a significant impact on the program structure. Since FROG has to be completely generic and has to store needed data in the most compact way, the dedicated file format is based on a binary encoding, where data are organized in *chunks*. Each chunk contains an *Id* that specifies the chunk type, a *Size* that indicates the chunk end, and the *Data* themselves. The chunk *Id* is written on 2 Bytes, so  $2^{16} = 65\,536$  different chunk types can be handled. The *Size* is written on 4 Bytes, so the chunk size is limited to  $2^{32} = 4$  GBytes. The *Size* is defined as :

$$\text{Size} = \text{sizeof}(Id) + \text{sizeof}(Size) + \text{sizeof}(Data) = 6 + \text{sizeof}(Data)$$

The chunks can contain any type of data, which ensures a maximal flexibility to the software. They can be divided into two categories : chunks that contain sub-chunks and those that do not. By similarity with trees, the firsts are called "branches" while the others are called "leaves". The branches are useful to group together all data of a same experiment/detector/region. See Figure A.3.

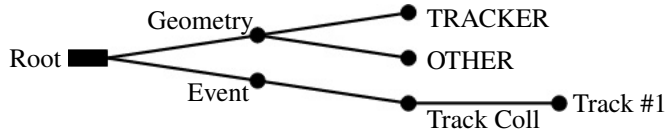


Figure A.3: A schematic view of the tree structure of a FFF.

A file always contains a unique primary chunk that encapsulates, in its *Data* part, all the other chunks, it is the root of the data tree. It must be of type C\_PRIMARY=55555. When the primary chunk *Size* is not equal to the file size, the file is assumed to be corrupted. The experiment data (e.g. the detector geometry or the event signals) are contained in the sub-chunks of this primary chunk. The chunk structure is illustrated in Figure A.4.

It is often possible to optimize the way data are stored. For instance, if a large number of data of the same type and the same size are stored (e.g. 100 Int32) in a mother chunk, it is clear that it is only needed to define the size and the type once for all the data. This optimized chunk is represented on Figure A.5. The best storing method is automatically chosen by FROG in order to reduce the file size. The definition of the chunk structure and the related methods can be found in the files:

Data of the Primary Chunk						
Id		Size		Data		
55555	16 = 2+4 + 10+10	01=Int32  2+4+4	10 =	Int32	02=Float  2+4+4	10 =
						Float

Figure A.4: Example of a FROG file data structure. The primary chunk contains two sub-chunks storing an integer and a float.

FROG/FROG\_Chunk.cpp and FROG/FROG\_Chunk.h files.

<b>Id</b>	<b>Size</b>	<b>Data</b>							
01=Int32	106 = 2+4 + 100*4	Int32	Int32	Int32	Int32	...	...	...	Int32

Figure A.5: Example of the chunk structure if the file contains 100 Int32.

## A.2 FROG Producer

The FROG Producer builds the Events and the Geometry of a particular detector and stores them into `.vis` and `.geom` files. It is the interface between the detector software<sup>1</sup> and FROG. A FROG Producer already exists for the CMSSW environment. The Producer is the only part of FROG that has to be interfaced to the user needs, to the experiment software and to the data format.

The Producer is in general a part of code (generally C++) that converts the experiment data format to the FFF. Since the Producer does not use specific graphical libraries, it can be run in parallel on a computer cluster. The many output .vis files can be merged in a unique file using the FROG merger included in the FROG package. This tool is extremely fast since it just puts the event chunks spread into many files, in the same primary chunk of a unique file.

<sup>1</sup>Two examples of detector softwares are CMSSW in the CMS experiment and Athena in the ATLAS experiment.

The experiment software only needs to include the FROG classes definition in order to produce the `.vis` and `.geom`. This reduced FROG package, containing only the class definition, takes of the order of  $\sim 0.5\text{MB}$  on disk and is freely distributable.

### A.3 FROG Displayer

This part of the code is completely independent of the detector and does not need to be modified by the FROG users. The code uses extensively the OpenGL library and is programmed in a way to keep the quick rendering of events.

All the style parameters are loaded from the configuration file (`config.txt`). The geometry and the current event are displayed in the different 3D/2D views. The display of the first frame can be slow, but then, thanks to the OpenGL Display Lists, the Displayer can render more than 60 frames per second.

Another technique is used to make the display faster for secondary views : after the first draw, an internal screenshot of the view is taken, then, this screenshot is just used to redraw the view. From time to time the screenshot is updated. However the main view does not use this technique. The mouse clicks are handled in order to outline (flashing) and print out information of the mouse selected object.

The Figure A.6 shows a screenshot of the FROG Displayer running an event in the fictitious tracking experiment defined in the FROG tutorial and detailed in the appendix of [40].

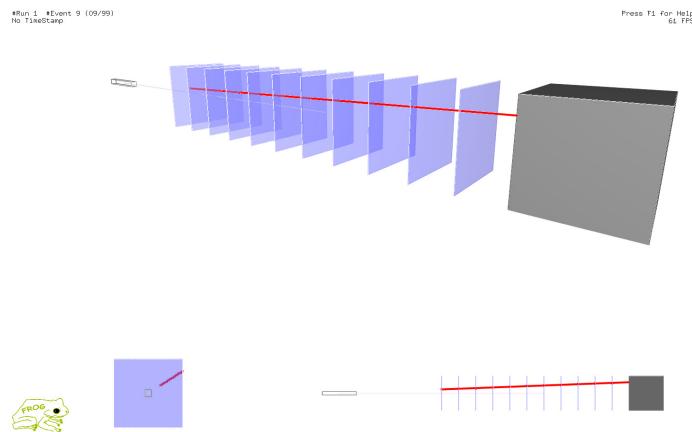


Figure A.6: Three different FROG Display views: 3D view (top), 2D longitudinal (bottom right), transversal view (bottom left). The different geometry parts are well visible : Particle Gun (grey), the Ending Block (grey) and the eleven tracking layers (blue). The particle track is shown in red.

## A.4 FROG Features

### A.4.1 Config File

FROG is fully configurable by a set of parameters defined in an ASCII file generally named (`config.txt`). The parameters may also be defined in other ASCII files that are included by the main configuration file. This file may be reloaded at any time in order to take new modifications into account, typically thresholds modification. Some of these options will be described in the next sections. The parameters given by the file(s) are, among other things:

- the path to the Input `.vis` file and/or Input `.geom` file
- the events to display
- the objects color, styles and thresholds
- the views to be used

### A.4.2 Styles

The style option of each FROG can be changed directly in the configuration file. If no style is given to an object, it is assumed that it is similar to the mother object style.

Objects properties are given using the unique object identification number (EventId/DetId). Below is an example of the text block to setup styles of a RecoTrack Collection with and EventId (23100001):

```
Id_23100001_Color      = { 1.0 , 0.0 , 0.0 , 1.0 };
Id_23100001_Thickness   = 3.0;
Id_23100001_Marker      = 0;
Id_23100001_MarkerSize   = 5;
Id_23100001_ShowDet     = false;
```

The `Color` parameter is used to set up the default (Red, Green, Blue, Alpha) component of the track color. The `Thickness` defines the thickness of the line used to draw the track while `Marker` (`MarkerSize`) defines the type (size) of the marker used to display the hits associated to the track. Many different markers can be used, and user can add himself new ones. Finally `ShowDet` defines if the detector module associated to the hits has to be drawn or not.

### A.4.3 Mouse Interface

Any displayable object can be selected by mouse. When it happens, the information concerning the selected object are displayed on the screen. For instance, when a track is selected, its momentum, transverse momentum,  $\chi^2$  and the number of hits are printed.

The selection routine is a non trivial part of the FROG Display Core: view projection matrix can not be reversed in order to find the object (in a 3D space) associated to a point on screen, this choice is basically not unique. So tricks have to be used.

### A.4.4 Web interface

The event (`.vis`) and geometry (`.geom`) files can be downloaded via Internet (world wide web) via the http or ftp protocols. FROG will download automatically the files using the libcurl URL transfer library: LIBCURL [81]. It is possible to update the event file periodically in intervals of time defined in the configuration file: This can be steered by setting the URL and file refresh time in the configuration file. For example:

- `InputVisFile = {http://projects.hepforge.org/frog/tut/02/SimulatedEvents.vis};`
- `InputGeom = {http://projects.hepforge.org/frog/tut/02/MyCustomTracker.geom};`
- `updateVisFileTime = 10; // File Update Interval in seconds`

This feature is useful for online visualization since the `.vis` file needs to be refreshed to consider the newly recorded events. When negative refresh time values are used, the file is never updated.

### A.4.5 Compressed files (GZip)

FROG can read and write (GZip) compressed files thanks to the ZLIB [82]. Compressed input `.vis/.geom` files are automatically uncompressed. The user can configure the FROG Producer so it creates `.vis.gz` files instead of `.vis` files. This is very convenient when files need to be archived or distributed via Internet. The compression rate is between 50% and 70% depending on the event content.

### A.4.6 View System

A flexible view system is implemented in order to increase the program flexibility. The user can always create the set of views that suits him best only by changing the configuration file. The view is defined by a set of parameters in the configuration file:

- Type of the view
- Position and Size of the view on screen (viewport)
- Camera Position and Target
- Camera movement (animate or not)
- Background Geometry
- Vertex/Pixel Shader to use
- Kind of Projection to use

Different types of view are available: 3D view, 2D orthogonal projection view, logo/text view, logo plot view, etc. The code that defines the different views is fully tunable in order to add easily new types of view [83].

### A.4.7 Tree menu

The FROG Displayer contains a Tree menu, see Figure A.7, that is used to set which Geometry/Event parts have to be displayed. This menu reflects the `.vis/.geom` (FFF) structure, see Figure A.3. The branches of the tree represent group of objects (detector or event data). The initial display state of the objects can be defined in the configuration file. The menu can also be used to list all the objects of a given collection and compare their properties.

### A.4.8 Online Mode

FROG can be used in online mode to have, in real time, clues on the quality of data taken by the experiment. In online mode, the Producer and the Displayer are used simultaneously. In other words, the Displayer can read a .vis while the Producer is pushing events into it. Many Displayers can be reading the same file as well. When the file size reaches a configurable limit, the Producer can just overwrite it without consequence for the Displayer connected to the file. The FROG Displayer can be used to display the latest event in the file, which is very convenient for the online running mode. The user can stop the event refresh to spend more time on one interesting/suspicious event, this have no consequence for the other Displayer connected to the same file.

This functionality has been used intensively for the first LHC  $pp$  collision in CMS at  $\sqrt{s} = 900$  GeV, 2.36 TeV. But also during the CMS Media event for the first collisions at 7 TeV on March 30th, 2010. During this exercise, FROG appears to be more stable and more quick than the other visualization tools.

### A.4.9 Stereoscopic and Anaglyph Rendering

A rendering technique capable of recording three-dimensional visual information or creating the illusion of depth in an image is qualified by stereoscopic rendering. Many techniques exist but FROG uses only two of them. The two are based on the same

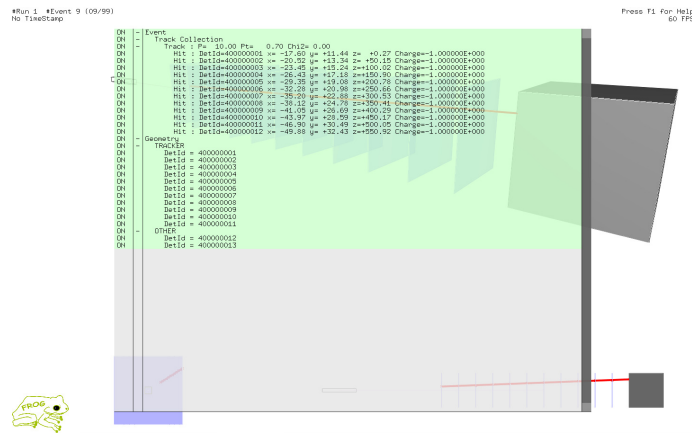


Figure A.7: Similar to Figure A.6 except that the  $<\text{t}>$  menu is opened. Both the event and geometry structures are visible. All the lines are green since all the objects are displayed. Hits position and charge are listed as well as the track properties.

principle. In order to give a depth impression to a scene, two different images of a same scene must be taken and sent separately to the left and right eye. The brain will make the recombination of the pictures as it does for standard vision. The two images must only differ by the position of the camera, which is translated by few centimeters between the two images. This first step is generally common to all stereoscopic techniques. Techniques differ in how the images are sent to the eyes.

The so-called Full Stereoscopy technique displays the two images on a special 3D display. Different kinds of displays exist: some displays make use of the light polarization to make the separation between the two images. In this case, the two images are projected on screen simultaneously but with different light polarizations, and the user wears polarization filter glasses that are used to get the right picture on the right eye and vice versa. Some other devices have a high refresh rate ( $> 120\text{Hz}$ ) and display the pictures alternatively while active glasses turn on the left eye and turn off the right eye when the left picture is displayed and vice versa. The latter is the technique that has the largest support of the industry and is going to be generalized in the coming years. Some other devices have special pixels that are divided into two parts, each of them being visible only by one eye.

Since the full stereoscopic rendering technique requires a special display device, it is generally quite expensive and not available to everyone. For this reason, a second method, cheaper, has been implemented in FROG. This method is called Anaglyph rendering and uses two simple color filters to direct the right image to the right eye. Idea is similar to the polarization method: the user wears glasses with different color filters for each eye. Standard is red/cyan glasses, which means that left eye has a red filter while right eye has a cyan filter. Only one picture is needed with this rendering technique, the red component of the image is seen by the left eye and only by this one, while the blue and green components of the picture are visible only by the right eye. So the red (green+blue) components play the same role as the left (right) eye picture of the previous technique. The disadvantage of this technique is that the color spectrum of the picture is obviously destroyed, so grey pictures are generally used before eye separation. An option is available to render the scene in grey scale color. On the other hand, the advantage of the method is its very small cost: only color filter glasses are needed. An other one is that the picture can be printed without consequences on the depth impression. The Figure A.8 shows few Stereoscopic (Anaglyph) screenshots.

#### A.4.10 Production of Pictures and Animations

Event display tools have to be able to record screenshots of nice/special events or detector geometry parts. There are two fundamentally different types of digital pictures.

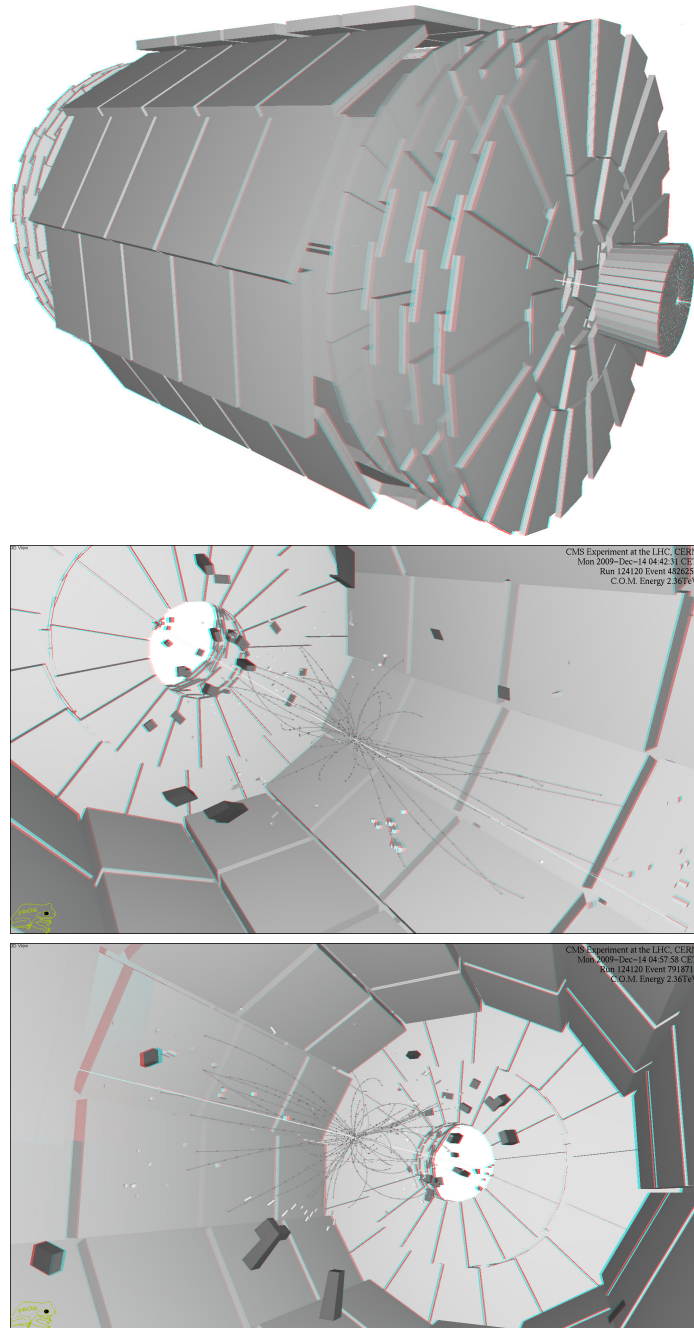


Figure A.8: Stereoscopic (Anaglyph) Screenshots of CMS Geometry (top) and Events (middle and bottom). Red/Cyan glasses are needed to have the depth illusion.

The first type, called raster picture, stores the color of the different pixels composing the picture in a pixel array. The picture quality only depends on the size of this array. PNG and JPEG are well known raster picture format supported by FROG via the PNGLIB [84] and JPEGLIB [85] library. Generally, the event display tool just copies the pixel array sent to the screen into a PNG/JPEG file. For this reason, the quality of the raster picture is fixed by the screen resolution which is generally not good enough to be printed on large scientific poster. For this reason, FROG uses a different technique based on the OPENGL Frame Buffer Object (FBO) that allows to create raster pictures of the desired resolution (up to  $6000 \times 6000$  pixels).

In the second type, called vector picture, the pixels array is replaced by a primitive vector. These primitives can be used to recreate a pixel array of any size. For that reason, the vector picture has an infinite resolution. The primitives are just lines, points, polygons, etc. EPS, PS, PDF, SVG are well known vector picture format supported by FROG via the GL2PS library [86]. The idea is to store directly the OPENGL primitives used to render the scene on the screen. Vector pictures are slow to be created and heavy since they store the complete information, but they have an infinite resolution. On the other hand, they can not be easily modifiable like the raster pictures.

3D Stereoscopic picture (Anaglyph or not) can be produced by the FROG Display. In the case of full 3D Stereoscopic pictures, two screenshots are made, one for the left eye and one for the right eye. In the case of Anaglyph picture, one unique (raster only) picture is made, the red component of the picture is extracted from the left eye view while the blue and green components of the picture are extracted from the right eye view.

A set of recorded raster pictures can be merged via external tools in order to convert them into animations. A couple of default images sequence production are already implemented. This is generally time consuming, because 25 pictures must be produced for each second of animation. The resolution of the animation is fixed by the screenshot resolution, the FullHD ( $1920 \times 1080$ ) resolution is commonly used for animation purposes. 3D Stereoscopic (Anaglyph or not) animations can be created as well by setting the option on the screenshot format.

This functionality has been used intensively for the CMS Media event organized for the first collisions at 7 TeV on March 30th, 2010. The first CMS events were animated in quasi-real time and distributed to the international press as official CMS material for the media. The animation were also broad-casted via Internet and encountered a huge success with more than 50,000 downloads within the first 24 hours.

### A.4.11 Vertex and Pixel Shaders

A shader is a set of software instructions which is used to calculate rendering effects on graphics hardware with a high degree of flexibility. Shaders are used to program the graphics processing unit (GPU) programmable rendering pipeline. Two different kinds of shader are used in FROG:

Vertex Shaders describe the operations that occur on OPENGL primitive vertex values and their associated data. The shader is a GLSL code that describes the operations that will be applied on all the primitives vertices. Operations are mainly position transformations from the 3D space of the scene to the 2D screen surface. But the operations may also act on the vertices colors and transparency: a part of the lighting effects are typically computed at this step.

Fragment or Pixel Shaders describe the operations that occur on OPENGL primitive fragment. A fragment is a pixel resulting from the rasterization of a primitive. Like the vertex shader, the pixel shader is a GLSL code that describes the operations that will be applied on all the primitives fragments. Operations are mainly color transformation and lighting effects.

The number of fragments is by definition much higher than the number of vertices, so the quality of the effects/operations is better but slower when applied in fragment shader. A combination of the two types of shader is thus foreseen. The shader code is generally just an ASCII file<sup>2</sup> that is compiled at run time. In FROG, a different vertex and pixel shader can be set for each view. The advantage of the shader is that anyone can modify the shader code without having to recompile anything. Non trivial/linear transformation can thus be defined there. A typical example is shown on Figure A.9. This one shows three different projections of the same CMS event: The first view is just an orthogonal projection of the 3D event on the  $Y - Z$  plane. The second view is a non linear projection of the event on the  $R - Z$  plane, where  $R$  is nothing but  $R = \sqrt{X^2 + Y^2}$ . The last view is the non linear projection on the plane  $\rho - Z$ , where  $\rho = \text{sign}(Y)\sqrt{X^2 + Y^2}$ . Other complex projections can be imagined in order to highlight different parts of the event. A well-known example is the fish-eye view, which is often used to distort transversal view. The transformation change is just  $(R\cos(\phi), R\sin(\phi)) \mapsto (\log(R)\cos(\phi), \log(R)\sin(\phi))$ . All these transformations are defined in the vertex shader code.

---

<sup>2</sup>The ASCII file generally does not exceed  $\sim 10$  lines of code.

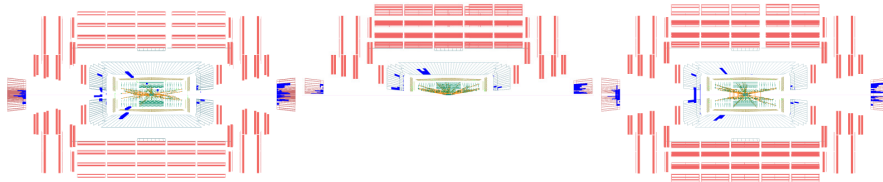


Figure A.9: Three different projections of the same CMS event. The projections are respectively made on the plane:  $Y - Z$ ,  $R - Z$  and  $\rho - Z$ .

## A.5 FROG Applications

FROG is already used in different experiments and environments, some of them are shown in this section. The few examples described in this section show that FROG can be used in many different applications. A non exhaustive list of these will be presented in the coming pages:

- GASTOF is a small detector prototype [46]
- DELPHES is not a detector but a framework for the fast simulation of the response of a generic detector in high energy physics [45]
- The ILD is one detector design for the future International Linear Collider [43]
- The TOTEM experiment is one of the LHC experiment dedicated to the precise measurement of the proton-proton interaction cross section [26]
- The CMS experiment is one of the general purpose LHC experiment, has a very large and complex geometry that is in general hard to render properly [25]

### A.5.1 GASTOF: The Ultra-Fast Gas Time-of-Flight Detector

GASTOF [46, 47] detectors are Cherenkov gas detectors that will be located at 420 m from the CMS [25] and ATLAS [87] interaction point (IP), as part of the FP420 project [88] for the LHC [89]. The aim of these detectors is to reduce backgrounds due to accidental coincidence of events detected in the central detectors and in the FP420 detectors on each side of the IP. To achieve that, the  $z$ -coordinate of the event vertex measured by the central detectors is compared to the vertex reconstructed by measuring the time difference of forward proton arriving to the GASTOF detectors on two sides of the given IP. Cherenkov photons produced by high energy protons traversing gas medium are reflected by a mirror onto a very fast photomultiplier. The Figure A.10 shows a simulated GASTOF event displayed by FROG.

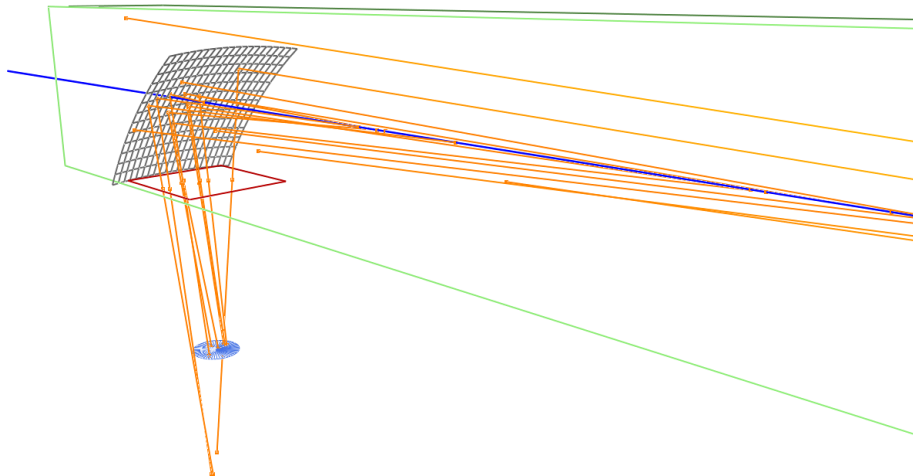


Figure A.10: 3D view zoomed on the GASTOF mirror. The proton trajectory is represented by the blue line while photon rays are shown in yellow. The Cherenkov photon production is well visible along the proton path. The majority of the produced photons is reflected by the curved mirror and focused on the photo-cathode.

The figures below show the simulated GASTOF events coming from the ray-tracing done by the GASTOF simulator [90]. The Figure A.11 shows 2D Y-Z projections of four different events while the Figure A.10 shows a 3D view of another event. In both cases, the Cherenkov photon paths (ray) are drawn in yellow.

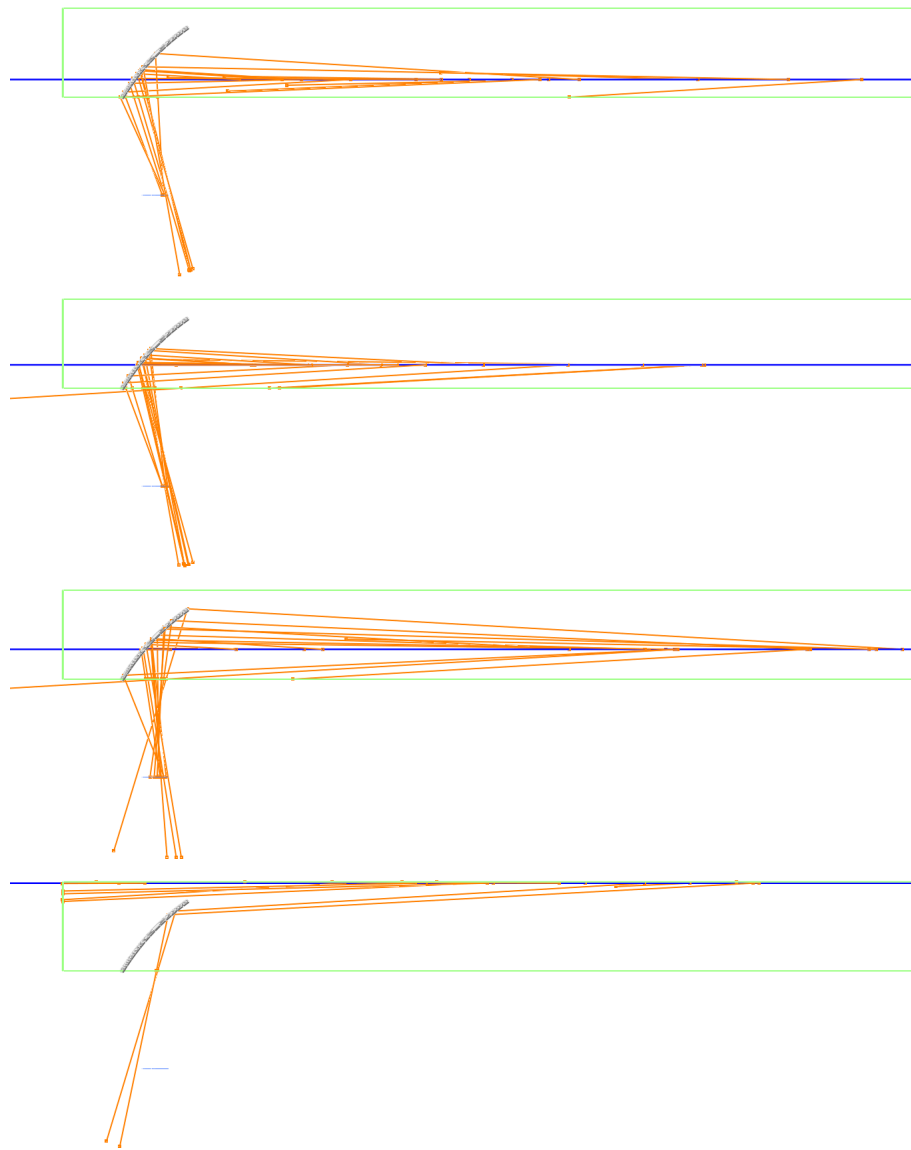


Figure A.11: 2D views of four different GASTOF events: The proton trajectory (going from right to left in that view) is represented by the blue line, while photon trajectories (ray) are shown in yellow. The Cherenkov photon production is well visible along the proton path. The majority of produced photons are reflected by the curved mirror and focused on the photo-cathode. Note that some photons are not reflected on the mirror and than some others miss the PMT.

### A.5.2 DELPHES: a Framework for the Fast Simulation of a General Purpose Collider Experiment

The DELPHES framework [45] is a fast and realistic simulator of a general purpose experiment, like CMS [25] or ATLAS [87] at the LHC. In addition of the usual components of such detector, DELPHES also simulates very forward detectors arranged along the beam line.

The overall layout of the general purpose detector simulated by DELPHES is shown in Figure A.12 and A.13. The innermost layer, close to the interaction point, is a central tracking system (pink). It is surrounded by a central calorimeter volume (green) with both electromagnetic and hadronic sections. The outer layer of the central system (red) consists of a muon system. In addition, two end-cap calorimeters (blue) extend the pseudo rapidity coverage of the central detector. The actual detector granularity and extension are defined in the DELPHES user-configuration card. The detector is assumed to be strictly symmetric around the beam axis (black line). Additional forward detectors are not depicted. The configuration of the subsystems used in these examples is summarized in Table A.1. The geometry displayed by FROG reflects the configurable DELPHES geometry as figured on right of Figure A.12.

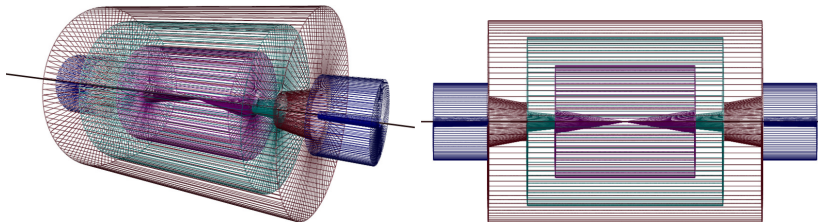


Figure A.12: Left: Layout of the generic detector geometry assumed in DELPHES. Right: Profile of the layout assumed in DELPHES.

System	Extension in pseudorapidity	
Tracking	$0.0 \leq  \eta  \leq 2.5$	
Calorimeters	central	$0.0 \leq  \eta  \leq 3.0$
	forward	$3.0 \leq  \eta  \leq 5.0$
Muon system	$0.0 \leq  \eta  \leq 2.4$	

Table A.1: Configuration of the subsystems used in the examples presented in Fig. A.12 and A.13

The visualization of the collision final states, as well as the detector geometry, is possible via a dedicated Producer interfacing FROG to DELPHES. One example of a Detector Parametrization used by DELPHES is shown on the Figure A.13. The same figure also shows how the DELPHES events are visualized at the vertex level (before the propagation into the detector).

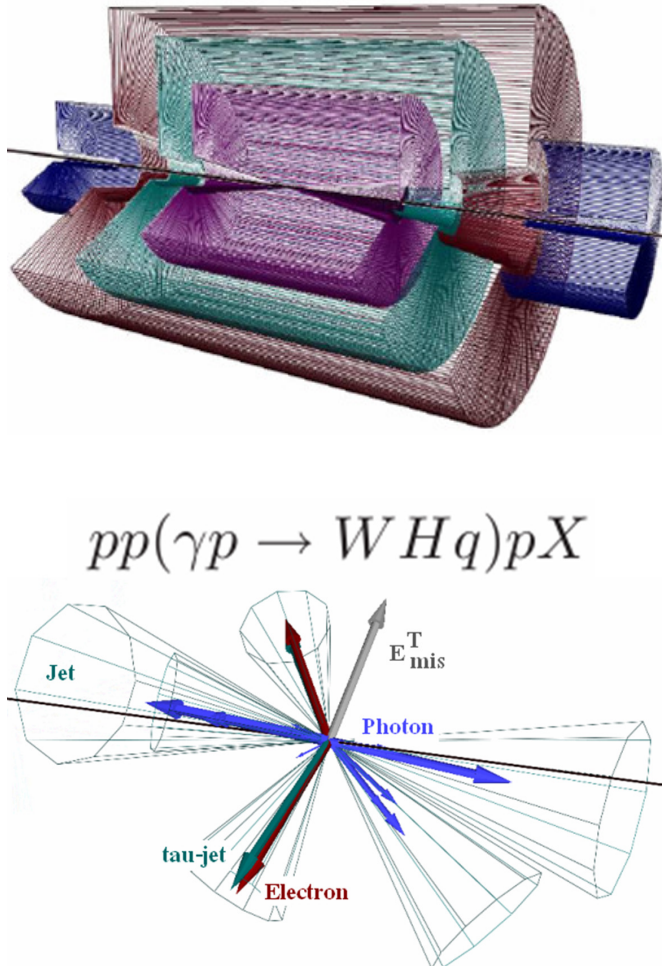


Figure A.13: Top: A 3D open view of the generic detector used by DELPHES. The parametrization of the detector is given by the user. Bottom: Display of a photon-photon event at the vertex.

### A.5.3 ILD: The ILC Detector Design

The ILD [43] is a detector design for the future International Linear Collider. A part of the CALICE [44] collaboration is using FROG for the design of the ILD hadronic calorimeter but also during test beams. The Figure A.14 shows one of the ILD HCAL Barrel Design, this one is composed of 48 RPC layers. In this simulated event, all the details of the hadronic shower initiated by a single K-long are well visible.

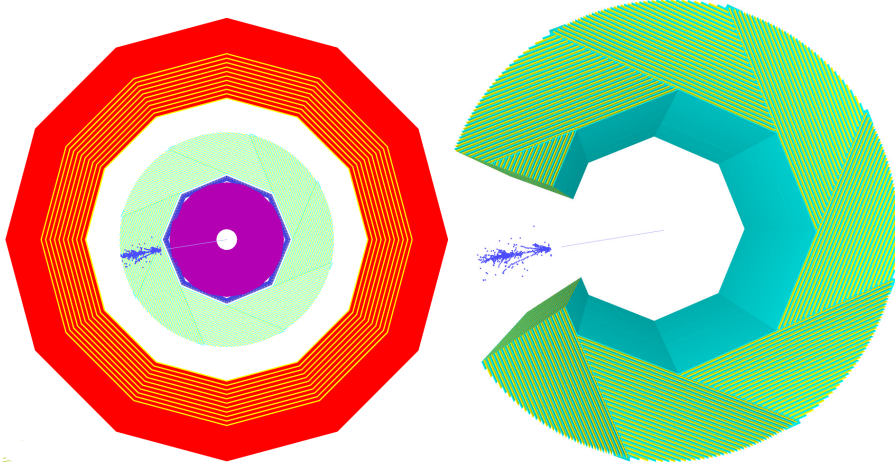


Figure A.14: Right: A transverse view of the geometry of one of the ILD Design. From inner to outer layers: the TPC (pink), the ECAL Barrel (Blue), the 48 HCAL Barrel Active (light yellow) and Passive (turquoise) layers, the muon detectors (yellow) and finally the magnetic field return yoke (red). A single K-long simulated event creating a hadronic shower in the HCAL subdetector is superimposed on the figure. Right: Same event shown in an open 3D-view of the HCAL Barrel geometry. The high granularity of the hadronic calorimeter is well visible.

#### A.5.4 TOTEM: The TOTEM Experiment

The TOTEM (TOTal cross section, Elastic scattering and diffraction dissociation Measurement at the LHC) [26] experiment is dedicated to the precise measurement of the proton-proton interaction cross section, as well as the in-depth study of the proton structure. The TOTEM Event Display software is based on FROG. The Figure A.15 shows a 7 TeV LHC event observed in the TOTEM geometry. Trajectories of very forward particles coming from the CMS interaction points are reconstructed both in the TOTEM telescopes and in the roman pots sensors. FROG was intensively used by the TOTEM group for commissioning and outreach purposes during 2010 LHC runs.

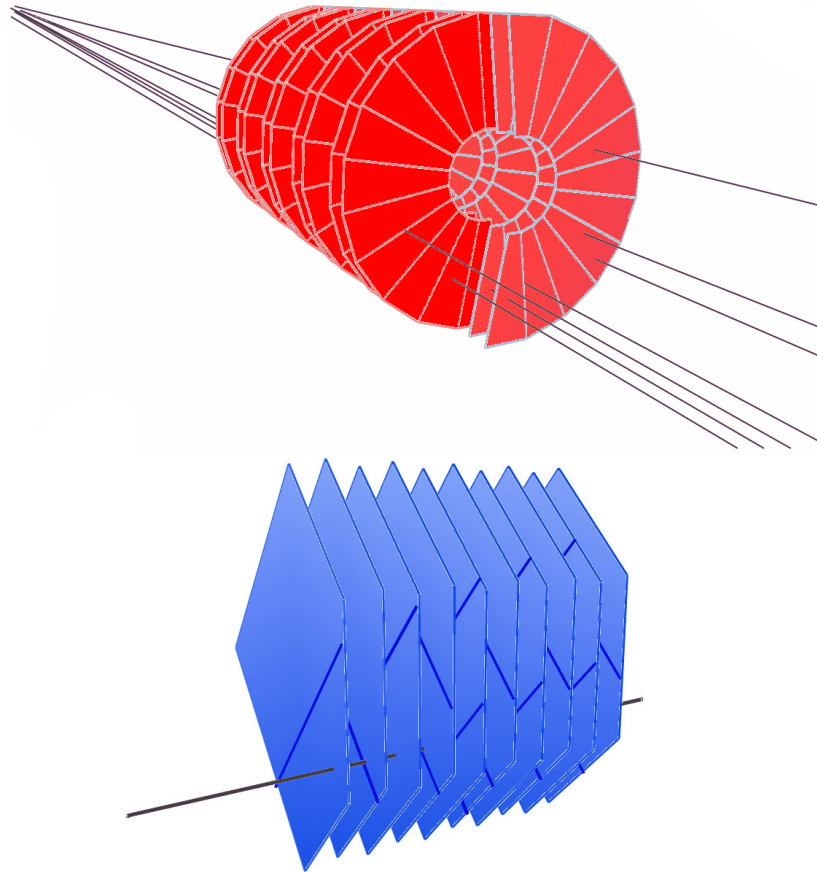


Figure A.15: Very forward particles coming from a real 7 TeV  $pp$  collision in CMS observed with the TOTEM detector. Top: track segments in a TOTEM telescope (T2-). Bottom: shows a track segment in a TOTEM roman pots (123).

### A.5.5 CMS: The Compact Muon Solenoid

The Compact Muon Solenoid [25] is one of two general-purpose particle physics detectors built on the Large Hadron Collider (LHC) [89]. It is capable of studying many aspects of proton collisions with a center of mass energy up to 14 TeV. A FROG Producer has been created as an additional module of the CMS Software (CMSSW) [91]. The displayed geometry is ensured to be exactly the same than the geometry used by CMSSW for the event reconstruction since it is automatically extracted from the CMS database by the Producer. This is important for debugging purpose. The Producer can be used both on simulated and real data.

A couple of event display of special CMS events are shown in this section. A detailed description of these events will not be given since it is out of the scope of this chapter, however a short description of the event key features is given in the legend of the figures. Display examples of simulated events are visible in Figures A.16 and A.17. The first shows a QCD Dijet event with a center-of-mass energy of 3.5 TeV while the second is a heavy ion (Pb-Pb) collision event in CMS. Finally, few special real data events are also illustrated in Figures A.18 and A.19. These events are, respectively, one of the first events recorded by CMS produced with a center-of-mass energy of 7 TeV, and the best di-leptonic top candidate observed so far at CMS. Two illustrations of the CMS Geometry have already been shown in Figure 2.6 and Figure 2.7.

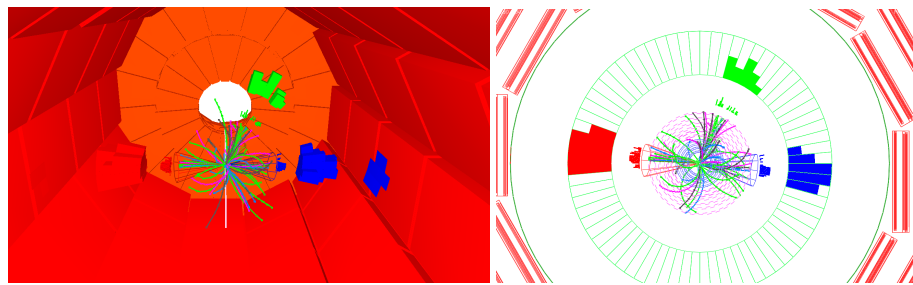


Figure A.16: A 3D and a transversal view of a simulated QCD Di-jets event with a center of mass energy of 3.5 TeV. The jets are represented by a cone pointing towards the jet calorimeter hits. The hit size is proportional to the logarithm of its energy. The first (second) leading  $p_T$  jet is drawn in red (blue), the others jets are green. A third jet coming from an initial gluon radiation is also visible.

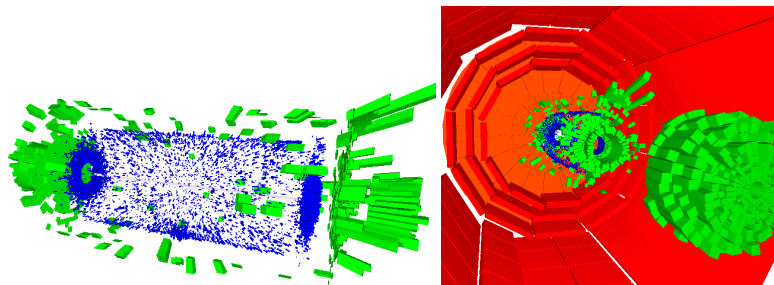


Figure A.17: CMS will also study the heavy ion (lead-lead) interactions. These events are characterized by a large calorimetric activity due to the amount of available energy in the collision. The two 3D views show the calorimeter hits of a simulated heavy ion collision: electromagnetic (hadronic) calorimeter hits are drawn in blue (green). The hit size is proportional to the logarithm of its energy.

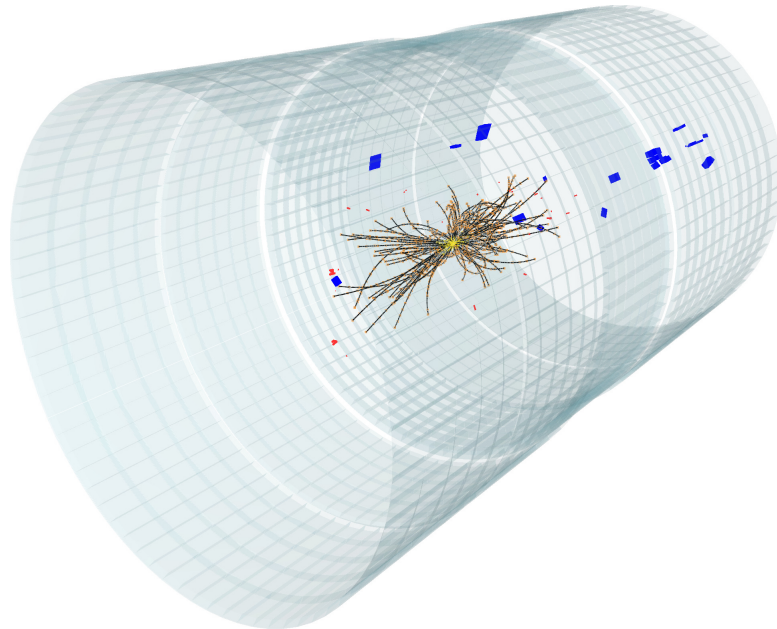


Figure A.18: 3D view of one of the first 7 TeV events (Run132440 Event4285681) recorded on 30 March 2010 at 13h23 CET. In this figure, tracks are shown in black, the Silicon Strip (Pixel) clusters associated to a track are shown in orange (yellow), while the ECAL (HCAL) hits are drawn in red (blue). The HCAL Outer (HO) calorimeter (transparent volume), located just between the CMS solenoid magnet and the CMS barrel muon system, is shown to give the proportion of the CMS detector.

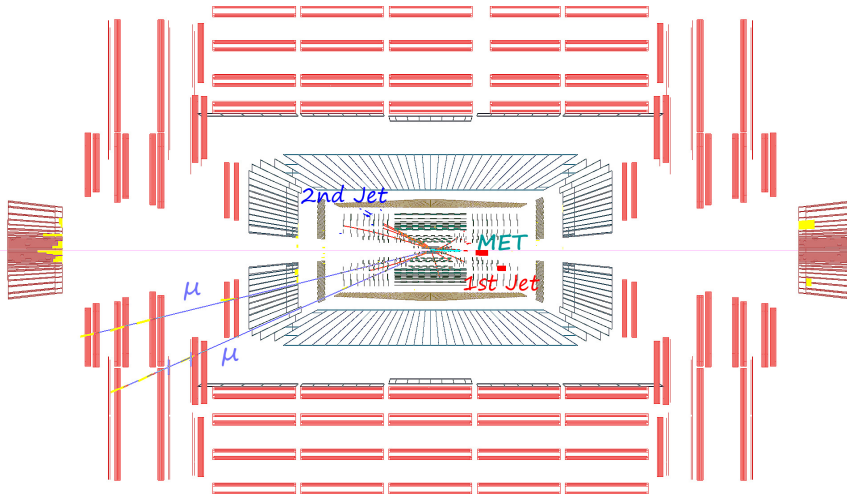


Figure A.19: Longitudinal view of the best Top candidate event produced in CMS for the time being. This di-leptonic event is made of two b-jets (56 and 45 GeV) coming from the decay of the two top quarks:  $t \rightarrow W^+b$ . Two reconstructed muons (57 and 27 GeV) and lots of missing transverse energy (57 GeV) are also present and both the muon and the missing energy come from the  $W$  decay:  $W^+ \rightarrow \mu^+\nu_\mu$ .

## A.6 Conclusion

The philosophy of the visualization tool developed during the doctoral work, FROG, solved many of the issues affecting the historical CMS visualization software. FROG was not initially designed to replace any software but simply to show that slowness in high granularity capable event display is not a fatality. But given the numerous success encountered by the first prototype, the development continued. Today, FROG is known to be one of the more flexible and fast event display available on the market. It is the only visualization tool that is used by two LHC experiments, but also by the ILC community and other smaller research groups. It is also the only tool able to animate collision event or detector geometry. Finally, FROG have some unique features that allow to create high resolution vectorial or raster (up to  $6000 \times 6000$  pixels) pictures but also 3D-stereoscopic or 3D-anaglyphs images and videos, this eases the communication work of the physics collaborations. The small size (<5MB) of the completely standalone package turns also FROG in one of the best tool for outreach and education purposes, since it can be easily copied and installed on almost any computer.

Appendix **B**

## Bethe-Bloch Approximation

In this section, the operation applied to approximate the Bethe-Bloch formula by a more simple parametrization for non-relativistic particles are detailed. First,  $T_{\max}$  is reduced to  $2m_e c^2 \beta^2 \gamma^2$  for particles much heavier than an electron, which is obviously true for low momenta hadrons or HSCP. Then, in order to simplify the calculation, the many constants are merged together into two unique constants: "a" and "b". The ionization term  $\delta(\beta\gamma)$  is small and therefore simply neglected.

$$\begin{aligned}
 \left\langle \frac{dE}{dx} \right\rangle &= -kz^2 \frac{Z}{A} \frac{1}{\beta^2} \left[ \frac{1}{2} \ln \frac{2m_e c^2 \beta^2 \gamma^2 T_{\max}}{I^2} - \beta^2 - \frac{\delta(\beta\gamma)}{2} \right] \\
 &\approx -kz^2 \frac{Z}{A} \frac{1}{\beta^2} \left[ \frac{1}{2} \ln \frac{(2m_e c^2 \beta^2 \gamma^2)^2}{I^2} - \beta^2 - \frac{\delta(\beta\gamma)}{2} \right] \\
 &= -kz^2 \frac{Z}{A} \frac{1}{\beta^2} \left[ \frac{2}{2} \ln \frac{2m_e c^2 \beta^2 \gamma^2}{I^2} - \beta^2 - \frac{\delta(\beta\gamma)}{2} \right] \\
 &= -\frac{a}{\beta^2} \left[ \ln(b \beta^2 \gamma^2) - \beta^2 - \frac{\delta(\beta\gamma)}{2} \right] \\
 &\approx -\frac{a}{\beta^2} [\ln(b \beta^2 \gamma^2) - \beta^2] \\
 &\approx -\frac{a}{\beta^2} \left[ \ln\left(\frac{b \beta^2}{1 - \beta^2}\right) - \beta^2 \right] \\
 &\approx -\frac{a}{\beta^2} [\ln(b \beta^2) - \ln(1 - \beta^2) - \beta^2]
 \end{aligned}$$

The logarithmic term can now be approximated using a first order Taylor expansion since:  $\ln(1 - x) \approx -x$  for values of  $x$  in  $[-1, 1]$  and similarly,  $\ln(x) = \ln(1 + (x - 1)) \approx x - 1$  for values of  $x$  in  $[0, 2]$ . Then  $(1 - \beta^2)$  can be rewritten as  $1/\gamma^2$ .

$$\begin{aligned}
\left\langle \frac{dE}{dx} \right\rangle &\approx -\frac{a}{\beta^2} [\ln(b \beta^2) - \ln(1 - \beta^2) - \beta^2] \\
&\approx -\frac{a}{\beta^2} [(b \beta^2 - 1) - (-\beta^2) - \beta^2] \\
&\approx -\frac{a}{\beta^2} [b \beta^2 - 1] \\
&\approx -\frac{a}{\beta^2} [(b - 1) \beta^2 + \beta^2 - 1] \\
&\approx -\frac{a}{\beta^2} \left[ (b - 1) \beta^2 - \frac{1}{\gamma^2} \right] \\
&\approx \left[ a (1 - b) + \frac{a}{\beta^2 \gamma^2} \right]
\end{aligned}$$

Finally, the constants "a" and "b" can be rewritten to make appear the parametrization used in the chapter 4:

$$\begin{aligned}
\left\langle \frac{dE}{dx} \right\rangle &\approx \left[ a (1 - b) + \frac{a}{\beta^2 \gamma^2} \right] \\
&\approx C + K \frac{m^2}{p^2}
\end{aligned}$$

The constants  $K$  and  $C$  are both positive constants because the constant "b" is much smaller than unity since the mean excitation energy ( $I$ ) in silicon is of the order of  $173 \pm 3$  eV.

# Bibliography

- [1] T.P. Cheng and L.F. Li, “Gauge theory of elementary particle physics”, *Clarendon Press, Oxford*, 1984.
- [2] E. Komatsu et al., “Five-Year Wilkinson Microwave Anisotropy Probe (WMAP) Observations:Cosmological Interpretation”, *Astrophys. J. Suppl.*, vol. 180, pp. 330–376, 2009.
- [3] M. C. Gonzalez-Garcia and Y. Nir, “Developments in neutrino physics”, *Rev. Mod. Phys.*, vol. 75, pp. 345–402, 2003.
- [4] H. Georgi and S. L. Glashow, “Unity of all elementary-particle forces”, *Phys. Rev. Lett.*, vol. 32, no. 8, pp. 438–441, Feb 1974.
- [5] P. Chen and J.-A. Gu, “Cosmological Constant as a Manifestation of the Hierarchy”, , 2007.
- [6] M. Fairbairn, A. C. Kraan, and D. A. Milstead et al, “Stable Massive Particles at Colliders”, 2006.
- [7] G. F. Giudice and A. Romanino, “Split Supersymmetry”, *ERRATUM-IBID.B*, vol. 706, pp. 65, 2005.
- [8] M. Carena, D. Choudhury, and R. A. Diaz et al, “Top-squark searches at the Tevatron in models of low-energy supersymmetry breaking”, *Physical Review D*, vol. 66, pp. 115010, 2002.
- [9] G. F. Giudice and R. Rattazzi, “Theories with Gauge-Mediated Supersymmetry Breaking”, *Physics Reports*, vol. 322, pp. 419, 1999.
- [10] C. Macesanu, C. D. McMullen, and S. Nandi, “Collider Implications of Universal Extra Dimensions”, *Physical Review D*, vol. 66, pp. 015009, 2002.

- [11] R. Mackeprang and D. Milstead, “An Updated Description of Heavy-Hadron Interactions”, *Eur. Phys. J.*, vol. C66, pp. 493–501, 2010.
- [12] R. R. Wilson, “The Tevatron”, *Phys. Today*, vol. 30N10, pp. 23–30, 1977.
- [13] T. Sjostrand, S. Mrenna, and P. Z. Skands, “PYTHIA 6.4 Physics and Manual”, *JHEP*, vol. 05, pp. 026, 2006.
- [14] L3 Collaboration, “Search for Heavy Neutral and Charged Leptons in e+ e- Annihilation at LEP”, *Physics Letters B*, vol. 517, pp. 75, 2001.
- [15] LEP SUSY Working Group, ALEPH, DELPHI, L3 and OPAL Collaborations, “Heavy Stable Charged Particles (LEPSUSYWG/02-05.1)”, *LEPSUSYWG/02-05.1*, 2004.
- [16] D. Acosta et al., “Search for Long-lived Charged Massive Particles in anti-p p Collisions at  $\sqrt{s} = 1.8$  TeV”, *Physical Review Letters*, vol. 90, pp. 131801, 2003.
- [17] F. Abe et al, “Search for heavy stable particles in 1.8-TeV  $p\bar{p}$  collisions at the Fermilab collider”, *Phys. Rev. Lett.*, vol. 63, no. 14, pp. 1447–1450, Oct 1989.
- [18] F. Abe et al, “Limits on the production of massive stable charged particles”, *Phys. Rev. D*, vol. 46, no. 5, pp. R1889–R1894, Sep 1992.
- [19] D. Acosta et al, “Search for Long-Lived Charged Massive Particles in  $p\bar{p}$  Collisions at  $\sqrt{s} = 1.8$  TeV”, *Phys. Rev. Lett.*, vol. 90, no. 13, pp. 131801, Mar 2003.
- [20] V. M. Abazov et al, “Search for Long-Lived Charged Massive Particles with the D0 Detector”, *Phys. Rev. Lett.*, vol. 102, no. 16, pp. 161802, Apr 2009.
- [21] T. Aaltonen et al., “Search for Long-Lived Massive Charged Particles in 1.96 TeV  $p\bar{p}$  Collisions”, *Phys. Rev. Lett.*, vol. 103, no. 2, pp. 021802, Jul 2009.
- [22] R. Adolphi et al., “The CMS experiment at the CERN LHC”, *JINST*, vol. 0803, pp. S08004, 2008.
- [23] L. Evans et al., “LHC Machine”, *JINST*, vol. 0803, pp. S08001, 2008.
- [24] D. Boussard and T. Linnecar, “The LHC Superconducting RF System”, *LHC Project Report*, vol. 316, 1999.
- [25] M. Della Negra, A. Petrilli, and A. Hervé et al., “CMS: The Compact Muon Solenoid, CMS Physics: Technical Design Report 1”, CERN/LHCC 2006-001, 2006.

- [26] TOTEM Collaboration, “The TOTEM Experiment at the CERN Large Hadron Collider”, *JINST*, 2008.
- [27] CMS Collaboration, “The Magnet Project Technical Design Report”, *CERN/LHCC 1997-10*, 1997.
- [28] CMS Collaboration, “The Tracker Project Technical Design Report”, *CERN/LHCC 1998-6*, 1998.
- [29] CMS Collaboration, “Addendum to the CMS Tracker Technical Design Report”, *CERN/LHCC 2000-16*, 2000.
- [30] CMS ECAL Collaboration, “CMS ECAL Technical Design Report”, *CERN/LHCC 1997-33*, 1997.
- [31] CMS Collaboration, “Electromagnetic calorimeter calibration with 7 tev data”, *CMS Physics Analysis Summary, EGM-10-003*, 2010.
- [32] CMS Collaboration, “The Hadron Calorimeter Technical Design Report”, *CERN/LHCC 1997-31*, 1997.
- [33] CMS HCAL Collaboration, “Energy Response and Longitudinal Shower Profiles Measured in CMS HCAL and Comparison with GEANT4”, *CMS NOTE 2006/143*, 2006.
- [34] CMS Muon Collaboration, “CMS Muon Technical Design Report”, *CERN/LHCC 1997-32*, 1997.
- [35] CMS Collaboration, “The TriDAS project, technical design report. Volume 1: The level-1 trigger”, *CERN-LHCC-2000-038*, 2000.
- [36] CMS Collaboration, “The TriDAS project, technical design report. Volume 2: Data acquisition and high-level trigger technical design report”, *CERN-LHCC-2002-026*, 2002.
- [37] CMS Collaboration, “CMS technical design report, volume II: Physics performance”, *J. Phys.*, vol. G34, pp. 995–1579, 2007.
- [38] F. Maltoni and T. Stelzer, “MadEvent: automatic event generation with MadGraph”, *Journal of High Energy Physics*, vol. 2003, no. 02, pp. 027, 2003.
- [39] S. Agostinelli et al., “GEANT4: A simulation toolkit”, *Nucl. Instrum. Meth.*, vol. A506, pp. 250–303, 2003.
- [40] L. Quertenmont and V. Roberfroid, “FROG: the Fast and Realistic OpenGL Displayer”, <http://projects.hepforge.org/frog/>, 2009, *arXiv:hep-ex/09012718v1*.

- [41] “OPENGL: Open Graphical Library”, <http://www.opengl.org>.
- [42] “GLUT: OPENGL Utility Toolkit”, <http://www.opengl.org/resources/libraries/glut/>.
- [43] “The ILD Collaboration”, <http://www.ilcild.org/>.
- [44] “The CALICE Collaboration”, <https://twiki.cern.ch/twiki/bin/view/CALICE>.
- [45] V. Lemaitre, S. Ovyn, and X. Rouby, “DELPHES”, arXiv:hep-ph/0903225, 2009.
- [46] L. Bonnet, T. Pierzchala, and K. Piotrzowski et al, “GASTOF: Ultra-fast ToF forward detector for exclusive processes at the LHC”, arXiv:hep-ph/0703320; CP3-06-18, 2006.
- [47] L. Bonnet and al., “GASTOF”, *Paper in preparation*, 2009.
- [48] L. Borrello et al., “Sensor design for the cms silicon strip tracker”, Tech. Rep. CMS-NOTE-2003-020, CERN, Geneva, Aug 2003.
- [49] W. Adam and L. Quertenmont et al., “Silicon Strip Tracker Detector Performance with Cosmic Ray Data at the Tracker Integration Facility”, *CMS NOTE-2008/032*, 2008.
- [50] M. Raymond et al., “The CMS Tracker APV25  $0.25\ \mu\text{m}$  CMOS Readout Chip”, *Proceedings of the 6th workshop on electronics for LHC experiments, Krakow*, 2000.
- [51] CMS Collaboration, “Commissioning and Performance of the CMS Silicon Strip Tracker with Cosmic Ray Muons”, *CMS PAPER CFT-09-002*, 2009.
- [52] D. Stefanos, K. Gill, and J. Troska et al., “Predicting the Gain Spread of the CMS Tracker Analog Readout Optical Links”, *CMS Note 2006/145*, 2006.
- [53] CMS Collaboration, “The 2008 CMS Computing, Software and Analysis Challenge”, *CMS IN-2008/044*, 2008.
- [54] CMS Collaboration, “Commissioning of the CMS Experiment and the Cosmic Run at Four Tesla”, *CMS PAPER CFT-09-008*, 2009.
- [55] The Particle Data Group, “Review of Particle Physics”, *Phys. Lett. B* 667, vol. 1, 2008.
- [56] H. Bichsel, “Straggling in thin silicon detectors”, *Rev. Mod. Phys.*, vol. 60, pp. 663–699, 1998.

- [57] G. Bruno, A. Giannanco, and L. Quertenmont, “Ionization energy loss and particle-id performance of the Silicon Strip Tracker with 900 GeV data”, *CMS AN 2010/020*, 2010.
- [58] The CMS Collaboaration, “Tracking and Vertexing Results from First Collisions”, *CMS Physics Analysis Summary, TRK-10-001*, 2010.
- [59] W. T. Eadie, D. Drijard, and F. E. James, *Statistical Methods in Experimental Physics*, North Holland, Amsterdam, 1971.
- [60] F. James, *Statistical Methods in Experimental Physics, 2nd Edition*, World Scientific, Singapore, 2006.
- [61] T.W. Anderson, “On the distribution of the two-sample Cramer-von Mises criterion.”, *Ann. Math. Stat.*, vol. 33, pp. 1148–1159, 1962.
- [62] G. Bruno, C. Nuttens, and L. Quertenmont, “Cleaning the Silicon Strip Clusters collection for  $dE/dx$  particle identification in CMS”, *Note in preparation*, 2010.
- [63] G. Bruno, A. Giannanco, L. Quertenmont, and et al., “Search for Heavy Stable Charged Particles with the CMS detector at  $\sqrt{s} = 7$  TeV”, *CMS AN 2010/194*, 2010.
- [64] The CMS Collaboaration, “Search for Heavy Stable Charged Particles in pp collisions at  $\sqrt{s} = 7$  TeV”, *CMS Physics Analysis Summary, EXO-10-004*, 2010.
- [65] The CMS Collaboaration, “Search for Heavy Stable Charged Particles in pp collisions at  $\sqrt{s} = 7$  TeV”, *CMS Physics Analysis Summary, EXO-10-011*, 2010.
- [66] The CMS Collaboration, “Search for Heavy Stable Charged Particles with  $100 \text{ pb}^{-1}$  and  $1 \text{ fb}^{-1}$  in the CMS experiment”, *CMS Physics Analysis Summary, EXO-08-003*, 2008.
- [67] J. Alwall, S. deVisscher, and F. Maltoni, “QCD radiation in the production of heavy colored particles at the LHC”, *JHEP*, vol. 02, pp. 017, 2009.
- [68] R. Mackeprang and A. Rizzi, “Interactions of coloured heavy stable particles in matter”, *Eur. Phys. J.*, vol. C50, pp. 353–362, 2007.
- [69] G. F. Giudice and R. Rattazzi, “Theories with gauge-mediated supersymmetry breaking”, *Phys. Rept.*, vol. 322, pp. 419–499, 1999.
- [70] B. C. Allanach et al., “The Snowmass points and slopes: Benchmarks for SUSY searches”, *Eur. Phys. J.*, vol. C25, pp. 113–123, 2002.

- [71] F. E. Paige, S. D. Protopopescu, and H. Baer et al., “ISAJET 7.69: A Monte Carlo event generator for p p, anti-p p, and e+ e- reactions”, , 2003.
- [72] The CMS Collaboaration, “Performance of CMS muon reconstruction in pp collisions at  $\sqrt{s} = 7$  TeV”, *CMS Physics Analysis Summary, MU-10-002*, 2010.
- [73] B. Giacomo, A. Giammanco, and L. Quertenmont, “Search for Heavy Stable Charged Particles with the CMS inner tracker”, *CMS AN 2010/053*, 2010.
- [74] A. Kulesza and L. Motyka, “Threshold Resummation for Squark-Antisquark and Gluino-Pair Production at the LHC”, *Phys. Rev. Lett.*, vol. 102, no. 11, pp. 111802, Mar 2009.
- [75] A. Kulesza and L. Motyka, “Soft gluon resummation for the production of gluino-gluino and squark-antisquark pairs at the LHC”, *Phys. Rev. D*, vol. 80, no. 9, pp. 095004, Nov 2009.
- [76] W. Beenakker et al., “Soft-gluon resummation for squark and gluino hadroproduction”, *JHEP*, vol. 12, pp. 041, 2009.
- [77] W. Beenakker, R. Hopker, and M. Spira, “PROSPINO: A program for the PROduction of Supersymmetric Particles In Next-to-leading Order QCD”, , 1996.
- [78] The CMS Collaboaration, “Jet performance in pp Collisions at  $\sqrt{s} = 7$  TeV”, *CMS Physics Analysis Summary, JME-10-003*, 2010.
- [79] The CMS Collaboaration, “Measurement of Tracking Efficiency in CMS”, *CMS Physics Analysis Summary, TRK-10-002*, 2010.
- [80] The CMS Collaboaration, “Measurement of CMS Luminosity”, *CMS Physics Analysis Summary, EWK-10-004*, 2010.
- [81] “LIBCURL”, <http://curl.haxx.se/>.
- [82] “ZLIB”, <http://www.zlib.net/>.
- [83] L. Quertenmont and V. Roberfroid, “FROG Tutorials”, <http://projects.hepforge.org/frog/Tutorial/Tutorial.html>.
- [84] “PNGLIB: Portable Network Graphics Library”, <http://www.libpng.org/>.
- [85] “JPEG Library: Joint Photographic Experts Group Library”, <http://www.jpeg.org>.
- [86] “GL2PS: an OPENGL to PostScript printing library”, <http://www.geuz.org/gl2ps/>.

- [87] The ATLAS Collaboration, “ATLAS Detector and Physics: Performance Technical Design Report”, CERN/LHCC 1999-14/15, 1999.
- [88] M.G. Albrow and R.B. Appleby et al., “FP420: The FP420 R&D Project: Higgs and New Physics with forward protons at the LHC”, arXiv:hep-ex/08060302, 2008.
- [89] M. Benedikt, P. Collier, and V. Mertens et al., *LHC Design Report*, CERN, Geneva, 2004.
- [90] T. Pierzchala and N. Schul, “GASTOF Simulator”.
- [91] M. Della Negra, A. Petrilli, and A. Hervé et al., “CMS: The Compact Muon Solenoid, CMS Physics: Technical Design Report 2”, CERN/LHCC 2006-021, 2006.



# List of Tables

1.1	Cross section for various HSCP model . . . . .	23
2.1	LHC parameters relevant for the CMS detector . . . . .	34
2.2	LHC parameters during the 2010 commissioning . . . . .	35
2.3	Detector type and position in the silicon strip tracker. . . . .	43
3.1	SST signal response as a function of sampling time . . . . .	59
3.2	Absolute charge calibration of the SST tracker . . . . .	74
5.1	Pre-selection efficiencies . . . . .	111
5.2	Selections used in the analysis . . . . .	125
5.3	Counting experiment results for the loose and tight selection . . . . .	128
5.4	Properties of the high mass loose candidates . . . . .	128
5.5	Cross-section upper limit for the tracker+muon selection . . . . .	134
5.6	Cross-section upper limit for the tracker-only selection . . . . .	136
5.7	Cross-section upper limit for the tracker-only selection . . . . .	138
5.8	Sources of systematic errors . . . . .	141
A.1	Example Configuration of the DELPHES subsystems . . . . .	164



# List of Figures

1.1	Schematic representation of the SM particle content . . . . .	18
1.2	Nuclear interactions experienced by HSCP . . . . .	21
1.3	R-hadron charge flipping in CMS . . . . .	22
1.4	HSCP: $p_T$ , $\eta$ and $\beta$ distributions . . . . .	24
1.5	HSCP: $\eta$ vs $\beta$ distributions . . . . .	25
1.6	CDF and LEP limits on HSCP cross section . . . . .	27
1.7	CDF limits on stable stop production . . . . .	27
2.1	Illustration of the LHC geometry. . . . .	30
2.2	Illustration of the CERN accelerator complex . . . . .	32
2.3	LHC temperature in 2009 . . . . .	32
2.4	Delivered/Recorded LHC integrated luminosity . . . . .	36
2.5	Tridimensional view of the CMS detector. . . . .	37
2.6	FROG open views of the CMS detector . . . . .	38
2.7	FROG open view of the CMS tracker . . . . .	38
2.8	The CMS tracker detector layout (1/4 of the $z$ view). . . . .	41
2.9	The CMS muon system layout (1/4 of the $z$ view). . . . .	45
2.10	Momentum resolution of the CMS tracking . . . . .	47

2.11 Illustration of the L1 Trigger . . . . .	48
2.12 Schematic of the FROG components . . . . .	51
2.13 Transverse and longitudinal FROG views of simulated HSCP event . . . . .	53
3.1 Illustration of a SST module . . . . .	56
3.2 Readout scheme of the CMS strip tracker. . . . .	57
3.3 Function of the SST signal amplitude with sampling time . . . . .	58
3.4 SST signal as seen by the FED . . . . .	60
3.5 Illustration of a particle passing through a silicon sensor . . . . .	61
3.6 Illustration of the AOH gain used in online operation . . . . .	63
3.7 Cluster charge distribution and correlation of the MPV with $\eta$ . . . . .	65
3.8 Distribution of the APV MPV . . . . .	68
3.9 Distribution of the normalized cluster charge . . . . .	70
3.10 Distribution of the tick-mark height . . . . .	72
3.11 Muon $\Delta E/\Delta x$ as a function of track momentum . . . . .	74
4.1 Mean energy loss rate . . . . .	79
4.2 Distribution of the MP $dE/dx$ estimators (tick-mark vs particle) . . . . .	82
4.3 Distribution of the MP $dE/dx$ estimators for data . . . . .	83
4.4 Distribution of the MP $dE/dx$ estimators for mc . . . . .	84
4.5 Determining the Bethe-Bloch parametrization constants . . . . .	86
4.6 Mass reconstruction with $dE/dx$ . . . . .	86
4.7 Distribution of the MP $dE/dx$ vs momentum . . . . .	87
4.8 Templates used by the $dE/dx$ discriminators . . . . .	90
4.9 Distribution of the $dE/dx$ discriminator . . . . .	90
4.10 Distribution of the $dE/dx$ discriminator vs momentum . . . . .	91
4.11 Signal and background efficiency for a $dE/dx$ based selection . . . . .	92
4.12 Invariant mass distribution of the reconstructed $\Lambda$ . . . . .	93

4.13 MP $dE/dx$ estimator versus momentum for $\Lambda$ decay . . . . .	94
4.14 $dE/dx$ discriminator versus momentum for $\Lambda$ decay . . . . .	94
4.15 Illustration of a SST cluster with a double maximum . . . . .	95
4.16 Illustration of a SST cluster affected by a hard $\delta$ -ray . . . . .	95
4.17 Distribution of SST cluster size and charge for MIP . . . . .	96
4.18 Distribution of SST cluster size and charge for HSCP . . . . .	97
4.19 Distribution of SST cluster size and charge for deuteron . . . . .	98
4.20 Distribution of the $I_{as}^d$ discriminator with and without cluster cleaning. .	98
5.1 Trigger efficiencies as a function of the HSCP velocity . . . . .	106
5.2 Trigger efficiencies . . . . .	107
5.3 Distribution of $\# \Delta E/\Delta x$ SST measurements and error on $p_T$ . . . .	109
5.4 Distribution of the $dx$ and $dz$ . . . . .	110
5.5 Distribution of $p_T$ and $I_{as}$ . . . . .	113
5.6 Stability of $I_{as}/p_T$ with time . . . . .	114
5.7 Impact of the cluster cleaning on the $I_{as}$ distribution . . . . .	115
5.8 Expected number of signals versus predicted number of backgrounds .	116
5.9 Distribution of $I_{as}$ for track of different #Hits and $\eta$ region . . . . .	117
5.10 Number of candidates observed for different selection used . . . . .	119
5.11 Distribution of $p$ vs $I_h$ and mass for pre-selected HSCP tracks . . . .	121
5.12 $I_{as}$ and $I_h$ distributions for two momentum ranges . . . . .	122
5.13 Ratio between observed and predicted candidates for different selection	124
5.14 Number of candidates predicted for different selection used . . . . .	126
5.15 Observed and Predicted mass spectra for the loose selection . . . . .	129
5.16 Distribution of $I_h$ vs $p$ for candidates passing the loose selection . .	129
5.17 Transverse and longitudinal FROG views of an HSCP candidate . . . .	131
5.18 Transverse and longitudinal FROG views of an HSCP candidate . . . .	132
5.19 95% C.L. cross-section upper limits for the tracker+muon selection . .	135

---

5.20 95% C.L. cross-section upper limits for the tracker-only selection . . . . .	137
5.21 95% C.L. cross-section upper limits for the tracker-only selection . . . . .	139
A.1 Schematic view of the FROG architecture (part 1) . . . . .	148
A.2 Schematic view of the FROG architecture (part 2) . . . . .	149
A.3 A schematic view of the tree structure of a FFF. . . . .	150
A.4 Example of a FROG file data structure . . . . .	151
A.5 Example of the chunk structure if the file contains 100 Int32. . . . .	151
A.6 Three different FROG Display views . . . . .	153
A.7 Example view of the FROG Tree Menu . . . . .	156
A.8 Stereoscopic screenshots of CMS Geometry and Events . . . . .	158
A.9 Three different shader projections of a CMS event . . . . .	161
A.10 a 3D view of the GAS TOF geometry . . . . .	162
A.11 2D views of four different GAS TOF events . . . . .	163
A.12 Layout of the generic DELPHES geometry . . . . .	164
A.13 A 3D view of a DELPHES geometry and event . . . . .	165
A.14 A transverse view of an ILD Design and a 3D view of an event . . . . .	166
A.15 Two FROG view of TOTEM events . . . . .	167
A.16 FROG views of a QCD Di-jets event . . . . .	168
A.17 FROG views of a heavy-ion event . . . . .	169
A.18 FROG view of one of the first LHC 7 TeV event in CMS . . . . .	169
A.19 FROG view of the best Top candidate observed in CMS . . . . .	170





Université catholique de Louvain  
Secteur des sciences et technologies  
Institut de recherche en mathématique et physique  
Center for Cosmology, Particle Physics and Phenomenology

Chemin du Cyclotron 2, 1348 Louvain-la-Neuve, Belgium  
Tél. : +32 (0) 10 47 32 73 - fax : +32 (0) 10 45 21 83  
<http://cp3.phys.ucl.ac.be/>

E-mail : Loïc.Quertenmont@cern.ch – loicus@gmail.com  
<http://cern.ch/quertenmont>

Heavy Stable (or long-lived) Charged Particles (HSCP) are predicted by various extensions to the Standard Model of the fundamental interactions among elementary particles. If this prediction reveals to be true, such particles should be produced at the Large Hadron Collider (LHC) and observable with the Compact Muon Solenoid (CMS) detector.

The LHC produced the first pp collisions at  $\sqrt{s} = 7$  TeV at the beginning of April 2010. These first collisions were used to calibrate the detector but also to search for new physics.

If HSCPs are produced in LHC collisions they will have an anomalously high ionization energy loss ( $dE/dx$ ) that can be measured using the CMS Silicon Strip Tracker (SST). These highly penetrating particles are expected to reach the CMS Muon System. The typical HSCP signature is therefore a high momentum track with an anomalously high  $dE/dx$  that reaches the muon system. However, a recent study on the modelling of the interaction of the HSCP with matter claims that certain species of HSCPs are undetectable in the muon system. A complementary search, which does not require the HSCP track to reach the muon system, was therefore developed.

The results of these two model-independent searches for HSCPs produced in pp collisions at  $\sqrt{s} = 7$  TeV are presented in this thesis. The tools needed to exploit the unique HSCP signature are also discussed, including the algorithms for the SST calibration, for identification and mass reconstruction of the particles based on their  $dE/dx$ . FROG, an innovative application for data visualization in high energy physics is also presented.

*Loïc Quertenmont was born in Belgium in 1985. He studied physics at the University of Louvain and got introduced to high energy physics via his master thesis on jet reconstruction algorithms. He started a Ph.D. on the search for HSCP in October 2007 and he is about to start a postdoctoral research on the same topic at the Florida State University.*

208 | 2010

Loïc Quertenmont

Search for Heavy Stable Charged Particles with the CMS detector at the LHC

# Search for Heavy Stable Charged Particles with the CMS detector at the LHC

## From Detector Commissioning to Data Analysis

Loïc QUERTENMONT

OCTOBRE 2010

Thèse présentée en vue de l'obtention  
du grade de docteur en sciences

Faculté des sciences  
École doctorale en sciences

Université catholique de Louvain



UCL